

Recent Advances in Understanding Particle Acceleration Processes in Solar Flares

V. V. Zharkova¹, K. Arzner², A. O. Benz²,
P. Browning³, C. Dauphin⁴, A. G. Emslie^{5,6},
L. Fletcher⁷, E. P. Kontar⁷, G. Mann⁸, M. Onofri⁹,
V. Petrosian¹⁰, R. Turkmani¹¹, N. Vilmer⁴, and
L. Vlahos⁹

the date of receipt and acceptance should be inserted later

Abstract We review basic theoretical concepts in particle acceleration, with particular emphasis on processes likely to occur in regions of magnetic reconnection. Several new developments are discussed, including detailed studies of reconnection in three-dimensional magnetic field configurations (e.g., current sheets, collapsing traps, separatrix regions) and stochastic acceleration in a turbulent environment. Fluid, test-particle, and particle-in-cell approaches are used and results compared. While these studies show considerable promise in accounting for the various observational manifestations of solar flares, they are limited by a number of factors, mostly relating to available computational power. Not the least of these issues is the need to explicitly incorporate the electrodynamic feedback of the accelerated particles themselves on the environment in which they are accelerated. A brief prognosis for future advancement is offered.

Keywords Sun: flares; Sun: X-rays; Sun: acceleration; Sun: energetic particles

¹Department of Mathematics, University of Bradford, U.K. E-mail: v.v.zharkova@brad.ac.uk

²ETH Zurich, Switzerland

³Physics Department, University of Manchester, U.K.

⁴Observatoire de Paris, LESIA, France

⁵Department of Physics, Oklahoma State University, Stillwater, OK 74078, U.S.A.

⁶Department of Physics and Astronomy, Western Kentucky University, Bowling Green, KY 42101, U.S.A.

⁷Department of Physics and Astronomy, University of Glasgow, Glasgow, G12 8QQ, U.K.

⁸Astrophysikalischen Institut, Potsdam, Germany

⁹Dept. of Physics, University of Thessaloniki, Thessaloniki 54124, Greece

¹⁰Center for Astrophysics, Stanford University, U.S.A.

¹¹Imperial College, London, U.K.

Contents

1	Introduction	3
2	Review of Pertinent Observations	4
2.1	Hard X-ray lightcurves and spectra	4
2.1.1	Lightcurves	4
2.1.2	Photon and electron energy spectra	5
2.1.3	Electron numbers	7
2.2	Lightcurves and energy spectra of γ -rays	8
2.2.1	Gamma-ray lightcurves	8
2.2.2	Energy spectra and abundances of ions in flares	9
2.2.3	Ion numbers	9
2.3	Geometry of hard X-ray and gamma-ray sources	10
2.3.1	Differences in footpoint spectral indices	10
2.3.2	Hard X-ray and gamma-ray sources	11
2.4	Hard X-ray and radio emission	12
2.5	Magnetic field changes associated with the flare	13
3	Models of Particle Acceleration	13
3.1	Basic physics	13
3.2	Magnetic reconnection models associated with flares	14
3.2.1	Basic 2-D MHD theory of magnetic reconnection	15
3.2.2	Effect of the Hall current on reconnection rates in 2-D models	16
3.2.3	Further improvement of reconnection models	17
3.3	Particle acceleration in a reconnecting current sheet	18
3.4	Particle acceleration by shocks and turbulence	21
3.4.1	Shock acceleration	21
3.4.2	Stochastic Acceleration	22
4	Recent Theoretical Developments	24
4.1	Stochastic acceleration	25
4.1.1	Improvements to the MHD stochastic acceleration model	25
4.1.2	Stochastic acceleration with particle feedback	25
4.2	Particle acceleration by large-scale Alfvén waves	26
4.3	Electron acceleration in collapsing current sheets	28
4.3.1	Acceleration in collapsing magnetic traps	29
4.3.2	Acceleration by a termination shock	30
4.4	Particle acceleration in a single 3-D RCS with complicated magnetic topology	32
4.4.1	Basic equations	32
4.4.2	Particle motion inside a 3-D RCS	33
4.5	Particle acceleration in 3-D MHD models with fan and spine reconnection	36
4.6	Particle acceleration in multiple current sheets formed by MHD turbulence	41
4.6.1	Acceleration in Cellular Automata Models	41
4.6.2	Acceleration in three-dimensional MHD turbulence	44
4.6.3	Acceleration in stochastic current sheets	45
4.6.4	Limitations of MHD turbulence models	46
4.7	Limitations of the test particle approach	46
4.7.1	The polarization electric field	47
4.7.2	Turbulent electric fields	47
4.8	Particle-in-cell simulation of acceleration in a 3-D RCS	48
4.8.1	Description of the PIC approach	48
4.8.2	PIC simulation results	49
4.8.3	Polarization electric field induced by accelerated particles	50
4.8.4	Particle trajectories	51
4.8.5	Energy spectra	52
4.8.6	Turbulent electric field	52
4.9	Particle acceleration in collapsing magnetic islands	54
4.9.1	Tearing-mode instability in current sheets	54
4.9.2	Studying particle acceleration in magnetic islands using a PIC approach	54
4.10	Limitations of the PIC approach	58
5	How well do Recent Theories Account for Observed Flare Characteristics?	59
5.1	Interrelation between acceleration and transport	59

5.2	Testing acceleration models against observational constraints	59
5.2.1	Stochastic acceleration	59
5.2.2	Collapsing current sheets	60
5.2.3	Acceleration in 3D reconnecting current sheets	60
5.2.4	Complex reconnection models	61
6	Summary	62

1 Introduction

It is by now well established that the primary source of the energy released in a solar flare is in stressed, current-carrying (“non-potential”) magnetic fields. This magnetic energy is released through a *magnetic reconnection* process, in which magnetic field lines of opposite polarity change their topological connectivity and the field relaxes to a state of lower energy, thereby releasing energy in the form of accelerated particles, plasma heating and mass motion.

Magnetic reconnection can occur in several geometries. For example, closed magnetic loops embedded into the solar photosphere can collide in the upper solar atmosphere, resulting in a localized region of relatively high magnetic shear, as in the classical Sweet-Parker model (see, e.g., Sweet 1969). Alternatively, open magnetic field lines can collapse onto a closed helmet-like magnetic configuration. This leads to a region of high magnetic shear near the top of the closed structure – as evidenced by looptop sources of hard X-rays first observed by *Yohkoh* (Masuda et al. 1994) – and in the energization of successive field lines at greater and greater heights, which produces both coronal hard X-ray sources (Krucker et al. 2008a) and a concomitant increase in the separation of the associated hard X-ray and $H\alpha$ footpoints (Kopp & Pneuman 1976). Magnetic reconnection can also be accompanied by dramatic large-scale changes in the magnetic field configuration, such as in the “breakout” model (Antiochos et al. 1999), in which a filament, previously restrained by the magnetic tension of a set of magnetic field lines exterior to it, is released into interplanetary space as a result of reconnection of the constraining field lines. Reconnection can also result in the formation of magnetohydrodynamic (MHD) shocks, which may be responsible for significant particle acceleration exterior to the region of magnetic reconnection itself.

Whatever the geometry, the fundamental process of magnetic reconnection somehow transfers a significant fraction (e.g., Miller et al. 1997) of the stored magnetic energy into accelerated charged particles, both electrons and ions. Some of the high-energy particles may be trapped in the corona by plasma turbulence (e.g., Petrosian & Liu 2004) and/or by magnetic mirroring (e.g., Melrose & White 1979; Leach 1984; Somov & Kosugi 1997), to produce hard X-ray (HXR) looptop sources (e.g., Masuda et al. 1994; Petrosian et al. 2002; Sui & Holman 2003; Jiang et al. 2006; Battaglia & Benz 2006; Liu 2006). Some particles may escape the acceleration region into interplanetary space and can contribute to solar energetic particle (SEP) events detected at 1 AU (e.g., Krucker et al. 2007a).

Understanding the conversion of magnetic energy into accelerated particles is one of the main goals of solar flare research. It also has attendant implications for our understanding of particle acceleration in other astrophysical sites and was indeed a key driver for the design of *Reuven Ramaty High-Energy Solar Spectroscopic Imager (RHESSI)*, which measures the diagnostic high-energy hard X-ray and gamma-ray radiation produced by the accelerated particles with unprecedented temporal, spectral and spatial resolution.

At a fundamental level, of course, charged particles are accelerated by an electric field. Differences in the large-scale structure and temporal evolution of the accelerating electric

field allows us to discuss particle acceleration in terms of several basic scenarios (see Section 3). These include large-scale sub-Dreicer acceleration (see, for example Benka & Holman 1994); super-Dreicer acceleration in a relatively localized 2-D current sheet (e.g., Litvinenko & Somov 1993a); and stochastic acceleration by MHD turbulence generated in fast plasma reconnection outflows (e.g., Miller et al. 1996; Pryadko & Petrosian 1997).

In Section 4, we report on recent work aimed at extending these basic mechanisms to more complex models. These include (1) first-order Fermi acceleration, either in a collapsing magnetic trap (Somov & Kosugi 1997) or in a fast termination shock (Tsuneta & Naito 1998; Aurass et al. 2007), or by a super-Dreicer electric field in a simple 3-D magnetic topology (Zharkova & Gordovskyy 2005b; Zharkova & Agapitov 2009); and (2) acceleration in more elaborate three-dimensional magnetic topologies derived from MHD simulations (Dalla & Browning 2006, 2008). We also discuss some recent suggestions of acceleration by large-scale Alfvén waves (Fletcher & Hudson 2008) and acceleration involving multiple reconnection regions or in a turbulent environment (Vlahos et al. 2004; Turkmani et al. 2005; Dauphin & Vilmer 2007).

In the latter portion of Section 4 we also consider both “local” and “global” aspects of the acceleration process. At the local level, accurate simulations of particle trajectories are needed to correctly infer the general properties of the acceleration. At the “global” level, we recognize that, in view of the large number of accelerated particles involved, the traditional “test-particle” approach, in which the electromagnetic environment in the acceleration region is *prescribed*, is not applicable (Section 4.7) – a self-consistent approach requires that we incorporate the electric and magnetic fields associated with the accelerated particles themselves in current sheets with and without tearing instabilities (Sections 4.8 and 4.9).

In Sections 5 and 6 we relate the results of the recent modeling efforts to flare observations, particularly from *RHESSI*, and we offer a brief prognosis for future models of the particle acceleration process.

2 Review of Pertinent Observations

2.1 Hard X-ray lightcurves and spectra

2.1.1 Lightcurves

Spatially-integrated hard X-ray light curves obtained by *RHESSI* confirm many of the temporal features established by previous observations: sharp increases (bursts) of hard X-ray intensity over a relatively short (~ 0.5 -5 s) timescale accompanied by a more slowly-varying component with a timescale up to a few tens of minutes (Holman et al. 2011). This suggests that electron acceleration is characterized by two fundamentally distinct timescales: a very short timescale associated with the actual *acceleration* of ambient electrons to high, bremsstrahlung-emitting energies and a much longer timescale associated with the *duration* of the acceleration process, a process that, as evidenced by steady hard X-ray emission for a substantial fraction of an hour or even longer, can continue to accelerate particles over such a sustained period.

At lower photon energies ε , where thermal bremsstrahlung dominates the total emission, the emission at higher photon energies is weighted more heavily by plasma at high temperatures T .

As a result, the decrease in conductive cooling time with temperature – $\tau \approx T^{-5/2}$ for collisionally-dominated conductive processes (see Spitzer 1962) – results in the emission

at higher energies peaking sooner (Aschwanden 2007), and hence the light curve peaking progressively earlier with increase in photon energy. At higher energies, where *non-thermal* bremsstrahlung dominates, the relative timing of the emission at different energies depends on a balance between the reduced “time-of-flight” for higher energy electrons before they impact upon the thick target of the lower atmosphere (which tends to *advance* high energy emissions relative to low energy ones – Aschwanden & Schwartz 1996; Brown et al. 1998) and on the decrease in collision frequency with energy (which tends to *delay* high energy emissions relative to low energy ones – Aschwanden et al. 1997).

2.1.2 Photon and electron energy spectra

Hard X-ray emission during flares typically exhibits a very steep spectrum at lower energies $\epsilon \approx 10$ keV, indicative of a thermal process. It must be noted, however, that the frequent assumption (e.g., Holman et al. 2003) of an *isothermal* plasma is neither expected on the basis of simple physics nor required by the observations (e.g., Brown 1974). Indeed, Aschwanden (2007) has shown that the assumption of an isothermal source is *inconsistent* with the observations of temporal variations of the hard X-ray spectrum in certain flares observed by *RHESSI*. Indeed, in most cases analysis of the variation of residuals (observed hard X-ray flux vs. flux calculated using an isothermal spectrum) with photon energy shows that that an isothermal model *does* provide an excellent fit to the observed spectrum; generally a broad-band hard X-ray spectrometer shows the (unique) hottest component of a multithermal source. Nevertheless *RHESSI*'s superior resolution and good photometric calibration have made it possible to derive a two-temperature source characterization from a single bremsstrahlung spectrum (e.g., Caspi & Lin 2010) in some cases.

In most powerful flares the photon spectra reveal double power laws below 300 keV, with the spectral index below ~ 30 -60 keV being smaller (flatter) than that above ~ 30 -60 keV by 2-4 units (Grigis & Benz 2006; Krucker et al. 2008a). For the most energetic flares, there can be discernible emission up to a few hundred MeV (for reviews, see Chupp & Ryan 2009; Vilmer et al. 2011). At photon energies ~ 500 -1000 keV, the spectrum tends to flatten again, a flattening that has been, at least partially, attributed to the increasing contribution of electron-electron bremsstrahlung (Kontar et al. 2007). However, the contribution of electron-electron bremsstrahlung to this flattening does not exceed ~ 0.4 , while the observed spectral hardening, as observed in a few events with *GRANAT/PHEBUS*, can be as high as 1.5-2 units at energies from 600 keV up to several tens of MeV (see, e.g., Trottet et al. 1998; Vilmer et al. 1999).

RHESSI observations reveal a relationship between spectral hardness and time. Values of the “local” spectral index $\gamma(\epsilon) = -d \log I(\epsilon) / d \log \epsilon$ are generally lowest around the peak of the event – a so-called “soft-hard-soft” evolution originally noted by Parks & Winckler (1969). *RHESSI*'s superior spectral resolution shows that nearly every discernible intensity peak (which can number up to a dozen or more in a single flare) has a soft-hard-soft structure (Grigis & Benz 2004). Also the decrease in spectral index before, and increase in spectral index after, this time does not occur at the same rate for all photon energies ϵ (Kontar & MacKinnon 2005); see Figure 2.1. Rather, a flare typically starts with a spectral index γ that is strongly dependent on energy, with the minimum value of γ showing a tendency to grow with time.

Non-thermal emission in the corona is identified in the impulsive phase by its softer spectrum (Mariska & McTiernan 1999; Petrosian et al. 2002), consistent with the small column depth of the coronal part of the source. The absence of a significant amount of (energy-dependent) collisional losses in this relatively thin target should result in a spectrum two

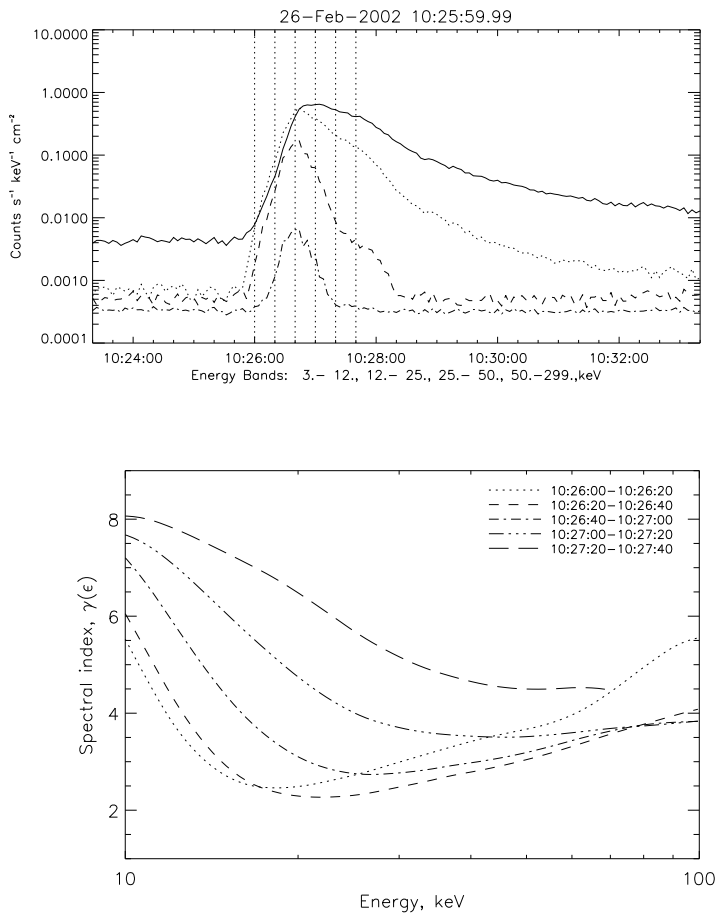


Fig. 2.1 *Upper Panel:* Temporal variation (4-second cadence) of the count rates in seven front *RHESSI* segments for SOL2002-02-26T10:27 (C9.6) (10:27 UT). The vertical lines show five 20-second accumulation intervals for spectral analysis. *Lower Panel:* Temporal variation of the energy-dependent photon spectral index $\gamma(\epsilon) = -d \log I(\epsilon) / d \log \epsilon$. Each line corresponds to one of the time intervals in the upper plot. From Kontar & MacKinnon (2005).

powers steeper than the target-averaged spectrum (Brown 1971; Hudson 1972; Datlowe & Lin 1973).

It should be noted that even if the accelerated electrons have a pure power-law energy spectrum $F_0(E_0) \approx E_0^{-\delta}$, for which a characteristic energy does not exist, characteristic energies associated with either electron transport and/or radiation physics may produce deviations from the power-law behavior in the observed spatially-integrated photon spectrum. Further, as elaborated upon by Kontar et al. (2011), anisotropy in the mean electron distribution, combined with the intrinsic directivity of the bremsstrahlung emission process, produces an anisotropic distribution of primary photons. Compton backscattering of photons from the photosphere (“X-ray albedo;” Langer & Petrosian 1977; Bai & Ramaty 1978) not only influences the observed photon spectrum, but also has a diagnostic potential for determining the electron angular distribution (Kontar & Brown 2006).

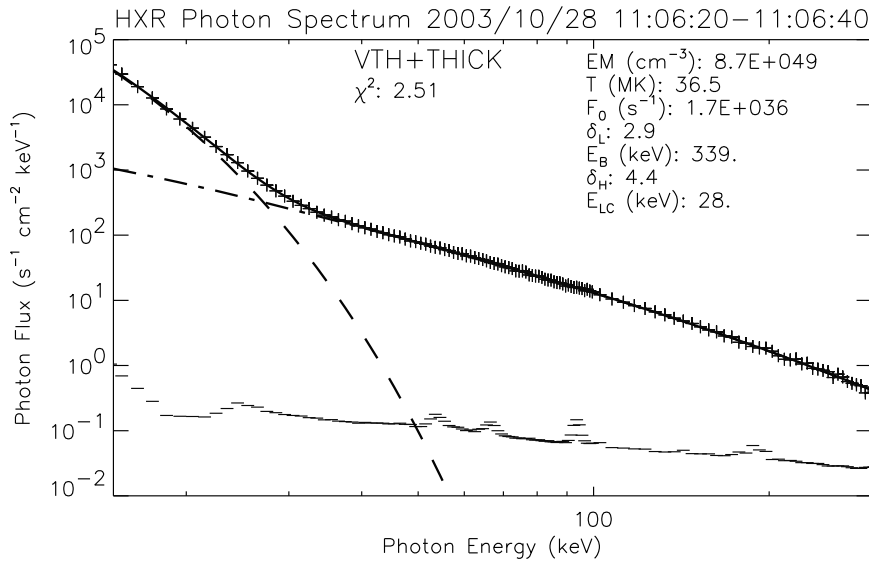


Fig. 2.2 *RHESSI* hard X-ray photon spectrum for SOL2003-10-28T11:10 (X17.2) (11:06:20–11:06:40 UT). The photon flux (plus signs) is fit with a thermal bremsstrahlung contribution from an isothermal plasma (dashed curve) plus a double power-law non-thermal electron flux component with a low-energy cutoff (dash-dotted curve). The best-fit parameters are shown in the plot.

2.1.3 Electron numbers

Analysis of *RHESSI* data (Brown et al. 2007; Dennis et al. 2007) has confirmed the important point that a significant fraction of the energy released in flares is deposited into accelerated particles. In addition, recent calorimetric analysis of the evolution of a radio spectrum from a dense flare (Bastian et al. 2007) reveals that a substantial fraction of the energy in the energetic electrons can be deposited into the coronal loop, rather than into the chromosphere; it is estimated that the energy deposited in the corona can approach about 30% of the estimated magnetic energy released in the whole flare.

As has been pointed out by several authors (e.g., Brown 1971; Tandberg-Hanssen & Emslie 1988), the total injected electron flux depends critically on the value of the low-energy cutoff E_c . A brief discussion of this issue is in order. Historically, a low-energy cutoff E_c was assumed simply in order to keep the injected power $\int_{E_c}^{\infty} E_0 F_0(E_0) dE_0$ finite (e.g., Brown 1971; Holman et al. 2003). To determine whether or not such a cut-off is actually *required* by observations, it is best to adopt a non-parametric approach to interpreting the photon spectrum $I(\varepsilon)$ – i.e., to infer from $I(\varepsilon)$ what range of mean electron source functions $\overline{F}(E)$ (Brown et al. 2003) allow a statistically acceptable fit to $I(\varepsilon)$. Kašparová et al. (2005), in their analysis of SOL2002-08-20T08:25 (M3.4), have shown that a low-energy cutoff, or even a gap, in the mean source electron spectrum exists if the observed spectrum is considered as primary bremsstrahlung only; however, such cutoffs and/or gaps disappear if an albedo correction (for an isotropic primary source) is applied to the observed photon spectrum (see, e.g., Kontar et al. 2011). Further, Emslie (2003) has shown that, when allowance is made for warm-target effects in the electron energy-loss rate, the injected electron energy

$\int_0^\infty E_0 F_0(E_0) dE_0$ corresponding to a pure power-law photon spectrum can be finite even if no low-energy cutoff exists.

Figure 2.2 shows the photon spectrum for the time interval indicated during SOL2003-10-28T11:10 (X17.2). Assuming that the non-thermal hard X-ray emission is thick-target bremsstrahlung (Brown 1971), one can use a forward-fitting method, including both thermal and nonthermal fit components, (e.g., Holman et al. 2003) to derive the injected non-thermal electron acceleration rate, differential in energy (electrons $s^{-1} \text{ keV}^{-1}$). This method (see Kontar et al. 2011) also determines an observational upper limit to E_c (as the intersection of the thermal and nonthermal fit components), and hence a lower limit on the associated electron number and energy fluxes. Integration over energy provides the total electron acceleration rate. For this event, one obtains a total non-thermal electron production rate $F_e = 1.7 \times 10^{36} s^{-1}$ above $E_c = 28 \text{ keV}$, corresponding to an injected power $P_e = 1.5 \times 10^{29} \text{ erg s}^{-1}$ above the same energy. For a nominal footpoint area $S \lesssim 10^{18} \text{ cm}^2$, such a particle rate corresponds to an electron flux $F_e \gtrsim 10^{18} \text{ cm}^{-2} s^{-1}$ and hence, since the average electron velocity $v \approx (c/3) \approx 10^{10} \text{ cm s}^{-1}$, to a beam density $n_b \gtrsim 10^8 \text{ cm}^{-3}$. This is a substantial fraction of the ambient density $n \approx 10^{10} \text{ cm}^{-3}$.

The total electric *current* corresponding to such a particle acceleration rate, *if the acceleration is unidirectional*, is $I \approx 3 \times 10^{17} \text{ A}$, and the associated current density $j = I/S \approx 0.3 \text{ A cm}^{-2}$. Such high current densities, especially since they are introduced over a timescale of seconds, produce unacceptably large inductive electric and magnetic fields, unless (1) the acceleration is near-isotropic, as in stochastic acceleration models (Section 3.4), (2) the source has very fine structure (Holman 1985), or (3) the beam current is effectively neutralized by a co-spatial return current formed by both the ambient and returning beam electrons (see Knight & Sturrock 1977; Emslie 1980; Brown & Bingham 1984; Larosa & Emslie 1989; van den Oord 1990; Zharkova & Gordovskyy 2006).

Finally, the total number of electrons in the acceleration region $\mathcal{N} = nV \approx 10^{37}$, a number which corresponds to only a few seconds of acceleration at the rates quoted above. Hence the issue of replenishment of the acceleration region (Emslie & Hénoux 1995) has to be accounted for by any acceleration and/or transport mechanism.

2.2 Lightcurves and energy spectra of γ -rays

2.2.1 Gamma-ray lightcurves

Due to the limited sensitivity of current gamma-ray detectors, information regarding the time scales for ion acceleration is less stringent than that for energetic electrons (Section 2.1).

The prompt gamma-ray line emission is known to peak roughly simultaneously, within $\pm 1 \text{ s}$, of the hard X-ray continuum emission, based on a few events (e.g., Kane et al. 1986).

This near-simultaneity of hard X-ray and gamma-ray emissions indicates that both ion acceleration to a few MeV, and interaction of the accelerated ions with the ambient atmosphere to produce nuclear lines (Vilmer et al. 2011), can occur within a timescale $\sim 1 \text{ s}$. However, in a few flares there *are* time delays between the appearance of hard X-rays and gamma-ray lines (see section 2.2.6 in Vilmer et al. 2011); this is often interpreted in terms of differential transport of electrons and ions between the acceleration and emission sites.

RHESSI observations (see, e.g., Figure 3.1 in Vilmer et al. 2011) have provided unprecedented information on the temporal evolution of “pure” gamma-ray lines (i.e., lines that occur in spectral regions that are relatively uncontaminated by electron bremsstrahlung). Such observations indicate the continuous production of very energetic ions ($>$ a few hundreds

of MeV) for hours after the impulsive phase of the flare, and so pose a formidable constraint on the ion acceleration mechanism (Vilmer et al. 2011).

RHESSI observations have also provided important information on the temporal evolution of prompt gamma-ray lines (Lin et al. 2003). Comparison with the temporal evolution of the X-ray flux at 150 keV shows that the temporal evolution of hard X-rays and gamma-rays are roughly similar, indicating a common origin of accelerated electrons and ions. However, for SOL2002-07-23T00:35 (X4.8), there is a small delay of around 10 s between the maxima of the X-ray and gamma-ray fluxes. This has been interpreted in terms of transport of energetic electrons and ions by Dauphin & Vilmer (2007), and is discussed in Vilmer et al. (2011).

2.2.2 Energy spectra and abundances of ions in flares

As reviewed by Vilmer et al. (2011), interactions of energetic ions in the energy range from ~ 1 MeV nucleon⁻¹ to 100 MeV nucleon⁻¹ produce an extensive spectrum of gamma-ray line emission. Narrow gamma-ray lines result from the bombardment of the ambient nuclei by accelerated protons and α -particles, while broad lines occur from the inverse reactions, in which accelerated heavy nuclei collide with ambient hydrogen or helium nuclei. De-excitation gamma-ray line spectra provide information on flare ions of energies above ~ 2 MeV nucleon⁻¹. The shape of the ion distribution below this energy is unknown, but is comparably important for the evaluation of the total ion energy as is the low-energy cutoff to the evaluation of the total electron energy content (Section 2.1) (see Emslie et al. 1997).

Quantitative gamma-ray line observations have now been obtained for more than twenty events. The accelerated ion spectra are found to extend as unbroken power laws down to at least 2 MeV nucleon⁻¹, if a reasonable ambient Ne/O abundance ratio is used (for details, see Vilmer et al. 2011). For the 19 flares observed by the *Solar Maximum Mission (SMM)* prior to the launch of *RHESSI*, the average spectral index was around 4.3; however, the events observed with *RHESSI* tend to have much harder slopes (Lin et al. 2003; Share & Murphy 2006).

Even though most of the energy contained in ions resides in protons and α -particles, the abundances of heavier accelerated ions provide crucial constraints for acceleration processes. Information on the abundances of such flare-accelerated ions was deduced for the *SMM/GRS* (Gamma-Ray Spectrometer) flares as well as for a few flares observed by *RHESSI*. A noticeable enhancement has been observed in the numbers of α -particles, as well as of accelerated ³He isotopes, compared to the standard coronal abundances. Furthermore, accelerated heavy ions, such as Ne, Mg and Fe, are also generally found to be over-abundant with respect to normal coronal compositions, as pointed out by Vilmer et al. (2011). This poses another constraint on models for ion acceleration.

2.2.3 Ion numbers

Since the first detection of solar flare gamma-ray lines in 1972 (Chupp et al. 1973), information on the energy content in ions has been obtained for more than 20 events. The analysis carried out using 19 events observed by *SMM/GRS* and a few events observed with *RHESSI* shows that the energy contained in >1 MeV ions ranges from 10^{29} to 10^{32} erg, comparable to the energy contained in sub-relativistic electrons. However, there are still large uncertainties in the determination of these quantities and a large dispersion of the ratio of electron (~ 20 keV) to ion (~ 1 MeV nucleon⁻¹) energy contents from one flare to another (for details, see Vilmer et al. 2011).

The issue of relative importance of electron and ion acceleration can also be addressed by comparing the production ratios of ions to quasi-relativistic electrons ($E \gtrsim 300$ keV). Such an analysis has been performed using both *SMM/GRS* (Forrest 1983; Chupp 1984; Chupp & Benz 1994) and *RHESSI* (Shih et al. 2009b) observations. Good correlations have been found between the total energy content in protons above 30 MeV and the total energy content in electrons above 300 keV, suggesting that high-energy electrons and ions are linked through a common acceleration processes. It should be noted, however, that in the statistical study by Shih et al. (2009a), a correlation between the number of protons with energies above 30 MeV, the electron number above 50 keV, and the soft X-ray *Geostationary Operational Environmental Satellite (GOES)* class exists, but only above a certain threshold in the level of ion production.

2.3 Geometry of hard X-ray and gamma-ray sources

The imaging capabilities of *RHESSI*, combined with its high spectral resolution, have allowed us to resolve in detail coronal sources (e.g., Krucker et al. 2008a) and footpoints occurring in the same flare (see Figure 2.3) and hence to study the acceleration processes that give rise to such sources.

The coronal source often appears before the main flare hard X-ray increase and the appearance of footpoints. In the impulsive phase, the coronal hard X-ray emission is, generally, well correlated in both time and spectrum with the footpoints (Emslie et al. 2003; Battaglia & Benz 2006). These observations suggest strong coupling between the corona and chromosphere during flares, a coupling that is presumably related to transport of accelerated particles from one region to the other.

2.3.1 Differences in footpoint spectral indices

An interesting *RHESSI* observation is the approximate equality of the spectral indices in different footpoints of the same loop. Emslie et al. (2003) reported differences $\Delta\gamma \approx 0.3 - 0.4$ between the spectral indices of the two dominant footpoints in SOL2002-07-23T00:35 (X4.8). In a few smaller events analyzed by Battaglia & Benz (2006), $\Delta\gamma$ is even smaller and indeed is significant only in one out of five cases. However, other observations of X-class flares reveal a much stronger difference (up to 5) between the spectral indices of footpoints of the same loop (Takakura et al. 1995; Battaglia & Benz 2006; Krucker et al. 2007b).

More surprising than the occasional difference between the spectral indices of footpoints are the differences (or lack thereof) between the spectra of the coronal source and the footpoints. The spectral index difference $\Delta\gamma = 2.0$ predicted (Brown 1971) between thin- and (collision-dominated) thick-target sources is *not* observed in most cases (Holman et al. 2011). Differences $\Delta\gamma$ smaller than 2 could in principle be interpreted by invoking a coronal target that is intermediate between thin- and thick-target conditions; such spectral differences could also be partially accounted for by the transport effects of precipitating electrons, e.g., by the effect of a self-induced electric field (Zharkova & Gordovskyy 2006). However, $\Delta\gamma$ ranges from 0.59 to 3.68 (Grigis & Benz 2006; Krucker et al. 2007b), which includes values beyond the capability of simple models to explain. For example, Figure 2.4 (after Battaglia & Benz 2006) displays the photon energy spectra of two footpoints and a coronal source, obtained for the same time interval during the flare SOL2005-07-13T14:49 (M5.0). The footpoint non-thermal power-law indices γ are near-identical (2.7 ± 0.1), while

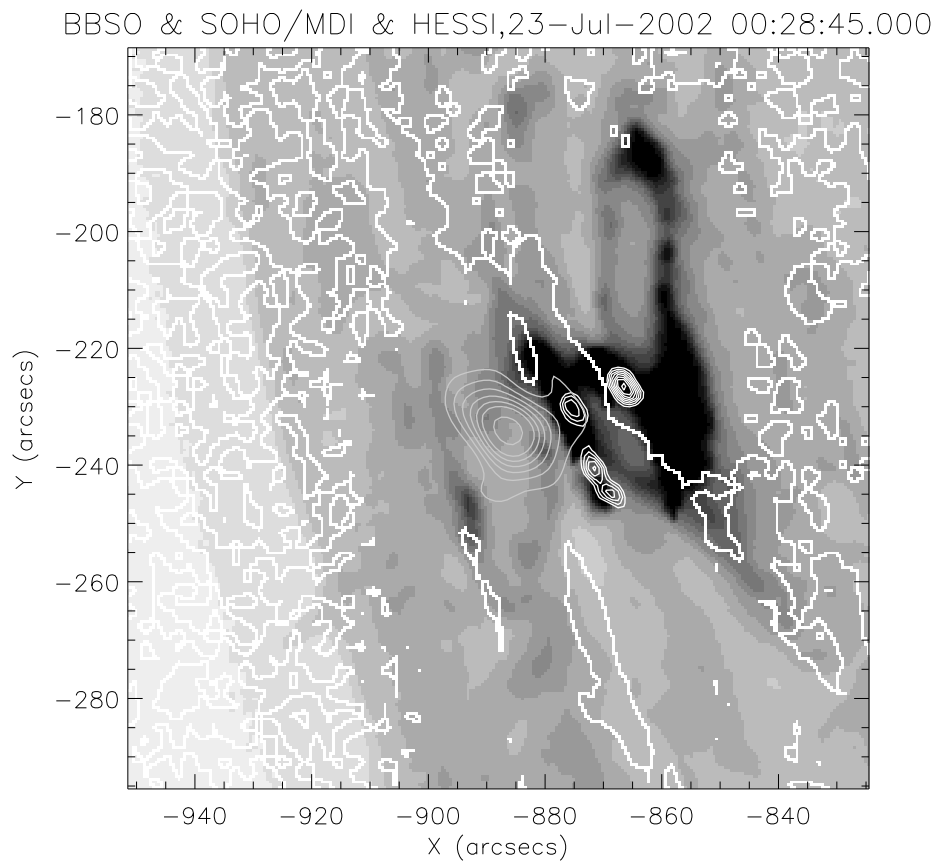


Fig. 2.3 *RHESSI* hard X-ray images of SOL2002-07-23T00:35 (X4.8) (white thin contours) taken at 00:28 UT, overlaid on Michelson Doppler Imager (MDI) neutral-line magnetograms (white thick contours) and (negative) $H\alpha$ taken at 00:28:45 UT. One extended (coronal) and three compact (footpoint) hard X-ray sources are evident. From Zharkova et al. (2005).

the spectral index of the non-thermal emission for the coronal source is substantially steeper ($\gamma = 5.6 \pm 0.1$).

2.3.2 Hard X-ray and gamma-ray sources

Gamma-ray images were first obtained by *RHESSI* for the flare SOL2002-07-23T00:35 (X4.8) (Hurford et al. 2003). They revealed the striking result that the hard X-ray sources are separated by a considerable distance ($\gtrsim 20''$) from the 2.223 MeV neutron-capture gamma-ray source. This presumably reflects differences in the acceleration and/or transport processes for ions and electrons, respectively (Vilmer et al. 2011). A similar, but smaller, separation was also detected for the “Halloween” flare SOL2003-10-28T11:10 (X17.2) (Hurford et al. 2006).

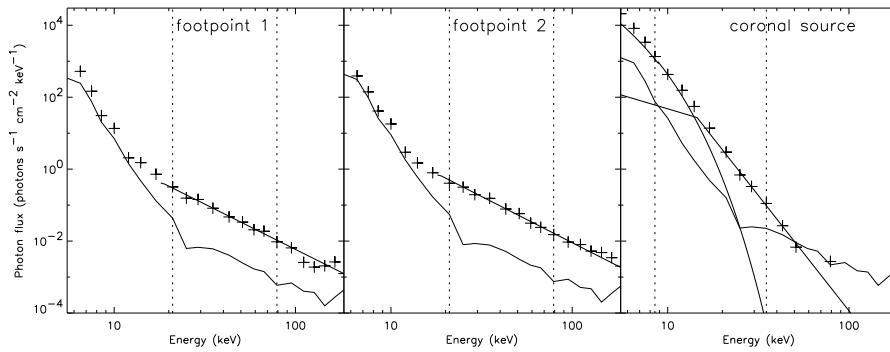


Fig. 2.4 Comparison of the spectra of the footpoint and coronal sources of SOL2005-07-13T14:49 (M5.0). *Left and middle panels:* Footpoint spectra. A power-law has been fit between the dotted vertical lines. *Right panel:* Spectrum of the coronal source. A power-law plus an isothermal spectrum has been fit between the dotted vertical lines. The bold line is the power-law fit in the dashed interval and a Maxwellian fit for the coronal source at low-energies. The thin curve is the background (mostly instrumental) determined at a location outside the enhanced flare emission. From Battaglia & Benz (2006).

2.4 Hard X-ray and radio emission

The information obtained through study of radio emission from solar flares complements that obtained from analysis of hard X-ray emission in several ways (White et al. 2011). Radiation at centimeter and millimeter wavelengths is gyrosynchrotron emission originating from mildly relativistic electrons with energies above about ~ 100 keV. Analysis of this emission hence permits an estimate of the ambient magnetic field strength, reported to be ~ 200 G in the corona (White et al. 2011). Coronal sources have been observed to emit in centimeter radio emission even before X-ray footpoints appear (Asai et al. 2006), suggesting that the pre-flare heating may not be unrelated to acceleration in the main phase. Comparison of radio and hard X-ray emissions by Benz et al. (2006) also revealed, in some events, coherent radio emission *after the hard X-ray emission had stopped* (this phenomenon was, however, reported in only 5% of the flares studied). Gyrosynchrotron radio emission in flares in general correlates well with hard X-rays in *time* but not in *space* (Krucker et al. 2008b; White et al. 2011); in addition, the electron spectra deduced from the radio emission are typically harder than the electron spectra deduced from the hard X-ray emission. Flare emission at decimeter wavelengths concurrent with hard X-rays has also been found to originate from different locations: for example, Battaglia & Benz (2009) report the origin of associated decimetric spike sources separated by some $100''$ from the coronal X-ray source.

Emission at meter and decimeter wavelengths originates not from individual particles, but from coherent radiation processes associated with various plasma waves. Benz et al. (2005) have studied the association of *RHESSI* hard X-rays with coherent radio emission in the meter and decimeter band in 201 flares with flare classes larger than C5. They found that coherent radio emission occurred before the onset of hard X-ray emission in 9% of the flares studied. Most of the radio emission was type III radiation at the plasma frequency and its first harmonic, emitted by a beam of electrons moving upward in the solar atmosphere into regions of progressively lower density. In a few cases, they also found a pulsating continuum, possibly caused by cyclotron maser emission. Both types of emission indicate the presence of electron acceleration in the pre-flare phase, which is often accompanied by

X-ray emission from a thermal source in the corona (Krucker et al. 2008a; Fletcher et al. 2011).

Emission at higher frequencies, such as decimetric narrow-band spikes, pulsations, and stationary Type IV events, correlate more frequently with the hard X-ray flux and thus appear to be more directly related to the acceleration process (Arzner & Benz 2005). While there is a good *association* between coherent radio emission and hard X-rays, a strong *correlation* in the details of the time profile is less frequent, so that coherent emission is not a reliable proxy for the main flare energy release. This can be accounted for by invoking multiple reconnection sites connected by common field lines, along which accelerated particles propagate and serve as a trigger for acceleration in other regions at some distance (Benz et al. 2005).

2.5 Magnetic field changes associated with the flare

Sharp temporal increases of hard X-ray emission are often closely correlated in time with variations of the magnetic field measured on the photosphere (see, e.g., Kosovichev & Zharkova 2001; Sudol & Harvey 2005; Wang et al. 2005; Zharkova et al. 2005). For example, in the flare SOL2002-07-23T00:35 (X4.8), the magnetic flux change over the flare duration was about 1.2×10^{21} Mx, most of which was concentrated in the area spanned by the magnetic inversion line. Such magnetic field changes are irreversible: the magnetic field reaches a new steady state and does not return to its pre-flare value (Kosovichev & Zharkova 2001; Sudol & Harvey 2005; Zharkova et al. 2005). Cross-correlation analysis with a time lag between the temporal variations of magnetic field covering the neutral line and the hard X-ray light curve reveals a significant positive correlation with a time difference less than ~ 100 s. This observation strengthens the theoretical notion that irreversible changes in the magnetic field are responsible for the initiation and development of the flare phenomenon.

3 Models of Particle Acceleration

In this Section, we first review some basic concepts, such as acceleration by a direct electric field in a plasma environment (Section 3.1) and magnetic reconnection (Section 3.2), in which magnetic energy is released into various forms, including the acceleration of charged particles, both electrons and ions. Recognizing the strong observational evidence for the formation of current sheets (localized regions in which a strong magnetic shear is present) in solar flares, our initial discussion relates to traditional two-dimensional (2-D) current sheets, with subsequent elaboration to the three-dimensional (3-D) case (Section 3.3). Two likely products of the fundamental reconnection process are magnetohydrodynamic shocks and stochastic MHD turbulence, and particle acceleration by these agents is discussed in Section 3.4.

3.1 Basic physics

As remarked in Section 1, the essential physics of particle acceleration is in principle rather straightforward – charged particles gain energy when subjected to an electric field in their rest frame. Such an electric field \mathbf{E} may be a large-scale externally-imposed field, or a $\mathbf{v} \times \mathbf{B}$ field associated with particles crossing magnetic field lines, or a collective field associated

with the environment in which the particle finds itself (e.g., a collisional Coulomb field or a field associated with a level of plasma wave energy). The richness of these various means of creating local electric fields is reflected in the richness of particle acceleration models in magnetized plasmas.

One of the most basic concepts is that of the *Dreicer field* (Chen 1974). Consider an electron subject to an externally-imposed large-scale electric field E , plus the frictional force due to collisions with stationary ambient particles. The equation of motion for such a particle is (in one dimension)

$$\frac{dv}{dt} = eE/m - f_c v, \quad (3.1)$$

where m and e are the electron mass and (absolute value of) charge, f_c is the collision frequency, and v is the velocity. Since for Coulomb collisions $f_c \sim v^{-3}$ (e.g., Chen 1974), we may write this as

$$m \frac{dv}{dt} = e \left(E - E_D \left[\frac{v_{\text{th}}}{v} \right]^2 \right), \quad (3.2)$$

where v_{th} is the electron thermal speed and we have defined the *Dreicer field* by

$$E_D = \frac{f_c(v_{\text{th}}) v_{\text{th}}}{e}; \quad (3.3)$$

numerically, $E_D \simeq 10^{-8} n(\text{cm}^{-3})/T(\text{K}) \text{ V cm}^{-1}$.

If $E < E_D$, then only high-velocity particles ($v > v_{\text{crit}} = v_{\text{th}}[E_D/E]^{1/2}$) see a net positive force and gain velocity. This increased velocity reduces the drag force, leading to an even greater net acceleration and eventual runaway acceleration. In contrast, particles with $v < v_{\text{crit}}$ suffer a net *retardation* force and are not accelerated; they remain part of the collisionally-redistributed Maxwellian core. For a Maxwellian distribution of velocities, the number density of accelerated particles $\int_{v_{\text{crit}}}^{\infty} f(v) dv$ (where $f(v)$ is the phase-space distribution function) is a (rapidly) increasing function of E . If $E > E_D$, all particles with velocity in excess of the thermal speed v_{th} are accelerated, and the efficient collisional re-population of the accelerated electrons thus leads effectively to acceleration of *all* the electrons in the distribution.

3.2 Magnetic reconnection models associated with flares

It is generally accepted that the energy release in solar flares occurs through a reconstruction of the magnetic field, caused by the change of connectivity of magnetic field lines during a magnetic *reconnection*. The electric field associated with this changing magnetic field and/or with the associated driven currents leads to particle acceleration.

Reconnection is a fundamental process defined by the magnetohydrodynamics of a magnetized plasma (see Priest & Forbes 2000). The magnetic diffusion equation (see, e.g., equation (3.91) of Tandberg-Hanssen & Emslie 1988) is

$$\frac{\partial \mathbf{B}}{\partial t} = \nabla \times (\mathbf{v} \times \mathbf{B}) + \frac{\eta c^2}{4\pi} \nabla^2 \mathbf{B}, \quad (3.4)$$

where c is the speed of light, \mathbf{B} is the magnetic field, \mathbf{v} the fluid velocity and η the resistivity. The order-of-magnitude ratio of the terms on the right side of this equation defines the *magnetic Reynolds number*

$$R_m = \frac{4\pi \ell V}{\eta c^2}; \quad (3.5)$$

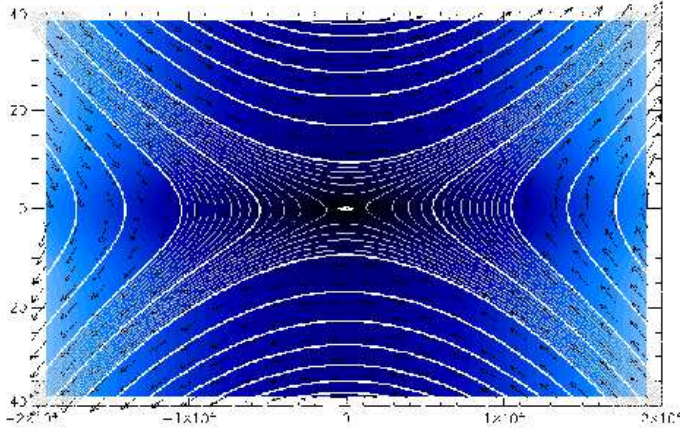


Fig. 3.1 Topology of the reconnecting magnetic field lines in the vicinity of an X-null point $B_y = \pm\alpha B_x$.

it measures the ratio of the advective to diffusive contributions to the change in the magnetic field. For typical solar coronal values of η and with $\ell \approx 10^9$ cm, $R_m \approx 10^{14}$; for such high magnetic Reynolds numbers, the plasma is effectively “frozen-in” to the field and negligible change in the field topology, with its concomitant release of magnetic energy, can occur. A topological change in the magnetic field requires a breakdown in this ideal “frozen-in” flux condition; by Equation 3.5, this can occur either in small-scale regions (high values of $\nabla^2 \mathbf{B}$) and/or in regions in which the resistivity η is anomalously enhanced. As a result, magnetic reconnection fundamentally occurs in narrow boundary layers called *diffusion regions*.

3.2.1 Basic 2-D MHD theory of magnetic reconnection

In the simple neutral sheet geometry originally proposed by Sweet and Parker (Sweet 1969), oppositely-directed magnetic field lines \mathbf{B} in close proximity follow a plasma inflow \mathbf{V}_i oriented in the x -direction perpendicular to the field lines – see Figure 3.1, where the x -direction is vertical and the y -direction horizontal (note that there does exist evidence for such reconnection geometries in flares – Aulanier et al. 2000; Fletcher et al. 2001; Sui & Holman 2003; Des Jardins et al. 2009). The increasing magnetic pressure in the localized region of field reversal is alleviated by reconnection in a small region of high $\nabla^2 \mathbf{B}$ near the origin, which allows plasma outflows with velocity V_o toward the sides of the diffusion region.

The original analysis by Sweet (1969) showed that the reconnection rate V_i is given by

$$\frac{V_i}{V_A} = \frac{2}{\sqrt{R_m}}, \quad (3.6)$$

where V_A is the Alfvén velocity. Because of the $R_m^{-1/2}$ dependence on the inflow velocity, and hence on the rate of magnetic energy dissipation, such a neutral sheet scenario describes a “slow” magnetic reconnection regime. In an effort to increase the reconnection rate, Petschek (1964) proposed a model involving the formation of shocks propagating outward from the diffusion region; in this scenario, the reconnection process occurs at a

significantly faster rate, with $V_i \approx V_A$. Both these models were originally proposed with a classical value for the resistivity η and both resulted in reconnection rates too slow to explain the rapid energy release observed in flares. However, later realization that the resistivity in the reconnection region may be driven to anomalously high values through the presence of plasma instabilities in the current sheet (see, for example, Dahlburg et al. 1992; Bret 2009, and references therein). These include the lower hybrid drift instability leading to the Kelvin-Helmholtz instability (Landau & Lifshitz 1960; Chen et al. 1997; Lapenta et al. 2003), the kink instability (Pritchett et al. 1996; Zhu & Winglee 1996; Daughton 1999), the sausage instability (Büchner 1999) and magneto-acoustic waves (Schekochihin & Cowley 2007). This realization revived hopes that reconnection mechanisms could indeed be a viable candidate for the energy release in flares (Syrovatskii 1981; Priest 1982; Somov 2000). Questions remaining about the stability of current sheet geometries such as those envisioned by Sweet and Parker have been extensively investigated using a full kinetic approach (see Daughton et al. 2009, and references therein), and are discussed further in Section 4.8.

Another simple 2-D diffusion region geometry involves magnetic field lines of the form $B_y^2 = \alpha^2 B_x^2$. Such a form is associated with two types of neutral point: an O-type, elliptic topology ($\alpha^2 < 0$; see Section 4.9), and an X-type, hyperbolic topology ($\alpha^2 > 0$; see Section 3.3; Figure 3.1).

3.2.2 Effect of the Hall current on reconnection rates in 2-D models

In the conductive plasma within the diffusive region where reconnection occurs, the current sheet tends to diffuse outwards at a slow rate with a timescale of $\tau_{\text{dif}} = a^2 \varpi$ where a is the current sheet half-width and ϖ is the magnetic diffusivity (Priest & Forbes 2000). This diffusion process ohmically converts magnetic energy into heat. As discussed in Section 3.3, this timescale is too slow to account for the fast reconnection rates observed in the impulsive phase of flares unless some other processes, such as resistive instabilities or Hall current effects, are invoked to enhance the reconnection process. The effects of the Hall current in MHD models of the reconnection process are now discussed. Its effects in particle-in-cell (PIC) models will be discussed in Section 4.8, while the effect of resistive instabilities will be discussed in Section 4.9.

The basic Sweet-Parker 2-D reconnection model discussed above can produce more realistic reconnection rates if, instead of a resistive MHD model, one uses a two-fluid MHD model, which includes in the equation of motion a Hall current (Sonnerup 1979). Use of a two-fluid model means that the velocity vector \mathbf{v} in Equation 3.4 now represents the velocity \mathbf{V} of the plasma as a whole, with an additional vector \mathbf{V}_H representing the relative velocity between the electrons and the ions. The *Hall current* results from the fact that, inside the current sheet, the electrons and ions are magnetized to significantly different degrees – the spatial scales for effective magnetization is c/ω_{pe} for electrons and c/ω_{pi} for protons. (Here ω_{pe} and ω_{pi} are the respective plasma frequencies, which are in the ratio of the square root of the proton-to-electron mass ratio $\sqrt{m_p/m_e} \simeq 43$.)

At length scales between c/ω_{pe} and c/ω_{pi} , the motions of the electrons and ions are decoupled, and the current generated from the relative motion of electrons and ions can lead to the formation of whistler waves (Mandt et al. 1994a; Ma & Bhattacharjee 1996; Drake et al. 1997; Biskamp 1997). Inside such a region, the reconnection rate becomes insensitive to electron inertia, allowing the reconnection rates to be strongly increased to levels large enough to account for those measured in solar flares (Birn et al. 2001; Huba & Rudakov 2004). These results indicate a compelling need to consider a full kinetic approach for mod-

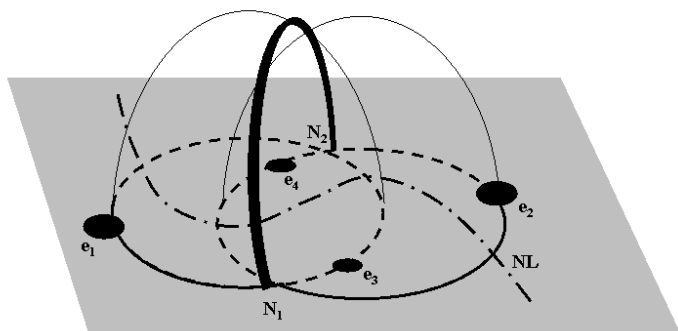


Fig. 3.2 The magnetic field geometry formed by four point-like sources of different magnetic polarity. The dot-dashed line labelled ‘NL’ is the neutral line. The *separatrix* surfaces are shown as thin dome-like lines connecting the photospheric sources. The intersection of these surfaces is the *separator*, shown as a solid line. From Titov & Hornig (2002).

eling magnetic reconnection processes in the diffusion region (for details, see Birn et al. 2001, and references therein); this will be discussed in more detail in Sections 4.8 and 4.9.

3.2.3 Further improvement of reconnection models

It must be recognized that magnetic reconnection is inherently a 3-D process, and that the addition of the third dimension inherently introduces fundamentally new physics. (As an elementary example, 2-D models may predict unrealistic energy gains since the induced electric field $\mathbf{E} = (\mathbf{V}/c) \times \mathbf{B}$ is infinite in extent in the invariant direction). In three dimensions, the magnetic field has a considerably more complicated structure (Figure 3.2), involving *separatrices* and *separators* (surfaces separating different domains of magnetic connectivity, and lines of intersection of separatrix surfaces, respectively; see Priest & Démoulin 1995; Démoulin et al. 1996; Demoulin et al. 1996). As shown by Priest & Démoulin (1995), magnetic null points are no longer required for reconnection to take place, and, even when they do exist, magnetic nulls have a more complicated structure, typically involving a “fan” structure oriented around an axial “spine” (Priest et al. 1997).

In summary, reconnection can proceed in a variety of different magnetic field geometries and topologies (Priest & Forbes 2002). Furthermore, depending on the magnetic field configuration, reconnection can be accompanied by a variety of other physical processes such as generation of plasma waves, turbulence and shocks, each occurring on different temporal and spatial scales. These additional processes not only directly accelerate particles (e.g., in regions of enhanced magnetic field, which act as moving “mirrors”), but can also feed back on the magnetic field topology and hence the ongoing reconnection rate.

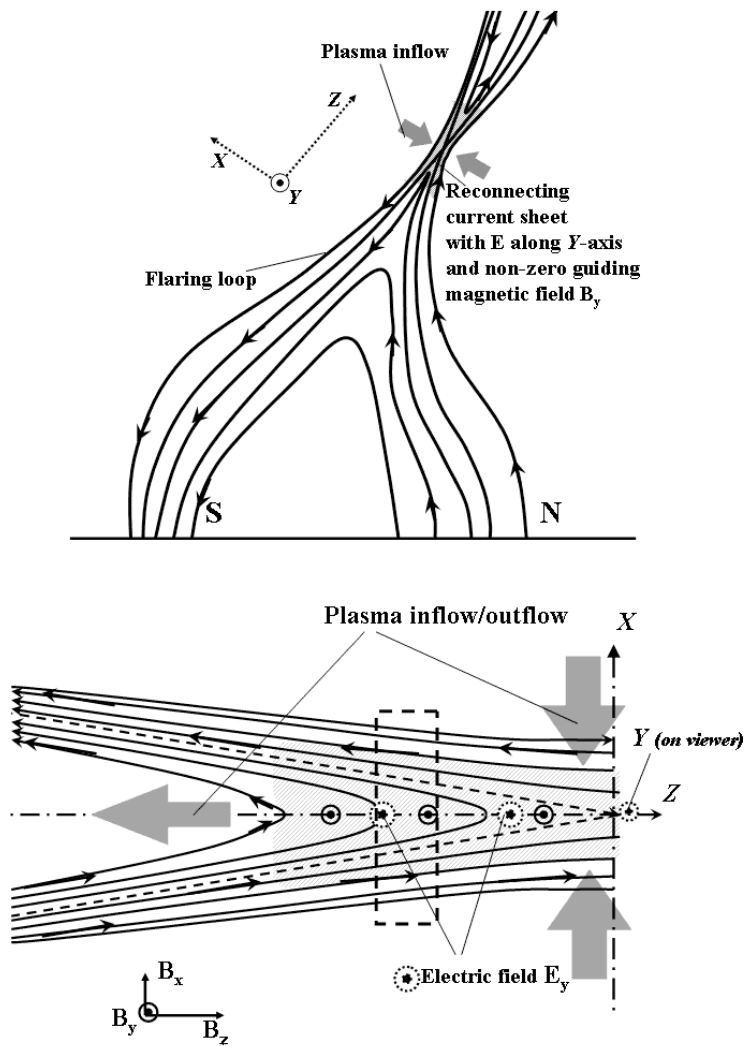


Fig. 3.3 *Top*: current-sheet location and *bottom* magnetic-field topology in a single helmet-type reconnecting non-neutral current sheet. The large arrows depict plasma inflows from the top and the bottom and outflows to the side. The x - and z -components of the magnetic field lie in the plane of the Figure; a guiding magnetic-field component B_y and a drift electric field E_y are perpendicular to the plane.

3.3 Particle acceleration in a reconnecting current sheet

Two of the most popular magnetic field topologies associated with solar flares involve the formation of a current sheet (Gorbachev & Somov 1989; Sui & Holman 2003), located either at the top of single helmet-like loop (Figure 3.3) or at the intersection of two interacting loops (Figure 3.4). Other more complicated topologies are essentially combinations of these two basic ones, and they are discussed in Section 4. In this Section we therefore briefly overview the basic physics of particle acceleration in reconnecting current sheets.

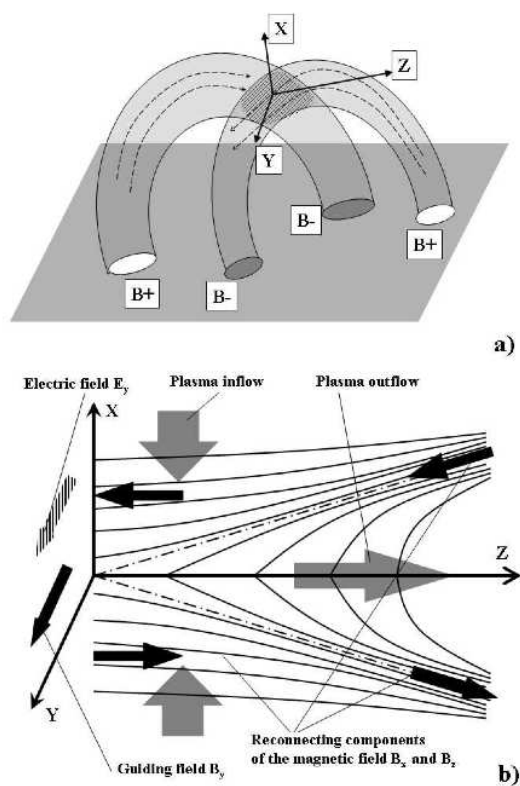


Fig. 3.4 *Top*: current sheet location, and *bottom*: magnetic-field topology in a reconnecting non-neutral current sheet formed by two interacting loops. The large arrows depict the plasma inflows. As for Figure 3.3, the x - and z -components of the magnetic field lie in the plane of the Figure; a guiding magnetic field component B_y and a drift electric field E_y are perpendicular to the plane.

Let us, then, consider the magnetic field topology as presented in the reconnecting current sheet (RCS) geometries illustrated in bottom plots of Figures 3.3 and 3.4. The tangential magnetic field component $B_z(x)$ is approximated by the linear function

$$B_z(x) = B_0 \left(-\frac{x}{d} \right), \quad (3.7)$$

where d is the RCS thickness (Martens & Young 1990; Litvinenko & Somov 1993b). The width a of an RCS in the z -direction approaches $10^2 - 10^3$ m (Somov 1992) and magnitudes

of the other two magnetic field components B_x and B_y are assumed to be constant:

$$|B_x| = B_{x0}, \quad |B_y| = B_{y0}. \quad (3.8)$$

Particles, effectively frozen into the field lines, are advected toward the RCS plane (the x -axis) by the flow field \mathbf{V}_i , where they are accelerated by the $(\mathbf{V}_i/c) \times \mathbf{B}$ electric field (Bulanov & Syrovatskii 1976; Litvinenko & Somov 1993b; Litvinenko 1996b). As the reconnection process continues, ambient particles drift into the reconnecting current sheet; the rate of acceleration of particles is limited by the size of the thin diffusion region.

The induced electric field E_y is given by (Bulanov & Syrovatskii 1976; Martens & Young 1990; Litvinenko & Somov 1993b; Zharkova & Gordovskyy 2004):

$$E_y = \frac{V_i B_{z0}}{c} - \frac{\eta c}{4\pi} \frac{\partial B_z}{\partial x}; \quad (3.9)$$

the first and second terms on the right hand side of Equation 3.9 dominate outside and inside the diffusion region, respectively (Somov 2000). Priest (1982) has shown that the plasma inflow velocity V_i is smaller than the local Alfvén speed by about two orders of magnitude, i.e., $V_i \approx 0.01V_A$. Hence the electric field is

$$E_y \approx 0.01 \frac{B_{z0}^2}{c \sqrt{4\pi n m_p}}, \quad (3.10)$$

where m_p is the proton mass. Let us assume the following physical conditions in the current sheet: temperature $T = 10^6$ K, density $n = 10^{10} \text{ cm}^{-3}$, and $B_{z0} \approx 100$ G. Then $V_A \approx 2 \times 10^6 \text{ m s}^{-1}$ and the thermal velocities are about 10^5 m s^{-1} for protons and 10^7 m s^{-1} for electrons. Taking the initial inflow velocity V_i to be the proton thermal speed, we obtain $E_y \approx 2 \text{ V cm}^{-1}$, which is roughly four orders of magnitude higher than the corresponding Dreicer field $\sim 10^{-4} \text{ V cm}^{-1}$ (Martens & Young 1990; Litvinenko 1996b, see Section 3.1). This electric field is directed along the longitudinal magnetic field component B_y , allowing efficient particle acceleration in the y -direction.

In these simulations the drifted, or reconnection, electric field is assumed to exist throughout the entire diffusion region, which in the MHD approach extends over some 10^2 m to 10^6 m (Bulanov & Syrovatskii 1976; Somov 1992; Oreshina & Somov 2000a). This assumption has been challenged by full kinetic PIC simulations (Furth et al. 1963; Drake & Lee 1977), which show the reconnection field to extend over a relatively small domain corresponding to the size of the electron diffusion region. Given the current limitations of PIC simulations (see Section 4.10), there is at present no definitive indication of which of the approaches (MHD or PIC) is more valid. In the remainder of this Section we adopt the value provided by the MHD approach, recognizing that appropriate caveats must therefore be made.

The magnitudes of the magnetic field components B_x and B_y are chosen such that electrons remain magnetized in the vicinity of the midplane while protons are unmagnetized during the acceleration phase. In this case, the energy of the unmagnetized protons upon ejection can be estimated (see Litvinenko 1996b) as:

$$\varepsilon = 2m_\alpha c^2 \left(\frac{E_{y0}}{B_{x0}} \right)^2, \quad (3.11)$$

where m_α is the particle mass. However, since the electrons are magnetized, they follow magnetic field lines and gain an energy (Litvinenko 1996b):

$$\varepsilon = d \left| e E_{y0} \frac{B_{y0}}{B_{x0}} \right|. \quad (3.12)$$

where d is the current sheet thickness along the x -direction (see the bottom plot in Figure 3.3). For RCSs with thicknesses from 1 m to 100 m, corresponding to proton Larmor radii in magnetic fields from 10^{-3} T to 2×10^{-2} T, electrons gain energies up to ~ 100 keV, comparable with those of bremsstrahlung-emitting electrons.

Although such a model does meet the challenge of (1) a sufficiently high reconnection rate and (2) sufficient energy gain by the accelerated electrons, the number of accelerated particles is fundamentally limited by the small width $2a$ of the current sheet. These deficiencies are addressed in the further development of this basic model to include three-dimensional considerations (Section 4.4), the use of multiple current sheets formed by the filamentation of the reconnection region (Section 4.6), and a full kinetic PIC approach to model portions of a 3-D current sheet (Sections 4.8 and 4.9).

3.4 Particle acceleration by shocks and turbulence

In this Section, we review the basic physics involved in acceleration models that do not rely on a large-scale coherent electric field.

3.4.1 Shock acceleration

Ever since the demonstration by several authors (Blandford & Ostriker 1978; Bell 1978; Cargill 1991; Giacalone & Jokipii 1996) that a very simple model of shock wave acceleration leads to a power-law spectrum of the accelerated particles (in good agreement with observations of galactic cosmic rays), shock acceleration has been frequently invoked in both space and astrophysical plasma contexts. However, this simple model, though very elegant, has a significant number of shortcomings. Inclusion of losses (Coulomb at low energies and synchrotron at high energies) or the influence of accelerated particles on the shock structure (see, e.g., Amato & Blasi 2005; Ellison & et al. 2005) can cause significant deviations from a simple power law.

Moreover, shocks are unable to accelerate low energy background particles efficiently; shock acceleration requires the injection of (fairly high energy) “seed” particles. Also, shock acceleration requires some scattering agents (most likely plasma waves or turbulence) to cause repeated passage of the particles through the shock front. In the case of quasi-parallel shocks, in which the magnetic field is nearly parallel to the normal of the shock front, the rate of energy gain is governed by the pitch-angle diffusion rate.

As pointed out by Wu (1983) and Leroy & Mangeney (1984), in the Earth’s magnetosphere, many shocks can be quasi-perpendicular (i.e., the vector defining the normal to the shock is almost perpendicular to the shock velocity vector). In such a case the particles drift primarily along the surface of the shock and get accelerated more efficiently. However, acceleration in quasi-perpendicular shocks suffers from the fundamental limitation that injection of seed particles with very large velocities $v > u_{sh}\xi$ (where u_{sh} is the shock speed and $\xi \gg 1$ is the ratio of parallel to perpendicular diffusion coefficients) is required (Amano & Hoshino 2010). Moreover, although there may be some *indirect* morphological evidence for the existence of such shocks in flares (see, e.g., Sui & Holman 2003), there is little *direct* evidence for the occurrence of these kinds of shocks near the top of flaring loop, where the acceleration seems to be taking place during the impulsive phase. Furthermore, such shocks typically do not appear in 3-D MHD simulations of the reconnection process.

In summary, many of the features that make acceleration of cosmic rays by shocks attractive are not directly applicable to the solar flare environment. As a result, this mecha-

nism has, with some justification, received only limited attention in the literature. However, in Section 4.3.2 we do discuss the possibility of acceleration at fast magnetosonic shocks resulting from reconnection.

3.4.2 Stochastic Acceleration

A main contender for the particle acceleration mechanism in flares is stochastic acceleration by the magnetic field component of low-frequency magneto-acoustic waves (Miller et al. 1997; Schlickeiser & Miller 1998; Petrosian et al. 2006).

In the originally proposed Fermi acceleration process (Fermi 1949; Davis 1956), particles of velocity v scatter coherently off agents moving toward each other with a velocity $\pm u$. Since the velocity gain in a single collision is $2u$, the rate of velocity increase is $\Delta v/\Delta t \approx 2u/(L/v)$, where L is the separation of the scattering centers. Solving this, for the case in which a scatter occurs on a timescale significantly less than that required for L to decrease, shows that the energy grows exponentially with time: $E \propto e^{4ut/L}$. For particles scattering off *randomly* moving agents, both energy gains and losses are possible. However, the increased likelihood of a head-on (energy-increasing) collision leads to a general (slower than exponential) increase in energy, at a rate proportional to $(u/v)^2 D_{\mu\mu}$, where $D_{\mu\mu}$ is the angular diffusion coefficient. This process is known as *second-order* Fermi acceleration.

In general, in a magnetized plasma characterized by a gyrofrequency Ω , a particle of velocity \mathbf{v} will resonate with a wave of frequency ω and wavenumber \mathbf{k} when

$$\omega = \mathbf{k} \cdot \mathbf{v} - \ell \Omega, \quad (3.13)$$

where ℓ is an integer. Particles with velocities near the Cherenkov resonance ($v \approx \omega/k_{\parallel}$) resonate with $\ell = 0$ waves. This process is known as *transit-time damping* (Hollweg 1974, and references therein). It acts to diffuse the particle distribution $f(\mathbf{p})$ in momentum space, described by the Fokker-Planck equation

$$\frac{\partial f(\mathbf{p})}{\partial t} = \left(\frac{1}{2} \sum_{i,j} \frac{\partial}{\partial p_i \partial p_j} D_{ij} - \sum_i \frac{\partial}{\partial p_i} F_i \right) f(\mathbf{p}) + Q(\mathbf{p}) - S(\mathbf{p})f(\mathbf{p}). \quad (3.14)$$

The diffusion coefficient D_{ij} and the secular coefficient F_i ($i = 1, 2$ correspond to energy and angular terms, respectively) contain the essential physics: the action of both the accelerating waves and decelerating effects (e.g., Coulomb collisions); the quantity $Q(\mathbf{p})$ corresponds to the injection of particle energy and the term $S(\mathbf{p})f(\mathbf{p})$ to escape.

For solar flares, the most likely sources for the energization term $Q(\mathbf{p})$ are plasma wave turbulence (Hamilton & Petrosian 1992; Pryadko & Petrosian 1997) and cascading MHD turbulence (Miller et al. 1996). In the first scenario, a presupposed level of plasma wave turbulence in the ambient plasma accelerates ambient particles of energy E stochastically with the rate D_{EE}/E^2 . It has been shown (e.g., Hamilton & Petrosian 1992; Miller et al. 1996) that for flare conditions, plasma-wave turbulence can accelerate the background particles to the required high energies within the very short timescale derived from hard X-ray observations. More importantly, at low energies, and especially in strongly magnetized plasmas, the acceleration rate D_{EE}/E^2 of the ambient electrons may significantly exceed the scattering rate $D_{\mu\mu}$ for particular pitch angles and directions of propagation of this turbulence (Pryadko & Petrosian 1997, 1998), leading to an efficient acceleration. However, high-frequency waves near the plasma frequency are problematic as drivers for stochastic acceleration in flares, because they would couple into decimeter radio waves and would be present at high levels in every flare, contrary to observations (Benz et al. 2005).

In the second scenario, involving cascading MHD turbulence, moving magnetic compressions associated with fast-mode MHD waves propagating at an angle to the magnetic field constitute the scattering centers. The wavelength of the induced MHD turbulence is assumed to cascade through an inertial range from large to very small, stopping at the point where wave dissipation becomes significant due to transit-time damping. Resonance with one wave will result in an energy change leading to resonance with a neighboring wave, and so on (Miller et al. 1996). Electrons can thus be accelerated all the way from thermal to relativistic energies through a series of overlapping resonances with low-amplitude fast-mode waves in a continuum broad-band spectrum.

In order to be efficiently accelerated, the test particle must have an initial speed that is greater than the speed of the magnetic compression, i.e., of order the Alfvén speed. For the pre-flare solar corona, *electrons* have speeds comparable to, or greater than, the Alfvén speed, and so are efficiently accelerated immediately. On the other hand, in a low- β plasma, the protons necessarily have an initial speed that is less than the Alfvén speed and so are not efficiently accelerated: the scattering centers converge before the test particle has suffered a sufficient number of energy-enhancing collisions. Efficient acceleration of ions therefore requires pre-acceleration to Alfvén speeds. In the model of Miller & Roberts (1995), this pre-acceleration is accomplished through (parallel-propagating) Alfvén waves, and it is essential to realize that *this process takes some time to accomplish*. During this pre-acceleration period, most of the energy is deposited in accelerated electrons; only after the protons are pre-accelerated to the Alfvén speed are they effectively accelerated – they then gain the bulk of the released energy by virtue of their greater mass (Miller & Roberts 1995). As explained by Emslie et al. (2004), this may be the explanation for the different locations of hard X-ray and gamma-ray sources in flares (see Section 2.3 and Hurford et al. 2003, 2006); efficient proton acceleration requires relatively long trapping times and so a larger magnetic structure, whereas electrons can be efficiently accelerated even in relatively small structures.

In practice, since there is a little difference *mathematically* between the plasma wave turbulence and shock mechanisms (Jones 1994), acceleration by both turbulence and shocks can be effectively combined. It should be also be noted that stochastic acceleration generally predicts an accelerated spectrum that is not a strict power-law, but rather steepens with increasing energy (e.g., Miller et al. 1996). However, a recent development in transit-time damping theory involves adding both the loss term $S(\mathbf{p})$ in Equation 3.14 that allows electron escape, and a source term $Q(\mathbf{p})$ due to the return current replenishing the electrons in the acceleration region. These additions cause the solution to become stationary within less than one second under coronal conditions (Grigis & Benz 2006); furthermore, in the hard X-ray spectral region of observed non-thermal energies, the photon distribution is close to a power law, in agreement with observation. The predicted spectral index γ depends on the wave energy density and on the interaction time between the electrons and the waves. Additional trapping (e.g., by an electric potential) tends to harden the electron spectrum.

The main limitation of stochastic acceleration models at this juncture is the need to presuppose an *ad hoc* injection of the necessary waves (plasma or MHD). Furthermore, in the absence of pitch-angle scattering, the stochastic acceleration process generally leads to a decrease in particle pitch angles. This, in turn, reduces the efficiency of the acceleration process, since now only waves with very high parallel phase speeds, or those with pitch angles near 90° , can resonate with the particles being accelerated. Therefore, in order for significant stochastic acceleration to occur, the effective particle scattering rate (which is proportional to the collision frequency between particles and waves) must be greater than the frequency of Coulomb collisions between the charged particles. The latter condition

imposes rather strict limitations on the growth rates of plasma waves or MHD turbulence, as appropriate.

4 Recent Theoretical Developments

In this Section, we highlight some recent promising developments in our understanding of the physics of particle acceleration in the magnetized plasma environment associated with solar flares.

In Section 4.1, we turn our attention to some recent advances in stochastic acceleration models, namely the inclusion of (1) small-scale electric fields and (2) feedback of the accelerated particles on the turbulence level in the acceleration region. Some ideas on possible particle acceleration by large-scale Alfvén waves in a large-scale closed magnetic configuration are discussed in Section 4.2.

In Section 4.3, the evolution of the ubiquitous “helmet”-type magnetic field configuration observed in flaring regions is presented. We point out two likely acceleration regions in such a geometry: the collapse of previously-stretched field lines onto a closed magnetic loop (which leads to acceleration by both first-order Fermi and betatron processes, associated with the shrinking and compression of field line bundles, respectively), and the formation of “termination” shocks associated with high-speed jets, which accelerate particles through shock-drift acceleration.

In Section 4.4, we consider particle trajectories in a realistic 3-D current sheet geometry, considering, in particular, the asymmetric acceleration of electrons and ions and the resulting particle energy spectra, which turn out to be power laws. In Section 4.5, we discuss particle acceleration in 3-D magnetic field configurations, in which magnetic nulls have a fundamentally different topological structure than they do in a simple 2-D reconnection geometry. Both “fan” and “spine” reconnection modes are considered, and the resulting (rather hard power-law) spectra of the accelerated particles are presented.

In Section 4.6, we turn our attention to acceleration in *multiple* acceleration sites, considering cellular automaton (CA) models, MHD turbulent environments, and stochastic acceleration in a distribution of elementary current sheet sites.

In Section 4.7, we turn our attention to a critical aspect of all acceleration models – the need to recognize that, since a substantial fraction of the magnetic energy released in flares appears in the form of accelerated particles, these particles simply cannot be considered as an ensemble of test particles interacting with a *prescribed* electrodynamic environment. Rather, the electric and magnetic fields generated by the accelerated particles themselves are an essential element of this environment; the self-consistent inclusion of these fields represent a paramount consideration in acceleration models, without which unphysical and even paradoxical conclusions can result. We review the limitations of existing acceleration models in this context. In Section 4.8, we discuss recent attempts to include this electrodynamic feedback through the use of PIC models, for which the self-consistent electric and magnetic fields associated with the accelerated particles *do* form an essential element of the modeling. Finally, in Section 4.9, we briefly discuss a mechanism for particle acceleration that involves multiple small-scale closed magnetic “islands” formed by the tearing-mode instability in a reconnecting current sheet.

4.1 Stochastic acceleration

As discussed in Section 2.1, the low value of the low-energy cutoff of the electron energy distribution suggested by *RHESSI* observations (Kontar et al. 2005; Saint-Hilaire & Benz 2005) has significant implications for the number of accelerated flare electrons. Indeed, for sufficiently low cutoff energies, the number of electrons required in a collisional thick-target model (Brown 1971) becomes so great that models in which the accelerated particles form a subset of the ambient distribution become untenable. The only viable mechanism of particle acceleration is then acceleration of the entire plasma within the acceleration region through a stochastic process that results in little or no net electrical current, to avoid the issues presented in Section 2.1.

As discussed in Section 3.4, high-frequency waves near the plasma frequency are problematic as drivers for stochastic acceleration, because they would couple into decimeter radio waves and would be present at high levels in every flare, contrary to observations (Benz et al. 2005). On the other hand, acceleration by transit-time damping do not suffer from this drawback – the driving waves have a frequency that is far below the plasma frequency.

4.1.1 Improvements to the MHD stochastic acceleration model

The basic transit-time damping stochastic acceleration mechanism has been improved by adding low-frequency fluctuating electric fields parallel to the magnetic field (Grigis & Benz 2004, 2005). Such fields may originate from low-frequency and high-amplitude turbulence, such as kinetic Alfvén waves, as discussed in Section 5.1 (see also Miller et al. 1996; Pryadko & Petrosian 1997). They can accelerate and decelerate electrons (and protons), leading to a net diffusion in energy space (Arzner & Vlahos 2004). As for other models for stochastic acceleration, the authors assume an *ad hoc* distribution of turbulence. In this model, the non-thermal electron distributions in coronal sources “grow” out of the thermal population: the coronal source is initially purely thermal, then a soft non-thermal population develops, getting harder at the hard X-ray peak and softening toward the end of the emission.

As discussed in Section 2.1, such a “soft-hard-soft” behavior has been observed in a coronal source (Battaglia & Benz 2007). Indeed, Grigis & Benz (2004) report *RHESSI* observations suggesting the existence of a point in the spectrum at which the hard X-ray flux does not change with time during an event. Above this *pivot point* the spectral variation is consistent with the characteristic “soft-hard-soft” behavior of the photon spectrum. Note, however, that Zharkova & Gordovskyy (2006) have pointed out that such a “pivot-point” behavior in the variation of the hard X-ray spectrum with time could also be associated with an electron beam accelerated by the super-Dricer electric field in a current sheet and precipitating into a loop leg with the self-induced (return-current) electric field (e.g., Knight & Sturrock 1977; Emslie 1981) associated with an electron beam accelerated by a directed electric field.

4.1.2 Stochastic acceleration with particle feedback

A more self-consistent approach to stochastic acceleration was recently reported by Bykov & Fleishman (2009), who simulated electron acceleration by MHD waves, but included the effect on the MHD turbulence (spectrum and intensity) caused by the injection of high energy particle beams into the acceleration region. The initial MHD turbulence is prescribed, and is assumed to be produced in the form of transverse motions with a Gaussian spectrum on the

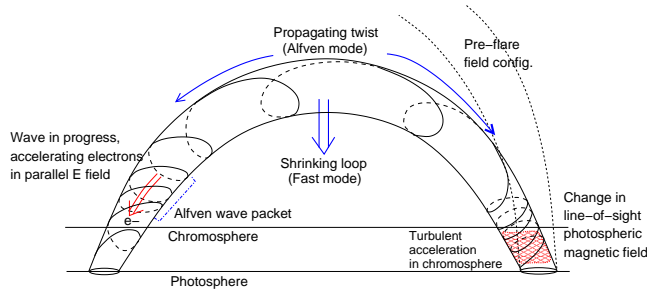


Fig. 4.1 The reconfiguring coronal field launches a torsional Alfvén wave pulse through the corona and into the chromosphere, as well as a fast-mode wave pulse. The Alfvén wave, which propagates in the inertial regime, can lead to electron acceleration in the corona. Any Alfvén wave energy entering the chromosphere can also lead to electron acceleration there. The wave will be partially reflected from the steep gradients in the chromosphere and then re-enter the corona (from Fletcher & Hudson 2008).

scale $2\pi/k_0$. Through mode coupling, this turbulence produces a corresponding level of longitudinal turbulence in a system of a finite size R (where $Rk_0 > 1$). The model includes only large scale energy-conserving motions, with the kinetics of particles on smaller scale being determined by turbulent advection, valid only for electron energies up to ~ 1 MeV (Bykov & Fleishman 2009); thus, the model can account for the feedback of the accelerated particles on the acceleration mechanism on large scales only. The phase-space diffusion coefficients D_{ij} in Equation 3.14 are expressed in terms of the spectral functions that describe correlations between large scale turbulent motions (for details, see Bykov & Toptygin 1993).

The model assumes a continuous injection of monoenergetic particles (both electrons and protons) into the acceleration region. The initial phase of the acceleration is characterized by a linear growth regime which results in effective particle acceleration by the longitudinal large scale turbulent motions and thus leads to a spectral hardening. However, because the accelerated particles eventually accumulate a considerable fraction of the turbulent energy, the efficiency of the acceleration decreases; this predominantly affects the higher-energy particles, leading to a spectral softening.

4.2 Particle acceleration by large-scale Alfvén waves

In this model, reconnection is still at the heart of the magnetic energy release process, in that it allows the pre-flare field to reconfigure, releasing the energy needed to power the flare. However, motivated by *in situ* observations and theories for energy transport and electron acceleration in the Earth's magnetosphere during sub-storms (Stasiewicz et al. 2000), it is suggested (Fletcher & Hudson 2008) that the energy is transported through the corona not by particle beams but by Alfvén-wave pulses, launched in the primary reconnection site and carrying a large Poynting flux towards the chromosphere. The presence of such pulses has recently been verified in MHD simulations by Birn et al. (2009). They may play a direct role in accelerating the electrons either in the field-aligned electric fields that they generate in the corona, or through the magnetic energy that they transport to the chromosphere, leading to acceleration of electrons locally in the chromosphere by mechanisms as yet unspecified. A cartoon realization of this model is shown in Figure 4.1.

To explain the rapid time variability observed in the flare time profiles, and also the simultaneity of hard X-ray footpoint sources within around 0.1 s, the wave pulses must move

quickly – on the order of $0.1c$, which is significantly larger than the values usually quoted for the coronal Alfvén speed. However, such speeds *are* consistent with the properties of the core of an active region before a flare, where the density may be 10^9 cm^{-3} or less, and the magnetic field on the order of a few hundred Gauss (e.g., Brosius & White 2006). Linear wave pulses traveling at such speeds do not damp significantly *en route* through the corona.

Fletcher & Hudson (2008) calculate that for a coronal field of 500 G and an ambient density of 10^9 cm^{-3} , a magnetic field perturbation of 50 G is more than enough to deliver sufficient Poynting flux to the chromosphere to produce the flare energies observed. Of course, such a perturbation, on the order of a few to 10%, does stretch the linear approximation for Alfvén waves. An ideal, incompressible, non-linear Alfvén mode traveling in a completely uniform plasma does not steepen into a shock, or dissipate due to Landau damping (Barnes & Hollweg 1974), but the presence of density fluctuations, including those generated by the wave itself, can lead it to decay via a parametric instability into a forward-propagating ion-acoustic wave and a backward-propagating Alfvén wave (e.g. Goldstein 1978).

Analytical work by Jayanti & Hollweg (1993) suggests that, in the low- β coronal regime, the maximum growth rate of this instability for a wave with an amplitude of a few percent is a few times the wave frequency, so that this decay occurs for all but long-wavelength perturbations. However, in the low- β case, the Alfvén speed exceeds the sound speed, so the front of the Alfvén wave train (and presumably also the front of a simple Alfvén wave pulse) propagates ahead of the ion-acoustic wave produced, and is, therefore, not significantly affected by the instability. This has been demonstrated by Turkmani & Torkelsson (2003) in numerical simulations for roughly the parameter regime of interest. The process has not yet been fully explored in an environment where collisionless damping is important, though this may be the case for coronal depths in flares.

Because the Alfvén speed in such an environment is so high (higher than the electron thermal speed, such that an average electron lags behind the wave), the details of the wave propagation require two-fluid or even full kinetic simulations. Such simulations performed in the case of the magnetosphere (Kletzing 1994) indicate that a parallel electric field is generated by the wave pulse, in which ambient electrons can – if at the appropriate “injection” energy – be accelerated to twice the Alfvén speed. Similar considerations for solar coronal conditions indicated that modest non-thermal energies of a few tens of keV could be achieved in this manner. McClements & Fletcher (2009) have also recently confirmed this for solar plasma in the test-particle limit. This process is found to damp the wave energy, though it remains to be seen by how much.

On arriving at the steep gradient in Alfvén speed represented by the chromosphere, it is to be expected that this wave pulse would be at least partially reflected (Emslie & Sturrock 1982). However, any component of the wave energy entering the chromosphere could be locally damped – for example by ion-neutral coupling – leading to chromospheric heating. If one considers the wave pulse as imparting stress to the chromospheric magnetic field, then the multiple current sheets that this might generate could provide an environment for particle acceleration, as suggested by Turkmani et al. (2005). The timescales are also such that a perpendicular MHD cascade could be established in the reflected wave field, providing another opportunity for stochastic acceleration of the chromospheric electrons, if the acceleration timescale is less than the collisional loss timescale as discussed in Section 3.4.

Significant theoretical work is yet required to demonstrate theoretically whether any of these options are viable, e.g., whether any chromospheric electron acceleration mechanism can reproduce the timing delays observed between high and low energy hard X-rays (e.g., Aschwanden et al. 1996), which are normally interpreted as strong evidence for a coronal

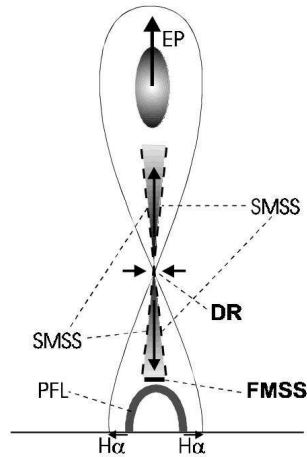


Fig. 4.2 Sketch of the flare scenario. EP: erupting prominence; DR: diffusion region; SMSS: slow-mode standing shock; FMSS: fast-mode standing (also called termination) shock; PFL: post flare loop. The grey shaded areas with the arrows show the outflow jets. From Mann et al. (2006).

electron accelerator. It should also be noted that in the proposed model of energy *transport*, magnetic reconnection still plays a central role as the mechanism of energy *release*, and as the driver of the Alfvén waves. This means that concurrent electron acceleration in the corona can also take place by “traditional” means (e.g., by electric fields in current sheets or by turbulent acceleration by various MHD wave modes).

4.3 Electron acceleration in collapsing current sheets

Figure 4.2 depicts a helmet-type magnetic structure often observed in solar flares (see, for example, Sui & Holman 2003), in which a prominence is destabilized due to photospheric footpoint motions and rises upwards as an *eruptive prominence*. As the prominence rises, the underlying field lines are stretched, leading to the formation of a current sheet. We suppose that when the current exceeds a critical value, the resistivity is suddenly enhanced (say by plasma waves excited by various instabilities) and rapid magnetic reconnection begins in the diffusion region (DR), as shown earlier in Figure 3.1.

MHD solutions for the large-scale magnetic configuration plotted in Figure 4.2 allow us to investigate (see Section 3.2) the reconnection process inside the diffusion region, characterized by plasma inflows with velocity V_0 in the x -direction (from the sides in Figure 4.2; from the top and bottom in Figure 3.1) and outflowing with velocities V_1 in the z -direction (to the top and bottom of Figure 4.2; to the left or right sides of Figure 3.1). The outflows are generally very fast and create a rather complicated structure in the outer region at the RCS edge. The plasma confined on the newly reconnected field lines will start moving with the velocity V_1 , both upwards (not shown in the cartoon), and downwards, where it will encounter a magnetic obstacle in the form of the underlying loop. If the distance to this obstacle is large, a collapsing magnetic trap (see the bottom plot in Figure 4.3) is formed. Moreover, the downward outflow is moving into a region of generally higher density and hence lower Alfvén speed. If a point is reached at which the outflow velocity V_1 exceeds

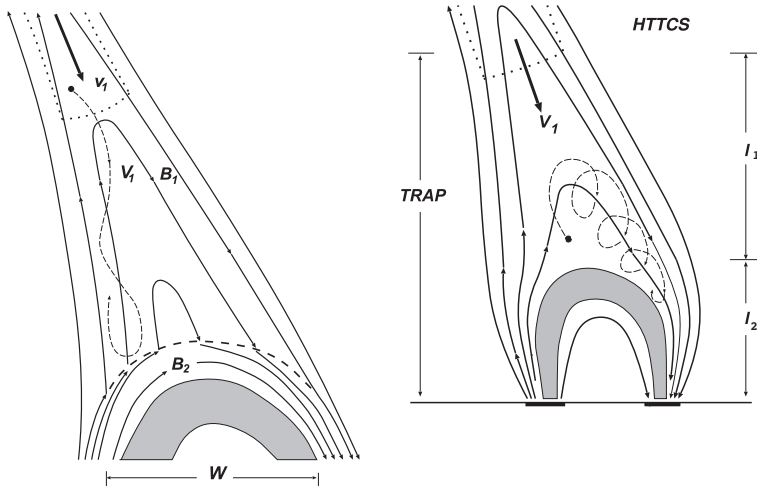


Fig. 4.3 Schematic models of collapsing magnetic field lines occurring in MHD models of magnetic reconnection with (left panel, dashed line) and without (right panel) a termination shock. From Somov & Kosugi (1997). HTTCS denotes “high temperature turbulent current sheet.”

the local magneto-acoustic wave velocity, then a fast MHD shock, termed a “termination shock,” can appear ahead of this magnetic obstacle (Somov & Kosugi 1997), as shown by the dashed line in the upper panel of Figure 4.3.

4.3.1 Acceleration in collapsing magnetic traps

Somov & Kosugi (1997), Karlický & Kosugi (2004) and Bogachev & Somov (2005, 2007) have carried out simulations of the acceleration of electrons in collapsing magnetic traps. Particles with an initial Maxwellian distribution are injected at random points of a fragmented current sheet geometry obtained using a three-dimensional MHD simulation.

As a result of its motion from the reconnection region towards the chromosphere, the length L of the magnetic trap decreases, leading to an increase in energy of the trapped particles via a first-order Fermi process associated with conservation of the longitudinal invariant $\int p_{\parallel} ds$ (Benz 2002). Also, as a result of the *transverse* contraction of the magnetic trap, particles are accelerated by the betatron mechanism. This transverse contraction can be described by the ratio $b(t) = B(t)/B_0$ which changes from 1, when $B(0) = B_0$ to $b_m = B_m/B_0$, where B_m is the magnetic field in the magnetic mirrors. Thus the particle momenta p_{\parallel} and p_{\perp} change as follows:

$$p_{\parallel} = p_{0\parallel} \ell^{-1}, \quad (4.1)$$

where $\ell = (L/L_0)$, and

$$p_{\perp} = p_{0\perp} b^{1/2}. \quad (4.2)$$

Both the Fermi and betatron accelerations are accompanied by a change in particle pitch angle – a decrease (Fermi) or increase (betatron). When these two mechanisms act simulta-

neously, then the pitch angles of accelerated particle vary according to

$$\tan \alpha = \frac{p_{\perp}}{p_{\parallel}} = \ell b^{1/2} \tan \alpha_0, \quad (4.3)$$

which can result in an increase or decrease of pitch angle, according to the relative importance of the two effects. The particle kinetic energy increases in the magnetic trap until it falls into the loss cone.

Simulations show that particles with an initially Maxwellian distribution gain energies via both acceleration mechanisms; they retain a quasi-thermal distribution but attain much higher energies. The change of total kinetic energy has a form of the burst of particles with energies up to a few MeV. However, the magnetic energy is absorbed very rapidly by the electrons, so that a test-particle approach very rapidly ceases to be valid. A fuller treatment of this scenario therefore requires full kinetic simulations similar to those discussed in Section 4.8.

4.3.2 Acceleration by a termination shock

Due to the strong curvature of the magnetic field lines in the vicinity of the diffusion region in a helmet-type reconnection (see Figure 4.2), the slowly inflowing plasma shoots away from the reconnection site as a hot jet. These oppositely-directed jets are embedded between a pair of slow magnetosonic shocks. If the speed of this jet is super-Alfvénic, a fast magnetosonic shock, also called a *termination shock*, is established, as shown previously in Figure 4.3. The appearance of such shocks was predicted in the numerical simulations of Forbes (1986), Shibata et al. (1995) and Somov & Kosugi (1997).

Radio measurements (Aurass et al. 2002; White et al. 2011) of SOL2003-10-28T11:10 (X17.2) reveal the termination shock as a standing radio source with a (large) half-power source area of $A_s = 2.9 \times 10^{20} \text{ cm}^2$. A strong enhancement of the electromagnetic emission in the hard X- and gamma-ray range up to 10 MeV is simultaneously observed with the appearance of the radio signatures of the shock (Aurass & Mann 2004). These observations indicate that the termination shock could well be the source of the highly energetic electrons needed for the generation of the hard X- and gamma-ray radiation.

A fast magnetosonic shock formed during the MHD simulations of a reconnection process is accompanied by a compression of both the magnetic field and the density. Thus, it represents a moving magnetic mirror at which charged particles can be reflected and accelerated through a process termed *shock-drift acceleration*. This process can accelerate highly energetic electrons up to 10 MeV (Mann et al. 2006).

Generally, shock-drift acceleration represents reflections at the termination shocks. Analysis of such an acceleration is most straightforwardly performed in the *de Hoffmann-Teller frame*, the frame in which the electric field vanishes, so that the reflection takes place under conservation of both kinetic energy and magnetic moment. From such an analysis (Mann et al. 2006, 2009), one obtains the relationships between the electron velocities $\beta = v/c$ parallel and perpendicular to the upstream magnetic field before (index i) and after (index r) the reflection:

$$\beta_{r,\parallel} = \frac{2\beta_s - \beta_{i,\parallel}(1 + \beta_s^2)}{1 - 2\beta_{i,\parallel}\beta_s + \beta_s^2} \quad (4.4)$$

and

$$\beta_{r,\perp} = \frac{(1 - \beta_s^2)}{1 - 2\beta_{i,\parallel}\beta_s + \beta_s^2} \cdot \beta_{i,\perp}, \quad (4.5)$$

where $\beta_s = v_s \sec \theta / c$. Here v_s is the shock speed, c the velocity of light, and θ the angle between the shock normal and the upstream magnetic field. In addition, the reflection conditions:

$$\beta_{i,\parallel} \leq \beta_s \quad (4.6)$$

and

$$\beta_{i,\perp} \geq \frac{\tan \alpha_{lc}}{\sqrt{1 - \beta_s^2}} \cdot (\beta_s - \beta_{i,\parallel}) \quad (4.7)$$

must be satisfied in order for acceleration to occur. The loss-cone angle is defined by $\alpha_{lc} = \sin^{-1}[(B_{\text{up}}/B_{\text{down}})^{1/2}]$, where B_{up} and B_{down} denote the magnitude of the magnetic field in the up- and downstream region, respectively.

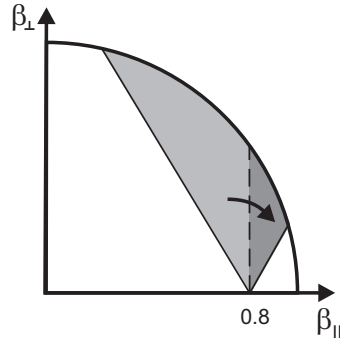


Fig. 4.4 Illustration of shock-drift acceleration in the $\beta_{\perp} - \beta_{\parallel}$ plane for a shock with $\beta_s = 0.8$ and $\alpha_{lc} = 45^\circ$. All particles initially located in the light grey area are transformed into the dark one.

Shock-drift acceleration represents a transformation in the $\beta_{\perp} - \beta_{\parallel}$ plane as illustrated in Figure 4.4. As seen in Figure 4.4, the accelerated distribution function is simply a *shifted loss-cone distribution*. The flux of the accelerated electrons parallel to the upstream magnetic field is defined by

$$F_{acc,\parallel} = 2\pi N_0 c^4 \int_0^1 d\beta_{\parallel} \beta_{\parallel} \int_0^1 y d\beta_{\perp} \beta_{\perp} \cdot f_{acc}(\beta_{\parallel}, \beta_{\perp}), \quad (4.8)$$

and the differential flux is given by

$$j_{acc,\parallel} = \frac{dF_{acc,\parallel}}{dE}. \quad (4.9)$$

Figure 4.5 shows the differential fluxes obtained from the shock-drift acceleration model for various angles θ , assuming an initial distribution in the form of a Maxwellian with a temperature $T = 10$ MK. For comparison, the dotted line in Figure 4.5 represents a pure Maxwellian distribution with the same temperature. One can see that shock-drift acceleration indeed provides a significantly enhanced component of energetic electrons, particularly for large values of the angle θ . These analytically-obtained results are qualitatively confirmed by numerical simulations performed for plasma conditions usually found at the Earth's bow shock (Krauss-Varban & Wu 1989; Krauss-Varban et al. 1989; Krauss-Varban & Burgess 1991).

In order to compare these results with observations, some basic parameters must be provided. Here, SOL2003-10-28T11:10 (X17.2) is considered as an example (Mann et al.

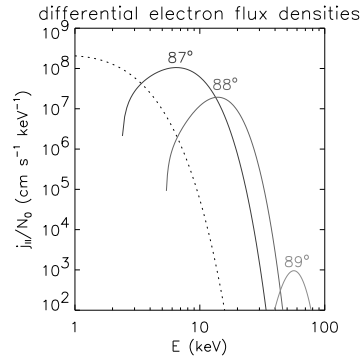


Fig. 4.5 Differential flux of electrons accelerated by shock-drift acceleration for various shock angles. The dotted line represents the flux of a pure Maxwellian distribution.

2009). In this event, the termination shock appears at 300 MHz for the harmonic emission. Matching harmonic emission to the observed 300 MHz frequency requires an electron number density of $2.8 \times 10^8 \text{ cm}^{-3}$. According to a two-fold density model of the corona (Newkirk 1961), such a region is located $\sim 160 \text{ Mm}$ above the photosphere, at which a magnetic field of $\sim 5 \text{ G}$ is expected (Dulk & McLean 1978). These parameters lead to an Alfvén speed $V_A \approx 560 \text{ km s}^{-1}$. For the temperature, a value of 40 MK is adopted, resulting in a thermal electron speed of $2.5 \times 10^4 \text{ km s}^{-1}$.

Assuming a density jump of a factor of two across the termination shock, the Rankine-Hugoniot relations give a magnetic field $B_{\text{down}}/B_{\text{up}} = 2$ and an Alfvén-Mach number $M_A = 3.5$, corresponding to a shock speed of $\sim 2000 \text{ km s}^{-1}$. Due to the curvature of the magnetic field lines convected through the termination shock, there is a distribution of θ across the shock. Recognizing from Figure 4.5 that the flux is very sensitive to θ , we model this curvature by a circle; the resulting flux of accelerated electrons can be integrated over θ , giving an accelerated electron production rate $F_e = 2 \times 10^{36} \text{ s}^{-1}$ and a related power $P_e = 1 \times 10^{29} \text{ erg s}^{-1}$ above 20 keV. This agrees well with the results inferred from *RHESSI* observations (Warmuth et al. 2007, 2009).

It must be stressed that a non-negligible part of the energy of the outflow jet is transferred into accelerated electrons. Thus, such a test-particle approach has its limitations: the termination shock acceleration process must be treated in a fully kinetic manner, in which the accelerated particles themselves are included in the conservation laws across the shock.

4.4 Particle acceleration in a single 3-D RCS with complicated magnetic topology

4.4.1 Basic equations

Following Section 3.3, we consider a highly-stressed current sheet oriented in the x -direction, with a lateral field

$$B_z(x) = B_0 \tanh\left(-\frac{x}{d}\right) \quad (4.10)$$

and a transverse magnetic field component B_x that is dependent on z according to (Zharkova & Gordovskyy 2005a,b):

$$B_x(z) = B_0 \left(\frac{z}{a}\right)^\alpha, \quad (4.11)$$

where $\alpha > 0$ (we consider an illustrative value $\alpha = 1$). A weak, constant longitudinal component of the magnetic field B_y is also assumed to be present:

$$B_y = \beta B_0. \quad (4.12)$$

Particle trajectories are calculated from the relativistic equations of motion

$$\frac{d\mathbf{r}}{dt} = \frac{\mathbf{p}}{m_0\gamma} \quad (4.13)$$

$$\frac{d\mathbf{p}}{dt} = q \left(\mathbf{E} + \frac{1}{c} \frac{\mathbf{p}}{m_0\gamma} \times \mathbf{B} \right), \quad (4.14)$$

where t is time, \mathbf{r} and \mathbf{p} are the particle position and momentum vectors, \mathbf{E} and \mathbf{B} are the electric and magnetic field vectors, q and m_0 are the charge and rest mass of the particle, c is the speed of light, and $\gamma = \sqrt{(p/m_0c)^2 + 1}$ is the Lorentz factor. The integration time steps are chosen to be much smaller than the corresponding gyro-period, i.e., $dt \leq 0.1 (m/q) B_z^{-1}$. For protons, this typically requires a time step $\lesssim 10^{-7}$ s, while for electrons the required time step is substantially shorter, $\lesssim 4 \times 10^{-11}$ s.

It should be noted that in the above description, the electric and magnetic field vectors \mathbf{E} and \mathbf{B} are *prescribed* quantities; the self-consistent electric and magnetic fields produced by the accelerated particles themselves are neglected. Such a test particle approach is valid for up to only $\sim 10^5$ test particles (Birdsall & Langdon 1985), and we shall return to this point in Section 4.7. It should also again be noted (see Section 3.3) that in this simulation the reconnection electric field is assumed to extend over the entire region covering the whole diffusion region. Thus, the caveats noted in this earlier Section also apply here.

4.4.2 Particle motion inside a 3-D RCS

In the test-particle description used here, the electron trajectory and the direction of ejection are determined uniquely by its initial coordinate, velocity and the magnetic field geometry. Particles inflowing into a 3-D RCS are accelerated mostly near the lateral field reversal at the x -axis. In the presence of a non-zero B_y , electrons and protons are ejected in opposite directions from the midplane ($x = 0$); whether the particle is ejected to $x > 0$ or $x < 0$ depends on the sign of the particle charge, and the signs and magnitudes of B_x and B_y . If B_y is strong enough, then all protons (regardless of the side of the RCS they entered from) are ejected to the $x > 0$ semispace, while all electrons are ejected to the opposite semispace, as illustrated in Figure 4.6 (Zharkova & Agapitov 2009). For particles of the same charge, there are two fundamental types of trajectories inside an RCS: particles that enter from and then are ejected into the *same* semispace are hereafter referred to as “bounced” particles, whereas particles that are ejected into the *opposite* semispace are referred to as “transit” particles.

Electron/proton asymmetry in the particle trajectories is dependent on the magnitude of the guiding field (Zharkova & Gordovskyy 2004). The asymmetry is *full* (equal to unity) if B_y is strong enough ($B_y/B_z \gtrsim 1.5 \times 10^{-2}$) that electrons are ejected into one semiplane and protons to the opposite one. If the guiding field is weak ($B_y/B_z \lesssim 10^{-6}$), electrons and protons can be ejected into the *same* semiplane (Zharkova & Gordovskyy 2004, 2005b). For a guiding field of intermediate magnitude, electrons and protons are ejected in a partially neutralized manner, with protons dominating in one semiplane and electrons in the other (Zharkova & Gordovskyy 2005b). The result of this separation of particle species is a polarization electric field appearing between the protons at the edge and electrons at the

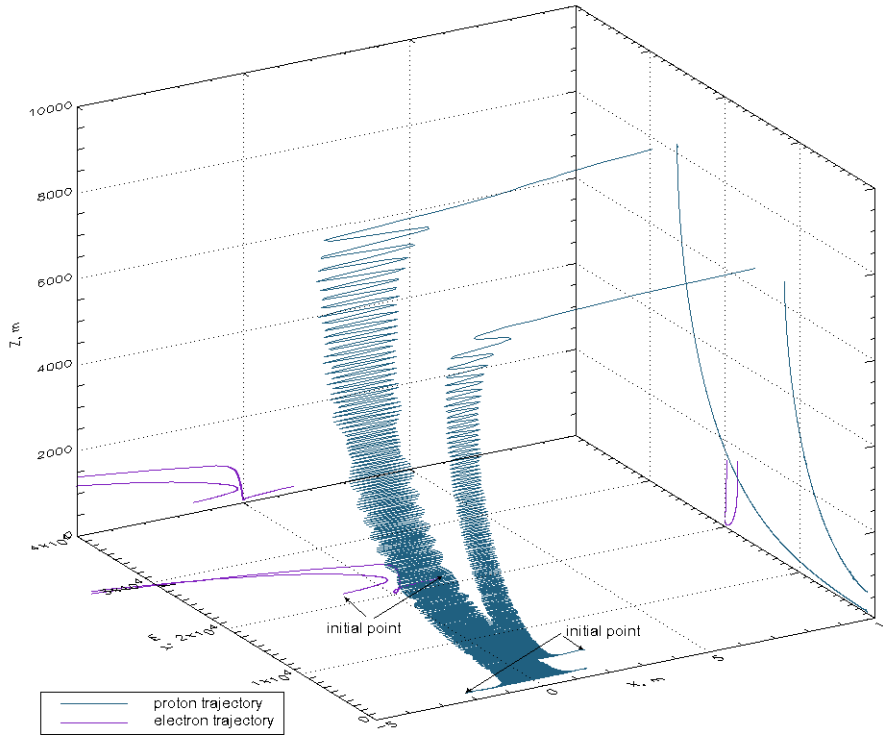


Fig. 4.6 Proton (blue lines) and electron trajectories (purple lines) in a 3-D RCS with a lateral magnetic field $B_x = 10$ G and an drift electric field $E_y = 100$ V m $^{-1}$. From Zharkova & Agapitov (2009).

midplane of the RCS. Such a field was anticipated by Litvinenko & Somov (1993a) and Oreshina & Somov (2000b), and has been investigated in some detail by Zharkova & Agapitov (2009).

The model produces power-law energy distributions with spectral indices $\delta = 1.5$ for protons and $\delta = 2$ for electrons. Such a result is confirmed by both analytic (Litvinenko 1996a) and numerical approaches (Zharkova & Gordovskyy 2005b; Wood & Neukirch 2005). For comparison, the particle energy spectra calculated for the model RCS of Oreshina & Somov (2000b) and presented in Figure 4.7 show features beyond such simple power-law forms: there is a rapid rise in flux to a maximum at $E = E_m$; above this, the spectrum is approximately power-law. $E_m \simeq 10 - 12$ keV for protons ($\simeq 2 - 5$ keV for electrons); these values increase slightly with the value of the parameter $\beta = B_y/B_z$. The energy E_m can be considered as the lower energy cutoff to the electron spectrum (see Section 2.1), and the values obtained here agree quite well with the values deduced from *RHESSI* observations (Holman et al. 2011).

The spectral index δ for the power-law part of the spectrum ($E > E_m$) is found to vary slightly with the magnitude of the guiding field B_y . For a weak guiding field ($\beta = 10^{-4}$ – Figures 4.7, [a] and [d]), the particle trajectories are nearly symmetrical (Zharkova & Gordovskyy 2005b); the particles are ejected equally into both hemispheres as approximately neutral beams. The particle energy spectra in both hemispheres ($x < 0$ and $x > 0$) are very similar, with a sharp increase from zero to E_m , followed by a power-law with spectral indices

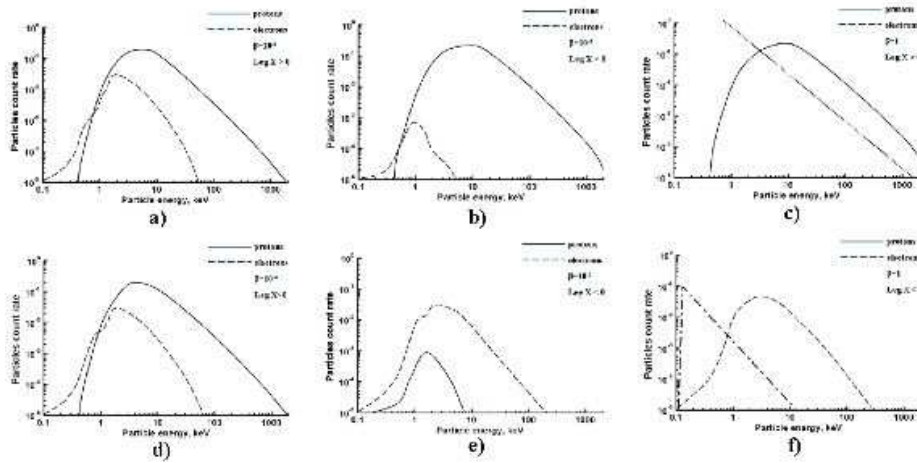


Fig. 4.7 Energy spectra of electrons (dashed lines) and protons (solid lines) ejected from the RCS. Spectra (a) - (c) are calculated for $\beta (= B_y/B_0)$ equal to 10^{-4} , 10^{-2} and 1, respectively, and correspond to the semispace $x > 0$. Spectra (d) - (f) are calculated for the same values of β , but for the semispace $x < 0$. The estimated proton spectrum is presented as a dotted line in plot (c) and the estimated electron spectrum is shown as a dash-dotted line in plot (f). From Zharkova & Gordovskyy (2005b).

$\delta \simeq 1.8$ for protons and $\delta \simeq 2.2$ for electrons. The power-law shapes extend up to about 100 keV (electrons) or 1 MeV (protons).

For a moderate guide field ($\beta = 10^{-2}$ – Figures 4.7 [b] and [e]), the protons and electrons are also ejected into both semispaces; however, the symmetry of their trajectories is partially destroyed. Hence, most protons are ejected into the semispace $x < 0$ with $\delta \simeq 1.7$, while a few low-energy protons are ejected into the semispace $x > 0$ with very soft, thermal-like, spectra ($\delta \simeq 4.8$). The opposite picture holds for electrons: the bulk are ejected into the semispace $x < 0$ with an energy spectrum $\delta \simeq 2.0$, while a smaller number of the low-energy electrons are ejected into the semispace $x > 0$ with a thermal-like spectrum having a maximum $E_m \approx 1$ keV.

Finally, if the guiding field is very strong ($\beta \simeq 1$ – Figures 4.7, [c] and [f]), the particle trajectories are completely asymmetric. Particles are ejected completely separately from the RCS midplane into opposite semispaces: all protons are ejected into the semispace $x > 0$ while all electrons are ejected into the semispace $x < 0$. Their energy distributions show a sharp increase of particle number up to around a few keV followed by a power-law energy spectrum of index $\delta \simeq 1.5$ for protons and $\delta \simeq 1.8$ for electrons. (These spectral indices vary with the magnitude of a guiding field (Fig. 4.8) reflecting different reconnection scenarios and with different phases of magnetic reconnection, as discussed in Section 4.5.)

As shown in Figure 4.9, during the reconnection process, the shape of the reconnecting current sheet changes from a non-compressed one with a symmetric X-type null point to a strongly-compressed shape with a well-defined elongation along the z -direction and a compression in the x -direction. The extent of this deformation depends on the value of the parameter α (Priest & Forbes 2000; Somov 2000) and possibly corresponds to different reconnection rates (Arber & Haynes 2006). At the reconnection onset ($\alpha = 0$) the diffusion region is located very near the null point. As the reconnection progresses (α increases from 0 to 1), the diffusion region becomes much wider in both x and z -directions. As α increases further, the reconnection rate begins to decrease (Zharkova & Agapitov 2009).

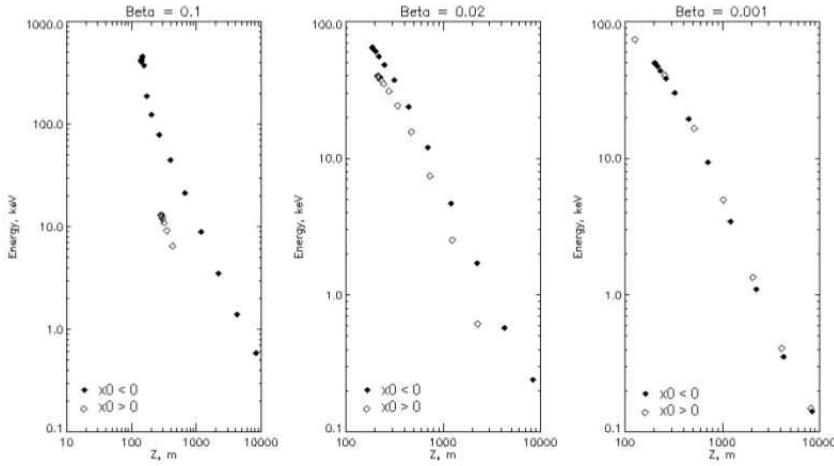


Fig. 4.8 The energy spectra resulting from the protons entering the current sheet from opposite sides, for different ratios $\beta = B_y/B_0$ and different magnitudes of the parameter α . From Zharkova & Agapitov (2009).

The spectral index of the accelerated particle energy spectra is associated with the parameter α and depends on the magnitude of the guiding field (Fig. 4.8). For an RCS with a density that increases exponentially with distance z and for a variation of density $n(z) \propto (z/a)^\lambda$, the following results are obtained (Zharkova & Agapitov 2009): for electrons in a weak (strong) guiding field B_y ,

$$\delta_{e,\text{weak}} = 1 + \frac{2 + \lambda}{2\alpha}; \quad \delta_{e,\text{strong}} = \frac{1}{2} + \frac{1 + \lambda}{2\alpha}, \quad (4.15)$$

while for protons in a guiding field of *any* strength,

$$\delta_p = 1 + \frac{1 + \lambda}{2\alpha}. \quad (4.16)$$

In principle, therefore, by simultaneously measuring the spectral indices of electrons and protons in the same flare, one can deduce the magnetic field geometry under which these particles were accelerated (Zharkova & Gordovskyy 2005b; Zharkova & Agapitov 2009).

We again stress that all of these results have been arrived at using a test-particle approach, in which the feedback of the electromagnetic fields associated with the accelerated particles is not taken into account. Such a limitation is addressed in the PIC approach discussed in Section 4.8.

4.5 Particle acceleration in 3-D MHD models with fan and spine reconnection

A further development in modeling particle acceleration in a reconnecting current sheet involves more advanced MHD models of fan and spine reconnection (Priest & Titov 1996).

The axis of symmetry of the magnetic field, called the *spine* and designated here as the x axis, is a critical field line connecting to the null point. In the plane $x = 0$, the magnetic field lines are straight lines through the null point describing a fan; hence, the (y, z) -plane is termed the *fan plane*. The spine and the fan are the 3-D analogs of the separatrix planes in

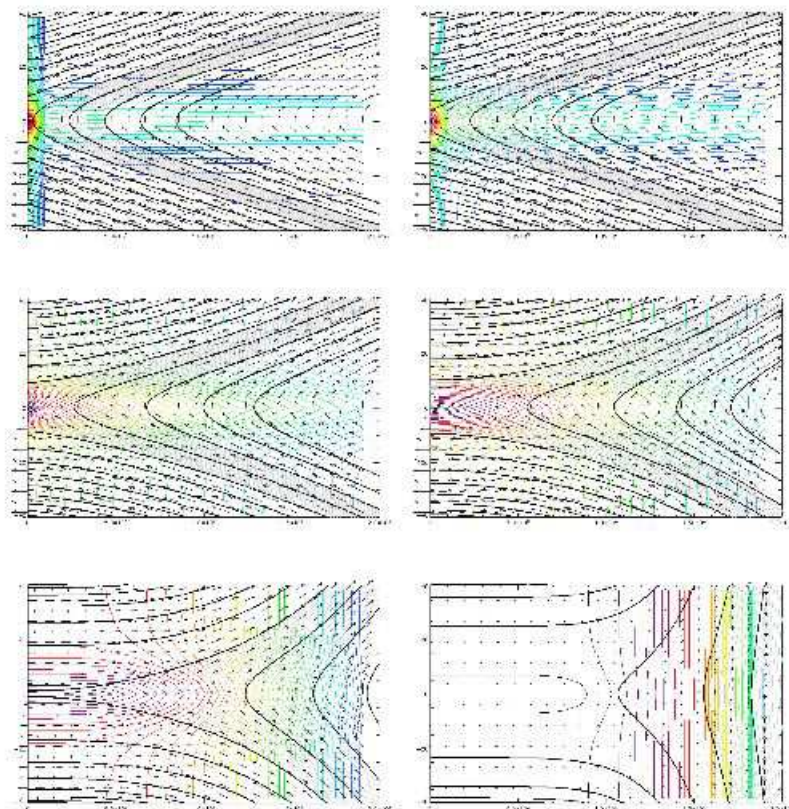


Fig. 4.9 Views of the current sheet for different values of $\alpha = 0.5; 0.7; 1.0; 1.5; 2.0$ and 5.0 (plotted by rows from the top left to the right bottom plot). From Zharkova & Agapitov (2009).

the classic 2-D X-point geometry. The field configuration near the potential magnetic nulls is given by Equations 4.10 – 4.12.

Two regimes of reconnection at a 3-D magnetic null are possible: *spine reconnection* and *fan reconnection* (Lau & Finn 1990; Priest & Titov 1996). While the magnetic field configuration is the same in the two regimes, they are characterized by different plasma flow patterns and different electric fields. Spine reconnection has a current concentration along the critical spine field line, while fan reconnection has a current sheet in the fan plane.

For a potential null, the spine reconnection regime is characterized by plasma flows lying in planes containing the spine, while fan reconnection has non-planar flows that carry the magnetic field lines in a “swirling”-like motion symmetric about the fan plane. It should be noted that the electric field and flow pattern are non-axisymmetric in all cases. The model of Priest & Titov (1996) provides a useful analytical model for initial studies; it allows some of the key features of topology and geometry to be identified, and it is the closest 3-D analog of the widely-studied constant out-of-plane electric field used in 2-D studies. It describes only the outer ideal reconnection region and does not include acceleration due to the parallel

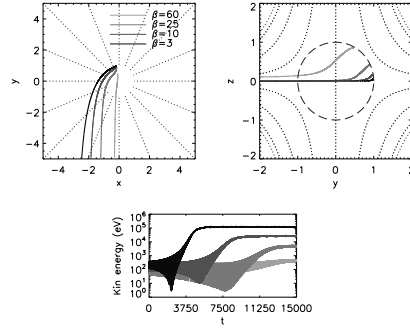


Fig. 4.10 Trajectories and energy gains in fan reconnection, for particles injected on the boundary at different latitudes β . From Dalla & Browning (2008).

electric field in the inner dissipation or resistive region; indeed, it breaks down very close to the spine/fan, as the electric fields formally diverge. However, since few particles will enter the small-volume dissipation regions, the results are likely to be appropriate for the bulk of the energy spectrum. This model has been used as a basis for particle acceleration at 3-D nulls in the regimes of both spine reconnection (Dalla & Browning 2005, 2006) and fan reconnection (Dalla & Browning 2008). Particle trajectories are obtained numerically by solving the relativistic equations of motion (Equation 4.14). Again, a test-particle approach is used (for limitations, see Section 4.7).

The strength of the driving electric field is quantified by the parameter

$$\tilde{\mu} = \frac{v_{\perp}^2}{v_E^2(L)}, \quad (4.17)$$

where v_{\perp} is the perpendicular speed associated with the gyro-motion, which may be equated to the thermal speed of the plasma. This can also be expressed as the dimensionless magnetic moment when speeds are normalized to the drift speed (Vekstein & Browning 1997):

$$\tilde{\mu} = \frac{mv_{\perp}^2/2B_0}{mv_E^2(L)/2B_0}, \quad (4.18)$$

where B_0 is the amplitude of the magnetic field. If $\tilde{\mu} \ll 1$, the electric drift speed at global length scales is strong compared with the thermal gyro-motion and we are in the *strong drift regime* corresponding to fast reconnection; in practice, this regime is reached when $\tilde{\mu} \approx 1$. In this case, particles may undergo significant acceleration (Dalla & Browning 2005) even in the outer “ideal” reconnection region, similar to those discussed in Section 4.4.

Typical individual trajectories in the fan reconnection are shown in Figure 4.10, while similar plots for spine reconnection can be found in Dalla & Browning (2005). Note the strong dependence of the energy gain on the injection location, similar to those found for a single RCS in Section 4.4: particles injected closer to the fan plane (at lower latitudes β) are accelerated the most as they approach the strong-electric-field region near the fan plane.

Energy spectra for the spine and fan reconnection (Figures 4.11 and 4.12, respectively) show that a significant fraction of protons can be accelerated to energies of up to 10 MeV, comparable to the values obtained in the simple 3-D topology presented in Section 4.4. As appears to be natural during any reconnection process, a generally power-law spectrum is obtained for the accelerated particles, but with a significant “bump” at higher energies,

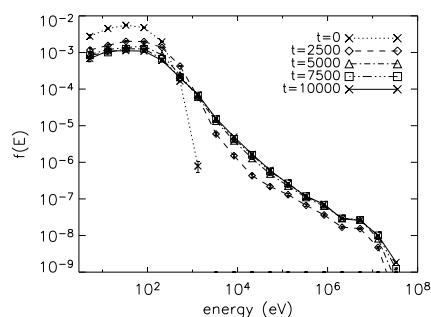


Fig. 4.11 Energy spectra of particles in spine reconnection at successive times, showing evolution towards steady state. From Dalla & Browning (2006).

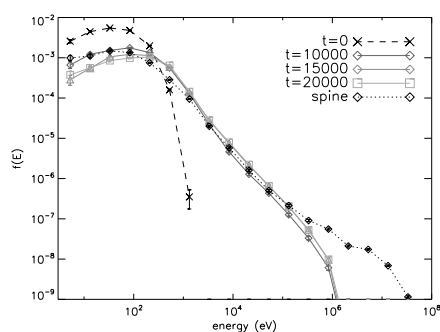


Fig. 4.12 Energy spectra of particles in fan reconnection at successive times, showing evolution towards steady state. From Dalla & Browning (2008).

particularly for the spine reconnection, for which the bump arises from particles approaching close to the null itself.

This “bump-on-tail” distribution is similar to those reported for a single 3-D current sheet in Figure 4.8 in Section 4.4 (see also Zharkova & Gordovskiy 2005c; Zharkova & Agapitov 2009) and is formed by the two populations of protons: “transit” and “bounced” ones, respectively. Note that the slopes of the spectra are similar for the spine and fan reconnection in the intermediate energy range, although fan reconnection is significantly less effective at generating high-energy particles.

Detailed information on both the spatial distributions of the accelerated particles, and where these particles originate, are shown in Figures 4.13 and 4.14, for spine and fan reconnection, respectively. These show the angular location of the particles at the initial (top plot) and the final (bottom plot) times. Each location is identified by its latitude β , i.e., the elevation angle from the x - y plane, and longitude ϕ . Inflow regions are the top-right and bottom-left quadrants in the (ϕ, β) representation, but for clarity, only particles originating in the latter are shown (the other quadrant can be added by symmetry). Each point represents one particle and is color-coded according to the final particle energy.

In the case of spine reconnection, particles injected in the plane in which the electric field is weakest (longitude $\phi = 0$) actually have the greatest energy gain, although their acceleration times are longest (Dalla & Browning 2005). The high-energy particles which

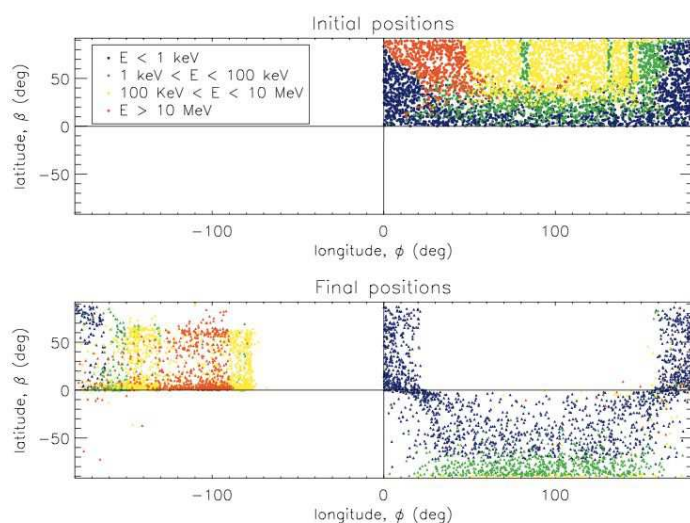


Fig. 4.13 Positions of particles at initial and final times for *spine* reconnection, color-coded according to their final energies (from Dalla & Browning 2006).

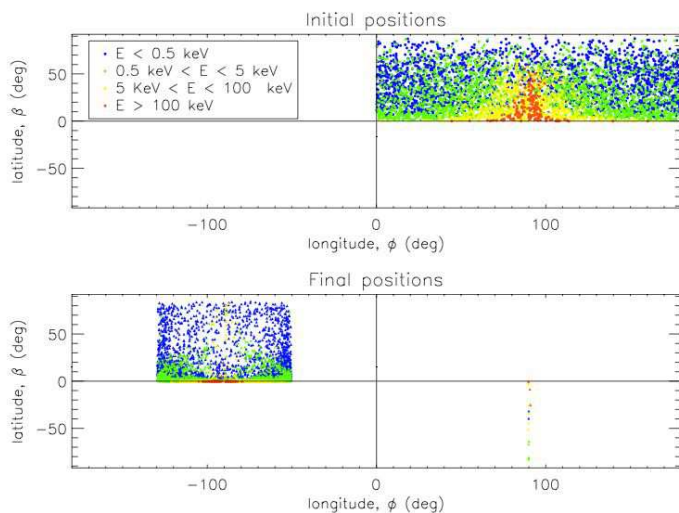


Fig. 4.14 Positions of particles at initial and final times for *fan* reconnection, color-coded according to their final energies. From Dalla & Browning (2008).

escape mostly emerge in jets along the spine. However, most of the highest-energy particles actually remain trapped in the magnetic field (Dalla & Browning 2006). The occurrence of these high-energy trapped particles may be an explanation for coronal hard X-ray sources (Krucker et al. 2008a).

In fan reconnection, particles starting near the fan plane are those that gain the largest energy, as would be expected since the fan plane is the location where the electric field is largest. As one moves towards increasing latitudes, particles will reach the fan plane

with greater difficulty and so gain less energy. Figure 4.14 shows that, at the final time, particles are confined to a range of longitudes $[-130^\circ, -50^\circ]$. This is a result of the tendency of the electric field drift in fan reconnection to push particles towards the $x = 0$ plane after they have passed the region near the null. Figure 4.14 also shows that the initial azimuthal locations near $\phi = 90^\circ$ are the most favorable for particle acceleration since, near this plane, the transverse component of the electric field drift, pushing particles towards the fan plane, is largest. The fan reconnection regime is less efficient in seeding test particles to the region of strong electric field, compared with spine reconnection, and acceleration times are longer.

These results, obtained for a single-current-sheet reconnection model with a more complicated magnetic and electric field topology simulated by Priest & Titov (1996), advance further the conclusions derived from the basic 3-D reconnection models discussed in Section 4.4. This approach confirms that acceleration by a super-Dreicer electric field generated during magnetic reconnection is a viable mechanism, which naturally explains the energy input from magnetic field dissipation and its output in the form of power-law energy spectra of accelerated particles, with spectral indices related to the magnetic field geometry occurring during the reconnection. Apparently, this approach offers a good diagnostic tool for the magnetic field topology from the observed signatures of accelerated particles. We yet again note that the limitations of the test-particle approach (see Section 4.7) can restrict this diagnostic capability, and that a full kinetic approach to particle acceleration in such geometries is required.

4.6 Particle acceleration in multiple current sheets formed by MHD turbulence

Although particle acceleration in a single current sheet can, in principle, account for some flares or even flare ribbons, it is highly likely that flares are due to a number of unresolved magnetic tubes interacting with each other, so that more complex coronal geometries with multiple acceleration sites must be considered. One obvious benefit of such a scenario is that a particle can be accelerated at more than one location, perhaps enhancing the energization process.

4.6.1 Acceleration in Cellular Automata Models

The idea of multiple dissipation sites in flares is longstanding, but the first serious effort at modeling this was by Lu & Hamilton (1991), who took the ideas associated with self-organized criticality (SOC) and applied them to the solar corona. They showed that if the right conditions were met, the triggering of dissipation at a single point could lead to a “spreading” of dissipation across a large coronal volume and that the distribution of event size as a function of energy followed a power law ($\mathcal{N}(\mathcal{E}) \propto \mathcal{E}^{-1.8}$) similar to that observed in flares (e.g., Crosby et al. 1993). However, a fundamental question remains: can existing MHD models verify that the main rationale behind the SOC theory is valid?

Self-organized criticality models identify dissipation occurring at many spatially-separated regions as illustrated in Figure 4.15, taken from Vlahos et al. (2004). The upper left panel shows a coronal field geometry, reconstructed from photospheric magnetograms, in a volume with characteristic dimensions of 10^9 cm. The current density in a localized region is shown in the upper right panel, and a snapshot of the locations where currents exceed the threshold for dissipation in the cellular automaton model (referred to as Unstable Current Sheets) is shown in the bottom right panel. Energy release in this model occurs at a number of locations of unstable current sheets (bottom left panel).

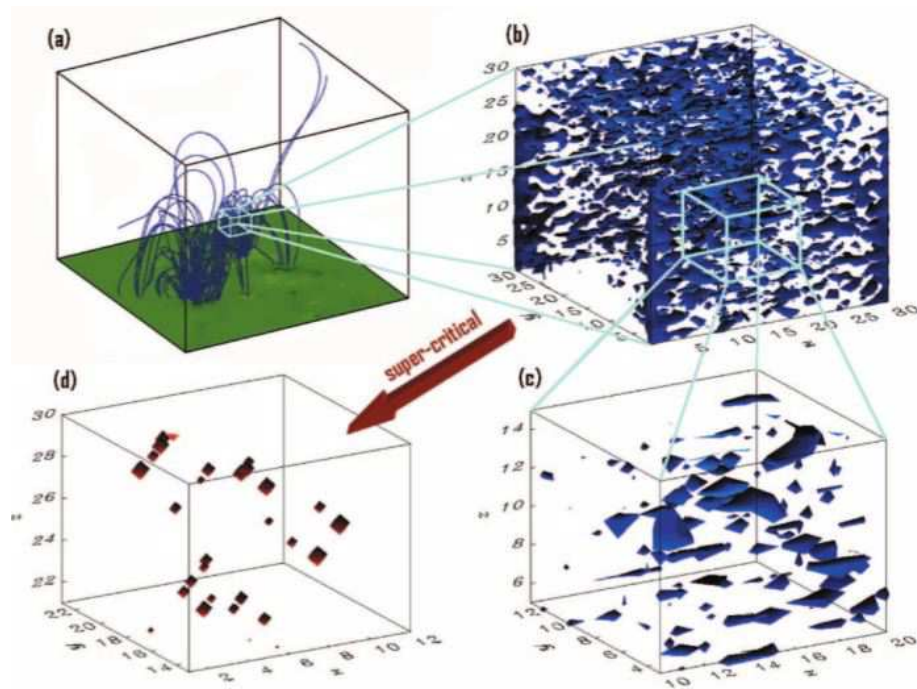


Fig. 4.15 The model of multiple current sheet formed by MHD turbulence in the CA model. From Vlahos et al. (2004).

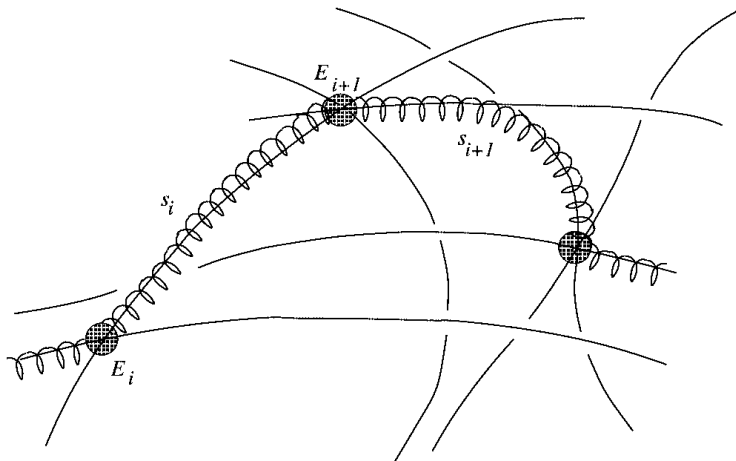


Fig. 4.16 Particle trajectories in the CA model. From Vlahos et al. (2004).

To assess particle acceleration in such a coronal geometry, Vlahos et al. (2004) have developed a model in which the particles move from one unstable current sheet to another unstable current sheet, gaining (or losing) energy at each and undergoing ballistic motion in a background magnetic field in between. This is illustrated in Figure 4.16, where a particle first interacts with a site i , escapes along the magnetic field, encounters a site $i + 1$, escapes again, and so on. The energy gain thus occurs in many small increments, rather than at the single location of the current-sheet approach. By using the self-organized criticality hypothesis, one can identify the structure of the spatial distribution of the unstable current sheets inside a complex active region which exhibits a specific fractal structure (McIntosh et al. 2002). Knowledge of the spatial structure of the unstable current sheets can help us to reconstruct the probability distribution of its spatial scales, and thus, the probability of a particle colliding with a given element of it (Islaker & Vlahos 2003). We do not yet understand the statistical properties of the “kernel” – the energy gain or loss for a particle colliding with an unstable current sheet – but this is relatively easy to study using three-dimensional MHD codes.

We can therefore start from a global reconstruction of the distribution of unstable current sheets and recover the kinetic properties of the particles, under the assumptions of the self-organized criticality theory. The acceleration is thus determined by three probability densities: one, defining the distance between a pair of accelerators; the second, the electric field strength at each accelerator; and a third, either the time spent in, or the length of, the unstable current sheet. The first two are assumed to be power laws, and the third is taken to be a Gaussian. Note that this model only addresses acceleration by direct electric fields, since that can be simply parameterized at the dissipation sites.

In the example shown in Figure 4.15, the particle moves in a box of size 10^{10} cm and the distance between accelerators ranges from 10^4 to 10^{10} cm. The magnetic fields may be such that the particles become partially trapped and the trajectory becomes rather complex. The upper limit of the free travel distance is set to a value larger than the coronal volume in order to allow particles to leave the coronal region without undergoing any interaction with electric fields, besides the initial one. Note that for the maximum time $\Delta t = 1$ second for which the system is monitored, these escaping particles will move at most a distance $c\Delta t = 3 \times 10^{10}$ cm, which is of the order of the length of the coronal volume considered.

The electric field at each unstable current sheet varies between sub-Dreicer and 10^8 times Dreicer, and the acceleration time has a mean value of 2×10^{-3} s (Vlahos et al. 2004). A large number of test particles are tracked through this coronal geometry using the relativistic equation of motion described by Equations 4.14, with acceleration taking place very rapidly ($\ll 1$ s).

Figure 4.17 shows the distribution function of electrons at four different times. The initial distribution is a Maxwellian with a temperature of 100 eV (dash-dot line). One can see that (a) prompt acceleration to energies well in excess of 100 keV takes place, (b) just under half of the particles end up in the high energy tail and (c) the tail is a power law with slope $\delta \simeq 4$. When the test particles are protons, much longer acceleration times must be considered to allow for similar energies to be reached within the prescribed acceleration time.

Another approach based on the SOC models was proposed by Anastasiadis et al. (2004) to predict the kinetic energy distributions of electrons. The acceleration of electrons is still due to the presence of the randomly placed localized electric fields produced by the energy release process and simulated by the CA model. It is assumed that electrons interact successively with reconnecting current sheets with the electric field linked to the energy release time series. At each encounter, they randomly gain or lose energy. Electrons can be acceler-

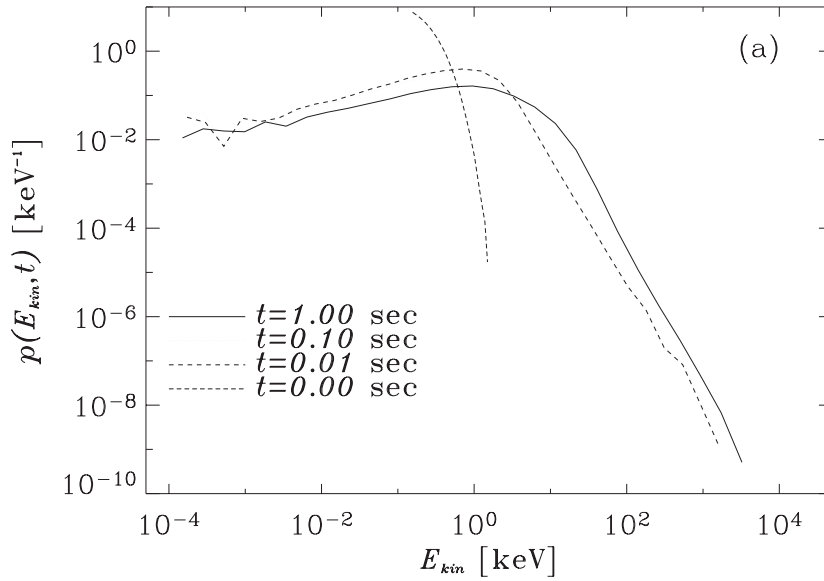


Fig. 4.17 Accelerated electron spectra in the CA model (Vlahos et al. 2004).

ated from a Maxwellian initial distribution up to a few MeV, and can be represented either by a power-law or an exponential distribution.

As the number of interactions increases, the electron energy distribution begins to diverge from a well defined power law, and an exponential tail develops (e.g., Trotter et al. 1998; Vilmer et al. 2003). Thick-target radiation from these energetic electrons was also computed, leading to hard X-ray spectra at low energies (10-100 keV) which are much flatter than usually observed. At higher energies (100-1000 keV), the X-ray spectra were consistent with the observations at these energies.

4.6.2 Acceleration in three-dimensional MHD turbulence

Numerical experiments for test-particle acceleration in the turbulent magnetic and electric fields obtained from pseudo-spectral direct numerical solutions of the compressible three-dimensional MHD equations, with the Hall term included, have been carried out by Dmitruk et al. (2003) and Dmitruk & Matthaeus (2006). In both experiments electrons and protons were accelerated within very short times before particles left the simulation box (with length size of the order of a few turbulent correlation lengths). The momentum distribution functions very quickly develop long high-energy tails.

For electrons, there is no substantial difference found between the results with and without the Hall term in the MHD solution, while for protons significant differences are seen in the low-momentum part of the distributions. When a background uniform magnetic field (the guiding field) is added, the particle acceleration is anisotropic. Electrons develop large parallel momentum, while protons develop large perpendicular momentum similar to those reported for a single current sheet in Section 4.4.

4.6.3 Acceleration in stochastic current sheets

Turkmani et al. (2005, 2006) have investigated the issue of particle acceleration in a 3-D coronal MHD model developed by Galsgaard & Nordlund (1996). The initial setting for the model is a straight stratified coronal loop with a magnetic field which extends between the two photospheric footpoints. The response of the loop to random photospheric motions is then followed. A turbulent cascade develops, leading to a formation of multiple current sheets in the corona. The resulting electric fields comprise both the inductive electric field and the resistive one, the latter appearing from the hybrid resistivity used in the model of Galsgaard & Rousev (2002). However, it is found that the impact of the (mainly perpendicular) inductive field on acceleration is weak. The distribution of current sheets changes in time with the turbulence development, giving rise to the possibility of very bursty particle acceleration events.

In order to study particle acceleration in this environment, the magnetic field topology deduced from the MHD simulation is assumed to be quasi-stationary, similar to that in Section 3.3. Then, test particles are followed through their motion in the electromagnetic fields associated with the multiple current sheets, using the relativistic equations of motion (Equation 4.14). The model also allows particles to leave the loop once they hit the boundaries, thus limiting their energy gain. The simulation results show different types of particle dynamics, with particles both gaining and losing energy; however, not surprisingly, most leave the loop with net energy gain. About one quarter of the particles do not interact with the current sheet at all and thus gain no energy.

The results show that the resistive electric field, being a parallel field, is the principal means of accelerating particles. The acceleration is very fast and efficient, accelerating particles to relativistic energies in a very short time. The resulting distribution function of accelerated particles has a clear double-power-law structure, with a thermal component at low energies (Turkmani et al. 2006).

The MHD model currently in use produces particles with higher energies at somewhat shorter times compared to the Cellular Automata model discussed above (Vlahos et al. 2004). This is likely because of different choices in the basic parameters, especially the magnetic field strength and density. The same MHD model accelerates both electrons and protons without any need to adjust the electric fields, contrary to the CA-based model. The double power law does not arise in the CA model because of the possibility of particle loss in the MHD model. Both approaches show that fragmented current sheets in the corona are a reasonable scenario for particle acceleration.

Décamp & Malara (2006) performed a test-particle numerical experiment to simulate particle acceleration in the low-frequency turbulent environment generated by footpoint motions in a coronal loop. Only the effect of the resistive electric field E is retained, which is mainly parallel to the axial magnetic field. In the spatial frequency spectrum, the contribution of small scales is dominant. The spatial structure of E is obtained by a synthetic turbulence method (p -model), which allows intermittency with a power-law distribution to be reproduced. Spatial intermittency plays a key role in acceleration, enhancing both an extension of a power-law range, and an increase in the maximum energy.

By solving the relativistic equations of motion, the time evolution of the particle distribution can be determined. Electrons are accelerated to energies of the order of 50 keV in less than 0.3 s, and the final energy distribution also exhibits a power law. A correlation is found between heating events and particle acceleration that is qualitatively similar to that in the stochastic models discussed in Section 3.4.

4.6.4 Limitations of MHD turbulence models

With all their attractiveness in accounting for observed electron distributions in solar flares, models invoking MHD turbulence in an ensemble of current sheets nevertheless have a few essential problems.

First, MHD models involving multiple current sheets inevitably inherit the same size- and time-step problems as the PIC simulations discussed in Section 4.8, allowing us to simulate MHD turbulence and electron acceleration in only a very small region (about 1 m^3). It is then assumed, without justification, that the results from this small volume can be extended to the coronal scale.

Second, the basic model of a current sheet (discussed in Section 3.3) is still used for the energy gains by accelerated particles in these reconnecting current sheets, while more realistic 3-D models of the reconnecting current sheets (as discussed in Sections 4.4 and 4.5) show the energy gains to be significantly different.

Third, even if, as suggested above, multiple current sheets are formed in the whole flare volume, the diffusion regions in each have to be connected somewhere to reconnecting magnetic field lines. In a single current sheet model (see Sections 3.3 and 4.4), and as also shown in the original magnetic field restoration from the magnetograms taken at the photosphere (Vlahos et al. 2004), these lines are embedded in the photosphere. The trajectory simulations presented in Section 4.4 show that the particle drifts follow the magnetic field lines of the main magnetic component and move towards the photosphere, not parallel to the solar surface. Therefore, in the proposed multi-current sheet models, the issue arises as to how the test particle can move across the magnetic field, in order to get to the another current sheet (see, in this context, Emslie & Héroux 1995).

Last, but not least, a major problem arises from the fact that these simulations inherit the most common limitations related to the test-particle approach, as discussed in Section 4.7.

4.7 Limitations of the test particle approach

As discussed above in Sections 3.2 (basic reconnection in a single 2-D current sheet), 3.4 (acceleration by shocks and/or plasma turbulence), 4.4 and 4.5 (reconnection in 3-D geometries), and 4.6 (MHD models incorporating multiple reconnection sites), a considerable amount of simulation of the particle acceleration process involves a use of “test particles” moving in a prescribed electromagnetic field configuration. Such a test-particle approach is certainly useful at some level – for example, it allows us to investigate the individual trajectories of electrons and protons inside 3-D current sheets (Zharkova & Gordovskyy 2004; Dalla & Browning 2005; Wood & Neukirch 2005), and to obtain the aggregated energy distributions for a large volume of particles (Zharkova & Gordovskyy 2005a,b; Dalla & Browning 2005; Browning & Dalla 2007), which can be compared with those inferred from observations. The approach can be used iteratively to extend the results of exact PIC simulations to a much larger region (see Section 4.8).

However, considerable caution must be exercised when applying a test-particle approach to situations in which the number of accelerated particles is sufficiently large (see Section 2.1.3). In such cases, the electric and magnetic fields associated with the accelerated particles themselves rapidly become comparable to the fields pre-supposed at the outset. Recall (Section 2.1) that a major flare can accelerate some 10^{37} electrons s^{-1} and that these electrons propagate within a magnetic flux tube of order 10^9 cm in radius. Attempting to model this as a single large-scale ejection leads to the well-known (e.g., Holman 1985;

Emslie & Hénoux 1995) paradoxes that (1) the magnetic fields induced by the resulting current vastly exceed the pre-supposed field, and (2) that the electric fields resulting from both charge separation and induction effects associated with the accelerated particle stream (see Sections 4.4 and 4.8) exceed plausible values by even more absurd margins. Specifically:

- Ampère’s law, applied to a steady flow of 10^{37} electrons s^{-1} (current $I \approx 10^{18}$ Amps), in a cylinder of cross-sectional radius $r \approx 10^7$ m gives a corresponding magnetic field strength $B \approx \mu_o I / 2\pi r \approx 3 \times 10^4$ T $\approx 3 \times 10^8$ Gauss. Using a propagation volume $V \approx 10^{21}$ m^3 , the associated energy content $(B^2/2\mu_o)V \approx 10^{36}$ J $\approx 10^{43}$ ergs, at least ten orders of magnitude greater than the energy in the electron beam itself;
- The typical rise time for a hard X-ray burst in a solar flare is $\tau \approx 1 - 10$ s. To initiate a current I over a timescale τ in a volume of inductance $L \approx \mu_o \ell$ (where ℓ is the characteristic scale) requires a voltage $V \approx \mu_o \ell I / \tau$. Alternatively, the largest current that can appear when a voltage V is applied is $I \approx V \tau / \mu_o \ell$. With the characteristic voltage associated with the acceleration of hard-X-ray-producing electrons being ~ 30 kV, and with solar loop sizes $\ell \approx 10^7$ m, this gives a maximum current $I \approx 10^4$ Amps, some *fourteen* orders of magnitude less than the total current involved.

It is clear, therefore, that the self-consistent electromagnetic fields associated with electron acceleration rapidly become comparable to the fields pre-supposed to be present in the acceleration region; in such an environment, a test-particle approach breaks down severely. Given this, it is a clear imperative to take into account the self-consistent evolution of the electric and magnetic fields, *including the fields associated with the accelerated particles themselves*. Failure to do so can result in unrealistic numbers of accelerated particles predicted by acceleration models and even paradoxical results, such as the energy in accelerated particles exceeding the free energy in the pre-flare magnetic field configuration.

4.7.1 The polarization electric field

As discussed in Section 4.4 (see Figure 4.6), reconnection in a 3-D current sheet geometry leads to a separation of protons and electrons across the midplane. As shown in Figure 4.18, such a charge separation results in a substantial (up to 100 V cm^{-1}) Hall-type polarization electric field across the midplane. As pointed out in Section 3.2, inclusion of such Hall-type electric fields can significantly *increase* the effectiveness of the whole magnetic reconnection process (Birn et al. 2001; Huba & Rudakov 2004; Drake et al. 2005); see also Section 4.9.

Electrons, because of their much smaller gyroradii, typically do not show much change in behavior in the presence of the polarization field. On the other hand, protons, with their larger gyroradii, gain slightly more energy when they move in the positive x -direction than in the negative x -direction. The net (nonlinear) result is that protons gain energy as a result of the polarization field, thus tending to make the proton energy spectrum flatter. A full investigation of the effect of the polarization electric field requires use of a PIC approach, as described in Section 4.8.

4.7.2 Turbulent electric fields

Various turbulent electric fields typically form inside a reconnecting current sheet – these are caused, for example, by the two-stream instability (Bret 2009) of the two electron beams that enter the current sheet from opposite sides (Zharkova & Agapitov 2009). Such electric

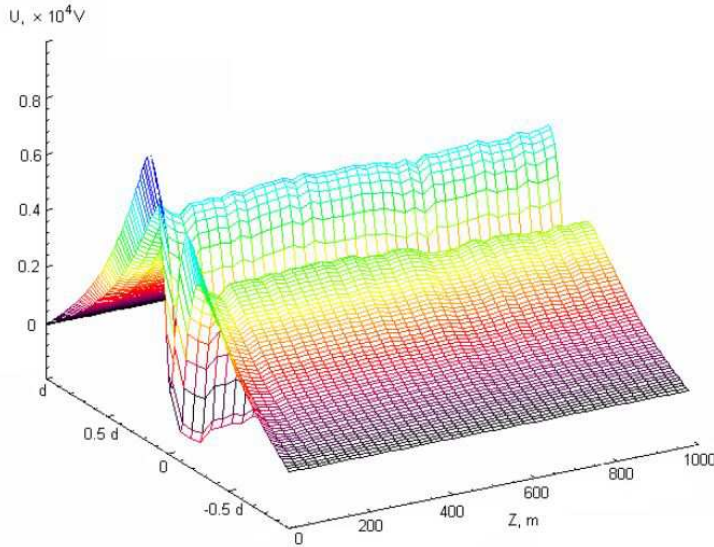


Fig. 4.18 Polarization electric field induced by the separation of protons and electrons accelerated in a 3-D current sheet with $B_0 = 10$ G, at various distances z from the null point (from Zharkova & Agapitov 2009).

fields, and their associated currents, typically oscillate near the plasma frequency and have an exponential growth rate Γ and an energy saturation level PE given by the analytical relations derived for the cold-beam plasma instability (Shapiro & Shevchenko 1988; Bret 2009):

$$\Gamma = \sqrt{1/3} 2^{-4/3} \Delta^{1/3} \omega_{pe}, \quad PE = (\Delta/2)^{1/3} E_{\text{beam}}, \quad (4.19)$$

where Δ is the ratio of the beam to plasma densities, and E_{beam} is the beam kinetic energy. The effect of the electric fields associated with such waves on the accelerated particle distributions was estimated by Zharkova & Agapitov (2009); this work confirmed the estimates of Bret (2009). Further progress requires full kinetic simulations.

4.8 Particle-in-cell simulation of acceleration in a 3-D RCS

As has been pointed out repeatedly above, a full description of the particle acceleration process in solar flares requires that the electromagnetic fields and currents associated with the accelerated particles be self-consistently included. In this section, we describe early efforts to accommodate this crucial element of the modeling.

4.8.1 Description of the PIC approach

In order to self-consistently include the electric and magnetic fields induced by the accelerated particles, one can use the 2D3V (PIC) simulation code (Verboncoeur & Gladd 1995). This PIC method solves the equations of motion for the plasma particles (see Equations 4.14), using values for the electric and magnetic fields which include both the pre-specified background fields \mathbf{E} and \mathbf{B} and the fields $\tilde{\mathbf{E}}$ and $\tilde{\mathbf{B}}$ associated with the accelerated particles, as calculated from Maxwell's equations.

In the 3-D simulations by Siversky & Zharkova (2009), the y -direction is chosen to be invariant. The system is periodic in the z -direction, so that a particle leaving the system through a boundary far from the reconnecting current sheet (see bottom of Figure 3.4) reappears at the opposite boundary. The current sheet half-thickness is taken to be 100 cm and the period along the x -direction is 2000 cm. In the PIC simulations discussed here, the computation region is extended well beyond the null point in order to explore the effect on the acceleration of different magnitudes of the transverse magnetic field. Plasma is continuously injected from the $x = \pm 1000$ cm boundaries of the simulation region.

In order to avoid numerical instabilities in the PIC method, constraints on the steps in time and space must be satisfied (for details, see Siversky & Zharkova 2009). To satisfy these conditions while keeping the code running time reasonable, an artificially low plasma number density $n = 10^{10} - 10^{12} \text{ m}^{-3}$ is used, and the proton-to-electron mass ratio is artificially reduced to $m_p/m_e = 100$. The spatial simulation grid has from 10 to 100 cells in the z direction and 100 cells in the x direction with $\Delta z = \lambda_D$ (the Debye length) and $\Delta x = \lambda_D/5$. There are ~ 100 particles per cell on average and the time step is 6×10^{-10} s.

4.8.2 PIC simulation results

The results of a simulation carried out with an extremely low number density $n = 10^4 \text{ cm}^{-3}$ are shown in Figure 4.19 for both protons (left panel) and electrons (right panel). This low-density simulation was performed mainly to verify that the PIC code can reproduce the results obtained in test-particle simulations (see Section 4.4, Figure 4.6).

Consistent with the test-particle results, the formation of separate beams of accelerated protons and electrons is clearly observed, and electrons and protons are ejected into the opposite semispaces with respect to the $x = 0$ midplane. The protons are largely unmagnetized inside the current sheet, so that the ejection velocity of the “bounced” and “transit” protons are almost the same. On the other hand, the electrons are much more magnetized, so that bounced electrons cannot reach the midplane and thus gain much less energy than transit electrons. In this particular case, however, the polarization electric field \tilde{E}_x caused by the charge separation is rather weak ($\sim 20 \text{ V m}^{-1}$). It must be noted, however, that the electron skin depth for this simulation is about 5000 cm, which exceeds by a large factor the size ($100 \text{ cm} \times 1000 \text{ cm}$) of the simulation region in both directions. The ion inertial length, which is also instrumental in controlling the electron/proton decoupling (Mandt et al. 1994b), is about 1000 cm, comparable to the size of the simulation region. Thus artificial decoupling of electrons and ion motions does result in this simulation.

Simulations for a higher density, $n = 10^6 \text{ cm}^{-3}$, are shown in Figure 4.20, for protons (left panel) and electrons (right panel). For this density the electron skin depth is reduced to ~ 500 cm, which is within the size of the simulation region in either direction. Thus the decoupling of electron and ion motions is not an artefact of the size of the region compared to the skin depth. Although the assumed density is several orders of magnitude lower than in the solar corona (often taken to be 10^{10} cm^{-3}), already several differences between the test-particle and PIC approaches appear. The dynamics of the relatively unmagnetized protons are not substantially different: their trajectories are close to those obtained from the test-particle simulations (Figure 4.6). They are still ejected mainly into one semispaces ($x < 0$) with respect to the midplane, and their acceleration rate coincides with the theoretical magnitude given in Section 3.3.

In addition, however, a small number of protons is ejected to the $x > 0$ semispaces, where electrons are normally ejected in test-particle simulations (Figure 4.20, left panel).

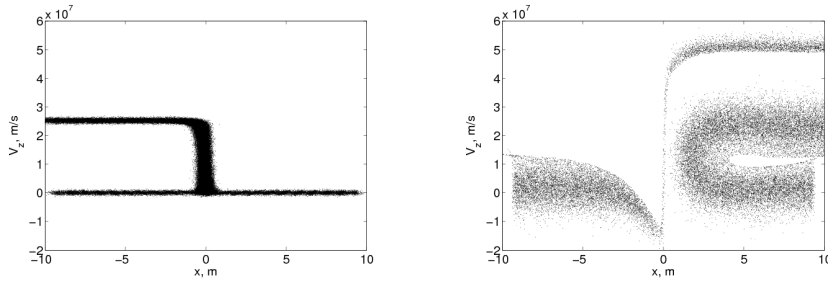


Fig. 4.19 PIC simulation snapshots of low-density ($n = 10^{10} \text{ m}^{-3}$) plasma particles on the x - V_z phase plane for protons (left plot) and electrons (right plot). The protons and the electrons enter the RCS from both sides and are ejected to opposite semiplanes either as a beam (transit particles) or as a flow (bounced particles); see the text for details. The current-sheet parameters are the same as in Section 4.4 (from Siversky & Zharkova 2009).

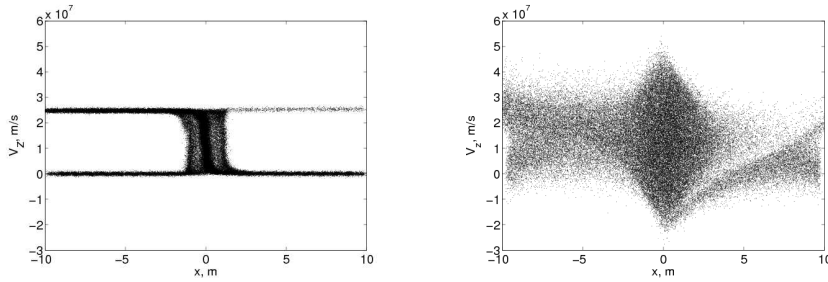


Fig. 4.20 Snapshots of higher-density plasma particles (10^{12} m^{-3}) on the x - V_z phase plane (PIC simulations) for protons (left plot) and electrons (right plot) entering the RCS from both sides. Protons are still ejected to the same semiplane, while the electrons form a cloud which experiences multiple ejections and returns to the acceleration region. As a result, the majority of the electrons ends up being ejected to the same semiplane as the protons, with only a small fraction of electrons being ejected into the opposite semiplane (see the text for details). The current sheet parameters are the same as in Section 4.4 (from Siversky & Zharkova 2009).

Figure 4.21 shows the fraction of the protons ejected into the $x > 0$ semispace as a function of B_{x0} and B_{y0} ; the dependence on B_{y0} qualitatively coincides with that obtained by Zharkova & Gordovskyy (2004). For small B_{y0} , both PIC and test-particle simulations show that the protons are ejected symmetrically with respect to the midplane. However, in the PIC simulation, all the protons are ejected into the one semispace ($x < 0$) when $B_{y0} > 7 \text{ G}$ ($\approx B_{z0}$), while in the test-particle simulation (Zharkova & Gordovskyy 2004), the accelerated particles are fully separated if $B_{y0} > 1.5 \times 10^{-2} B_{z0}$. Thus, in PIC simulations, the particle trajectories have less asymmetry than those in the test-particle approach.

4.8.3 Polarization electric field induced by accelerated particles

The PIC simulations show that the induced magnetic field $\tilde{\mathbf{B}}$ is typically much smaller than the background \mathbf{B} . On the other hand, inclusion of the induced *electric* field $\tilde{\mathbf{E}}$ is essential. Indeed, its absolute value is much larger (by an order of magnitude) than the field E_y induced by the reconnection itself (see Sections 4.4 and 4.7.1).

Figure 4.22 shows the value of the charge separation electric field \tilde{E}_x , perpendicular to the current sheet, averaged over the z coordinate, for different values of B_{x0} and B_{y0} . The field becomes stronger when either B_{x0} decreases or B_{y0} increases. Also, when $B_{y0} \rightarrow 0$, the

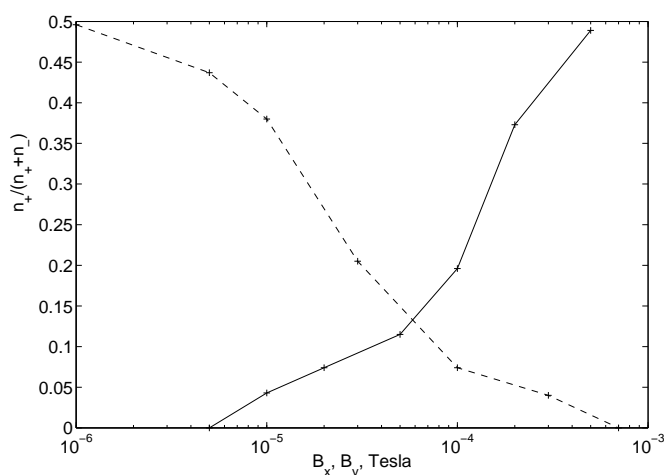


Fig. 4.21 The fraction of protons that are ejected into the $x > 0$ semispace, *Dashed line*: fraction vs. B_{y0} ($B_{x0} = 0.2$ G). *Solid line*: fraction vs. B_{x0} ($B_{y0} = 1$ G). All other parameters of the current sheet are the same as in Figure 4.20.

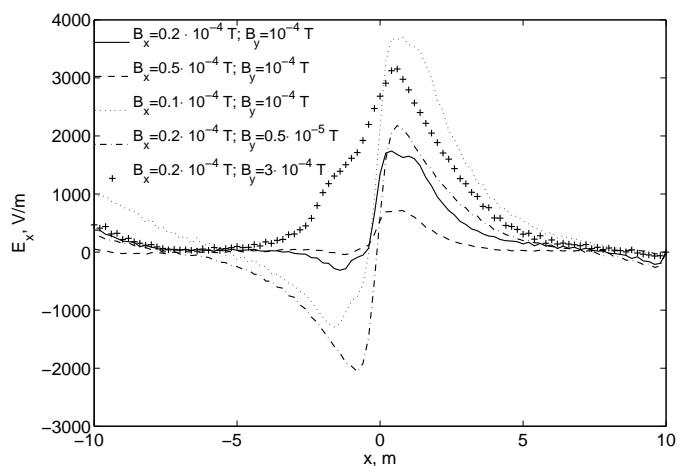


Fig. 4.22 Electric field \tilde{E}_x induced by particles in the PIC simulations for different values of B_{x0} and B_{y0} . All other parameters of the current sheet are the same as in Figure 4.20.

system becomes symmetric, and accordingly so does \tilde{E}_x . The distribution of the associated charge density $\rho(x) = (1/4\pi) \partial \tilde{E}_x / \partial x$ has been presented by Siversky & Zharkova (2009).

4.8.4 Particle trajectories

As discussed above, proton trajectories do not change much in the presence of the polarization field, the only difference being that the “bounced” protons have somewhat larger orbits

(Siversky & Zharkova 2009), leading to two smaller peaks at about ± 1 m in the charge density plot (Figure 7 in Siversky & Zharkova 2009).

The trajectories of electrons are much more complicated. First, electrons which enter from the $x < 0$ semispace have dynamics similar to those of the “transit” electrons: they drift towards the midplane, become accelerated and are ejected to the $x > 0$ semispace. However, the polarization field $\tilde{E}_x(x)$, which extends well beyond the current sheet thickness and has a component parallel to the magnetic field, acts to decelerate the ejected electrons. For the chosen magnitudes of B_x and B_y , the majority of electrons cannot escape to the $x > 0$ semispace; instead, they are dragged back multiple times to the current sheet and after some time become indistinguishable from the electrons that entered from the $x > 0$ semispace.

The electrons that come from the $x > 0$ semispace demonstrate rather different dynamics compared with the case when $\tilde{E}_x = 0$. These electrons, which are “bounced” from the RCS in the absence of an \tilde{E}_x , can now reach its midplane. In the vicinity of the midplane, electrons become unmagnetized and oscillate with a gyro-frequency determined by the magnitude of B_y (Figure 8 in Siversky & Zharkova 2009). After a large number of oscillations, the electron is ejected. If the electron’s initial velocity is small, it can become quasi-trapped inside the RCS, similar to the situation in the vicinity of an X-type null point (Petkaki & MacKinnon 1997). Such electrons are accelerated on the midplane, ejected from it, then decelerated outside the RCS and return back to the midplane. This cycle is repeated until the electron finally gains enough energy to escape the RCS. Since the magnitude of the polarization field $\tilde{E}_x(x)$ is smaller at $x < 0$ than at $x > 0$ (see Figure 4.22), it is easier for the electron to escape to the $x < 0$ semispace. Thus, eventually, *most of the electrons are ejected to the same semispace as protons*, contrary to the results of the test-particle simulations, while creating an electron cloud around an RCS before their joint ejection with protons. It seems that the asymmetry condition is shifted to much higher magnitudes of the guiding field than those found in the test-particle approach ($>0.01B_{z0}$, Zharkova & Gordovskyy 2004).

4.8.5 Energy spectra

As shown by Siversky & Zharkova (2009), the ejected electrons, in general, form a wide, single-peaked energy distribution with the width being of the order of the mean energy. This is different from the test-particle simulations, in which two narrow-energy electron beams are formed. Consistent with Section 4.4, the mean electron energy still strongly depends on B_x , with lower B_x corresponding to a higher mean energy and a wider energy distribution.

4.8.6 Turbulent electric field

Another interesting effect observed in the PIC simulations for the selected physical conditions and proton-to-ion mass ratio is the excitation of plasma waves.

As can be seen from Figure 4.23, the \tilde{E}_z component of the induced electric field is structured with a characteristic length scale of $\lambda_{\text{wave}} \approx 2$ m. This structure propagates in time in the positive z -direction at a speed $V_{\text{wave}} \approx 1.3 \times 10^7$ m s⁻¹. This corresponds to an oscillation period $T_{\text{wave}} \approx 1.5 \times 10^{-7}$ s, consistent with the plasma frequency for a density $n = 10^6$ cm⁻³. Note, also, that the oscillating component of the excited wave \tilde{E}_z is parallel to the direction of propagation which corresponds to the polarization of the Langmuir wave. The instability mechanism is evident from study of the electron velocity V_z . As shown in Figure 4.24, the electrons have an unstable “bump-on-tail” distribution. The range of velocities V_z for which the derivative $\partial f / \partial V_z$ is positive is from 1.3×10^9 to 2×10^9 cm s⁻¹, corresponding to the phase velocity of the associated Langmuir wave V_{wave} .

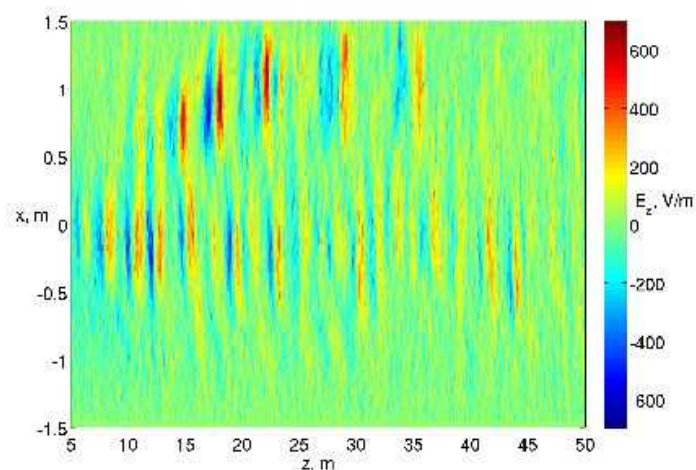


Fig. 4.23 Electric field \tilde{E}_z induced by particles in PIC simulation ($B_{z0} = 10^{-3}T$, $B_{y0} = 10^{-4}T$, $B_{x0} = 4 \times 10^{-5}T$, $E_{y0} = 250 \text{ V m}^{-1}$, $m_p/m_e = 10$, $n = 10^6 \text{ cm}^{-3}$).

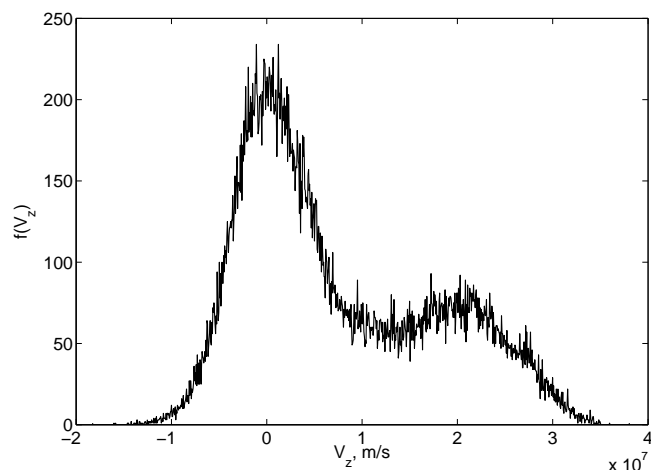


Fig. 4.24 Distribution function of electrons calculated for the region with turbulence plotted in Figure 4.23.

The use of plasma instabilities to produce anomalously high values of resistivity in the reconnection region have been studied by many authors. A comprehensive review of these results is beyond the scope of this article; however, a brief commentary is appropriate. Both 2-D and 2.5-D PIC simulations have revealed various types of instabilities to be present, from the lower hybrid drift instability (LHDI) leading to the Kelvin-Helmholtz instability (Landau & Lifshitz 1960; Chen et al. 1997; Lapenta et al. 2003) to kink (Pritchett et al. 1996; Zhu & Winglee 1996; Daughton 1999) and sausage (Büchner 1999) instabilities. However, full 3-D PIC simulations (with an artificially reduced speed of light $c = 15V_{Ae}$ and proton-to-electron mass ratio of 277.8; Zeiler et al. 2002), while retain-

ing the lower hybrid drift instability, reveal no evidence of kink or sausage instabilities. This indicates that the appearance of various instability modes may be dependent on the details of the simulation used, and hence argues for an abundance of caution at this time in applying these results to actual flares.

4.9 Particle acceleration in collapsing magnetic islands

4.9.1 Tearing-mode instability in current sheets

As mentioned in Section 3.2, in reconnecting current sheets, diffusion converts magnetic energy into Ohmic heat, with a concomitant slow expansion of the current sheet at a rate proportional to the resistivity. Consequently, one way of enhancing the reconnection rate is to consider enhancement of the resistivity through resistive instabilities such as the tearing instability (Furth et al. 1963).

In a current sheet wide enough to meet the condition $\tau_{dif} \gg \tau_A$, where $\tau_A = d/V_A$ is the Alfvén traverse time, the tearing instability occurs on a timescale of $\tau_{dif}(\tau_A/\tau_{dif})^\lambda$, with the parameter λ in the range $0 < \lambda < 1$. The tearing instability occurs on wavelengths greater than the width of the current sheet, ($ka < 1$), with a growth rate (Priest & Forbes 2000):

$$\omega = \left[\tau_{dif}^3 \tau_A^2 (ka)^2 \right]^{-1/5}, \quad (4.20)$$

where the wave number k satisfies the condition $(\tau_{dif}/\tau_A)^{1/4} < ka < 1$. The fastest growth is achieved for the longest wavelength (i.e., at $ka = 1$), while the smallest wavelength of the instability grows more slowly, on a timescale $\tau_{dif}^{3/5} \tau_A^{2/5}$. As first demonstrated by Furth et al. (1963) (see also Spicer 1977), tearing-mode instabilities generated during reconnection in a current sheet can produce closed magnetic “islands” with an elliptical O-type topology. Accordingly, large current sheets often observed in solar flares (e.g., see Sui & Holman 2003, and references therein) can, depending on their sizes and conditions, be subject to the formation of magnetic islands. For example, for a current sheet of size $\sim 10,000$ km (as reported by Sui & Holman 2003), embedded in a (coronal) medium with magnetic field $B \approx 100$ G and density $n = 10^{10} \text{ cm}^{-3}$, then the Alfvén velocity is about 2000 km s^{-1} and $\tau_A \approx 5$ sec. With a rather conservative collision frequency estimate 10^4 s^{-1} , $\tau_{dif} \approx 10^{15}$ sec. Substituting these values into Equation 4.20 gives an island formation time in the range $10 - 1000$ s.

4.9.2 Studying particle acceleration in magnetic islands using a PIC approach

In the past decade, the tearing-mode instability has been extensively investigated, both in 2.5-D current sheets (Drake et al. 1997; Shay & Drake 1998; Drake et al. 2005, 2006b,a) and in a full 3-D kinetic PIC approach (Zeiler et al. 2002; Pritchett & Coroniti 2004; Karimabadi et al. 2007; Shay et al. 2007; Daughton et al. 2009; Drake et al. 2010).

Shay & Drake (1998) studied the dynamics of whistler waves generated inside the magnetic islands, using a code in which the electric and magnetic fields were calculated at each time step using the Poisson condition $\nabla \cdot E = 4\pi\rho$. The time step was normalized to the electron cyclotron time Ω_e^{-1} , calculated for a maximum initial magnetic field B_0 , the spatial step normalized to the skin depth c/ω_{pe} , and the velocity normalized to the Alfvén velocity for electrons $V_{Ae} = B_0/\sqrt{4\pi n_0 m_e}$. The speed of light was artificially reduced to $5V_{Ae}$ in order to marginally resolve Debye radii. The simulation grid was 512×512 with 7 million particles

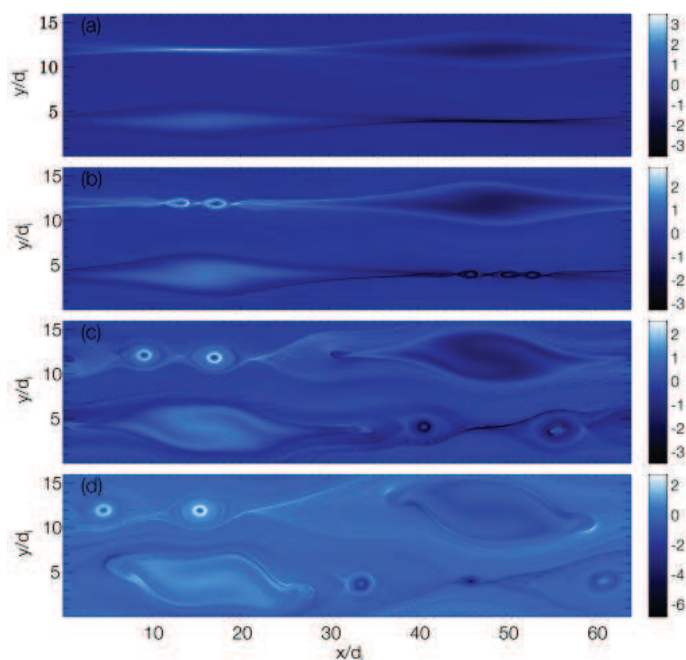


Fig. 4.25 Out-of-plane current density in 2.5-D PIC simulations of reconnection with a guiding field, for four consecutive time intervals, from top to bottom. The environment contains two current sheets and is characterized by the appearance of islands formed by the tearing instability. At the start, there are only (a) large islands, followed at later times (b-d) by the formation of smaller magnetic islands. Note that such islands do *not* appear in 2-D PIC simulations of the same environment without a guiding field. From Drake et al. (2006b).

involved. Small magnetic perturbations and associated currents were added as initial conditions to form seed magnetic islands centered around the two current layers, as shown in Figure 4.25. Using such a formalism, Shay & Drake (1998) were able to resolve the electron dissipation region, despite the use of an artificially low ion-to-electron mass ratio of 200.

A further modification of the PIC code was used to extend it to a 3-D model with 64 grid cells in the third direction, while increasing the proton-to-electron mass ratio to 277.8 and the speed of light to $c = 15V_{Ae}$ (Zeiler et al. 2002). Unlike a conventional Harris equilibrium, in which the variation of the density produces the equilibrium current, the density was taken to be nearly constant, with the current being produced by the $\mathbf{E} \times \mathbf{B}$ drift of the electrons. This resulted (see Figure 4.26) in a “parallel” electric field occurring in the plane of the island current sheet (Drake et al. 1997; Shay & Drake 1998; Zeiler et al. 2002). Pritchett & Coroniti (2004) have further shown that in 3-D current sheets with a guiding magnetic field, the “parallel” electric field is formed only in the two quadrants $(+x, +y)$ and $(-x, -y)$. Electrons entering these sectors are accelerated by this “parallel” electric field; the other quadrants are characterized by an excess of ions, strongly reminiscent of the drift separation of electrons and protons in a 3-D single current sheet (Sections 4.4 and 4.8).

Once formed, magnetic islands tend to shrink due to magnetic tension forces. Conservation of the longitudinal invariant leads to efficient first-order Fermi acceleration of particles tied to the island’s field lines. As shown by Drake et al. (2006a), the process of island shrink-

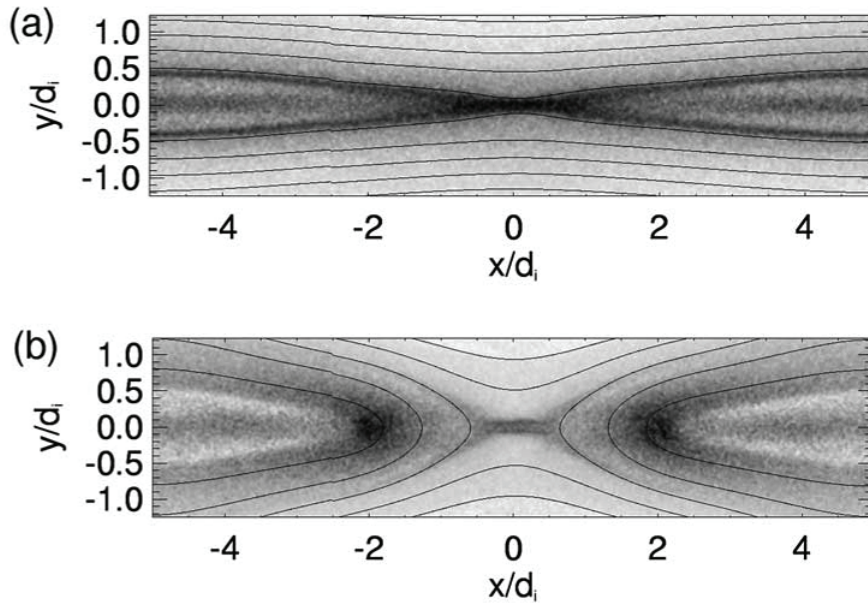


Fig. 4.26 Current density in PIC simulations for times (a) $t = 7.7/\omega_{ci}$ and (b) $t = 12.9/\omega_{ci}$. The solid lines correspond to magnetic flux lines. Adopted from Zeiler et al. (2002).

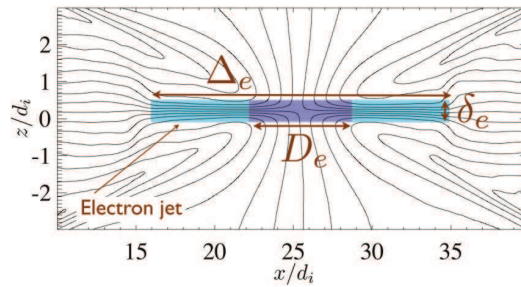


Fig. 4.27 The multi-scale structure of the electron diffusion region around an X-type null point of total length of Δ_e and thickness δ_e , as derived from 3-D PIC simulations. The solid lines show the electron trajectories for the time $t\omega_{ci} = 80$ (ω_{ci} is the ion cyclotron frequency). In the inner region of length D_e , there is a steady inflow of electrons and a strong out-of-plane current; the outer region is characterized by electron outflow jets. From Karimabadi et al. (2007).

ing halts when the kinetic energy of the accelerated particles is sufficient to halt the further collapse due to magnetic tension forces; the electron energy gain is naturally a large fraction of the released magnetic energy. A sufficient number of electrons can be produced to account for a moderately-sized solar flare. The resultant energy spectra of electrons take the form of power laws, with harder spectra corresponding to lower values of the plasma β . For the low- β conditions appropriate to the solar corona, the model predicts accelerated spectra that are much harder ($\delta \approx 1.5$) than observed.

Further progress with 3-D PIC simulations of magnetic islands, using a larger 2560×2560 grid, revealed that the electron diffusion region formed by the electron flows occurs

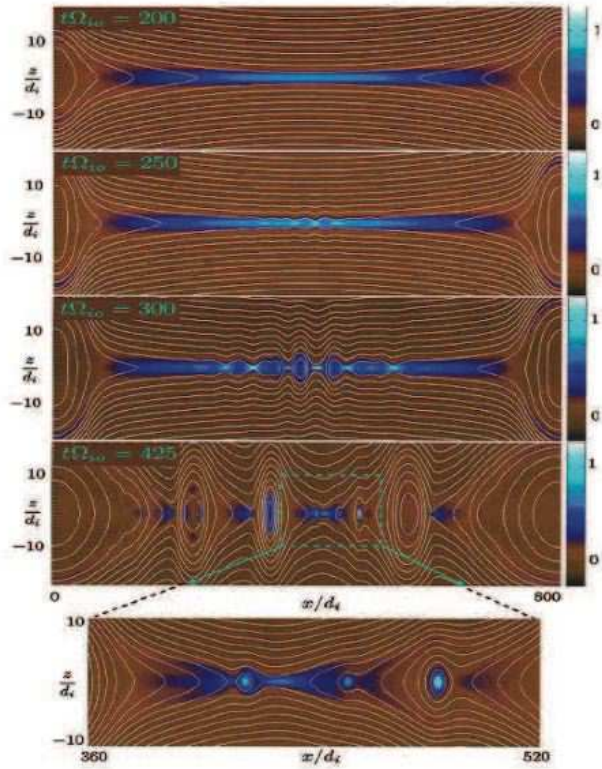


Fig. 4.28 Evolution of the current density over a region of extent $800d_i$ (where d_i is the ion inertial length), for different times t . White lines are the magnetic flux surfaces. The bottom plot presents a close-up of a region in which formation of new islands is occurring. From Daughton et al. (2009).

over a width of $5d_e$ (where d_e is the electron inertial length – Birn et al. 2001), while other simulations show an extent up to $20d_i$ (where d_i is the ion inertial length – Karimabadi et al. 2007; Shay et al. 2007); see Figure 4.27. The electron diffusion region becomes elongated with a two-scale structure: an inner region (size D_e in Figure 4.27) with a strong electron-drift-associated electric field (see Equation 3.9) and a wider diffusion region characterized by electron jets (Karimabadi et al. 2007; Shay et al. 2007). Shay et al. (2007) found that the electrons form super-Alfvénic outflow jets, which become decoupled from the magnetic field and extend to a large distance from the X-type null point, similar to the manner in which electron jets decouple from the protons in a test-particle approach to reconnection in a single 3-D current sheet (Section 4.4).

Recently, Daughton et al. (2009) showed that for collisional Sweet-Parker reconnection with Lundquist numbers S higher than 1000, the reconnection region becomes susceptible to the tearing instability, leading to the formation of many magnetic islands with half-thickness approaching the ion inertial length d_i (see Figure 4.28). This result shows that the current sheet size is a key factor in defining timescales and the role of different physical processes at different stages of the reconnection process. For example, the shrinking of a large current sheet during MHD reconnection is halted when it approaches a size conducive to the formation of magnetic islands.

4.10 Limitations of the PIC approach

Many PIC simulations (Birn et al. 2001; Drake et al. 2006b; Tsiklauri & Haruki 2007; Shay et al. 2007; Karimabadi et al. 2007) have been concerned with the study of reconnection rates in the vicinity of a magnetic X-type null. Even for the very low densities used in these simulations, it is apparent that the feedback of the fields induced by accelerated particles can be substantial (see Section 4.7): it can significantly modify the particle trajectories and the energies gained during their acceleration.

However, because of computer power limitations, the size of the region in which the induced electric and magnetic field are simulated and coupled to the particle motion is necessarily rather small: $\sim 100 \times 50 \times 1000$ cm for 2-D simulations (Birn et al. 2001; Tsiklauri & Haruki 2007), or $4000 \times 40000 \times 86$ cm for the most recent 3-D simulations (Shay et al. 2007; Drake et al. 2010). These are orders of magnitude smaller than the $10^8 - 10^{10}$ cm sizes associated with flares (Masuda et al. 1994; Sui & Holman 2003; Jiang et al. 2006). Only in the PIC simulations discussed in Section 4.8 is the computation region extended well beyond the null point in order to explore the variations of acceleration process, at different magnitudes of the transverse magnetic field. Thus, *the narrowness of the simulation region* still imposes strong limitations on the number of particles being accelerated in PIC simulations.

Other puzzling features of the simulations relate to the origin of the electric fields in the models. One example is the “parallel” electric field reported in many 3-D simulations (Zeiler et al. 2002; Pritchett & Coroniti 2004; Drake et al. 2010) and produced either as a result of an advective electric field (see the first term in Equation 3.9) and/or by a gradient of the magnetic field component across the current sheet (see the second term in Equation 3.9). This ‘parallel’ electric field is the electric field induced by accelerated electrons known as a self-induced (return-current) electric field associated with their propagation into a flaring atmosphere, which can exceed the local Dreicer field by a factor of up to ~ 30 (Zharkova & Gordovskyy 2006). Although both the “parallel” electric field, or the “self-induced (return current)” electric field associated with the propagation of accelerated electrons can cause various interesting effects (e.g., the charge separation electric field can decelerate electrons and even return them back to the acceleration region), causality arguments would strongly suggest that neither field can be considered as the main driver of particle acceleration since the field is *formed by the accelerated particles themselves*.

A related problem is the difference in electron and ion gyration radii/periods (Birn et al. 2001). Because of this difference, within a timescale of $\lesssim 10^{-7}$ s, electrons can move towards the midplane, be accelerated and ejected, while the protons have only just started their gyrations in the RCS environment. In the simulations to date, the proton-to-electron mass ratio has been arbitrarily lowered to 100-200, an order of magnitude smaller than the actual value. Even the speed of light is conveniently reduced by some one or two orders of magnitude to allow a reduction in simulation times (Birn et al. 2001; Drake et al. 2006a). Such simulations, then, serve to highlight that by artificially adjusting fundamental physical constants (such as the electron mass or the speed of light) in order to achieve results with a reasonable amount of computational effort, certain features of the results can be altered significantly. Although Shay & Drake (1998) have shown that the *reconnection rate* may be indeed insensitive to the adopted values of both the electron mass and speed of light.

Issues such as the ratio of macro- to micro-scales can be resolved only by increasing the reconnection region size in the PIC simulations up to sizes comparable with observations. However, even with exponential increases in computing power, there are substantial doubts that one can achieve this goal within the next few decades. Possibly a hybrid approach, com-

binning PIC simulations convoluted with test-particle extensions to greater source volumes, will allow us to make substantial progress in this area.

5 How well do Recent Theories Account for Observed Flare Characteristics?

5.1 Interrelation between acceleration and transport

Before we address the relative merits of the various particle acceleration models, it is important to realize that many flare observations consist of radiation integrated over the source volume; the quantity observed involves integration over not only space but also quantities such as particle pitch angles. Therefore, in order to relate to observed features (Section 2), one must incorporate the effects of particle acceleration with the *transport* of the accelerated particles throughout the remainder of the flaring source. Although such an inclusion will in all probability obscure information on the acceleration process, it can also, more profitably, be used as a diagnostic of particle transport processes themselves.

As we have seen (Sections 4.4, 4.5 and 4.6), accelerated electrons can attain quasi-relativistic energies within an extremely small timescale and can thus propagate over the extent of a solar flare of size $\sim 10^9$ cm within ~ 0.01 - 0.1 s. The proton acceleration time is longer than that for electrons by up to two orders of magnitude (Section 4.4), so that protons still remain within the acceleration region while the electrons are ejected from it. Thus, particle transport mechanisms are essential for completing the electric circuit for particles escaping the acceleration region (Emslie & Hénoux 1995) and/or in establishing co-spatial return currents (Knight & Sturrock 1977; Emslie & Hénoux 1995; Zharkova & Gordovskyy 2006). Such return currents can be formed both by ambient electrons (Knight & Sturrock 1977; Nocera et al. 1985) and by relatively high-energy beam electrons (Zharkova & Gordovskyy 2006) that return to the corona with nearly the same velocities as the injected electrons. The self-induced electric fields created by the beam electrons and/or the return current have a structure very favorable for the generation of plasma turbulence (Karlický & Bárta 2008), which naturally creates the conditions required for stochastic acceleration of electrons to sub-relativistic energies as discussed in Section 3.4 (see also Miller et al. 1996; Pryadko & Petrosian 1997).

Another issue that can arise is consideration of *radiative* transport effects, such as radiative transfer of optically-thick lines and continua, and reflection (or albedo effects) of emission of hard X-rays from the photosphere.

5.2 Testing acceleration models against observational constraints

Here we briefly summarize the extent to which the various models discussed in Section 4 have increased our ability to account for the characteristics (e.g., number, spectrum) of accelerated particles in a solar flare. In other words, can *any* hitherto-identified acceleration process produce the rate, number and energy spectrum of accelerated particles inferred from observations?

5.2.1 Stochastic acceleration

Stochastic acceleration remains one of the most promising candidates to account for most of the characteristics deduced from hard X-ray, radio and gamma-ray observations. This mechanism does, however, require a pre-supposed level of either plasma or MHD turbulence, the

basis for which has not yet been fully established. Further, high-frequency waves near the plasma frequency can be excluded as drivers for stochastic acceleration, since they would couple into a high level of decimetric radio emission in every flare, contrary to observations (Benz et al. 2005).

On the other hand, acceleration by transit-time damping *is* compatible with a frequent lack of radio emission because the frequency of the postulated MHD turbulence is far below the plasma frequency. The non-thermal electron distribution “grows” out of the thermal population, resulting in a “soft-hard-soft” evolution of the hard X-ray spectrum that is consistent with observations. Further, such “soft-hard-soft” behavior has been found in coronal sources, (Battaglia & Benz 2007) and is therefore inherent to the acceleration process and not to collisional transport effects. *RHESSI* observations showing the existence of a “pivot point” energy at which the differential electron flux does not vary with time, leading to the observed “soft-hard-soft” behavior, have been used (Grigis & Benz 2004) as evidence for a stochastic acceleration model.

Recent models of stochastic acceleration that involve the interaction of turbulence with high energy particle beams injected from elsewhere (Bykov & Fleishman 2009) can also account for some basic features of accelerated particles and their evolution with time. During the initial (linear) phase of the acceleration, effective particle acceleration by the longitudinal large scale turbulent motions, leading to visible spectral hardening. Then, because the accelerated particles eventually accumulate a considerable fraction of the turbulent energy, they deplete the energy in the turbulence, leading to a spectrum softening. Again, this is consistent with observations (Battaglia & Benz 2007) of “soft-hard-soft” spectral evolution in the main stage and even some hardening (soft-hard-harder behavior) during later stages (Krucker et al. 2007a).

5.2.2 Collapsing current sheets

Estimates of the electron energy gained in collapsing magnetic traps associated with reconnection in a helmet-type geometry, with and without a termination shock, reveal that there is a sufficient amount of energy released in accelerated particles during such a process. In addition, betatron acceleration, possibly coupled with first-order Fermi acceleration in collapsing current sheets, can account for the electron number and energies gained, although the energy spectrum of the accelerated particles resembles more the higher energy tail of a Maxwellian distribution. It remains to be established how the accelerated particles can move across the magnetic field of the trap in order to precipitate into the flare footpoints.

5.2.3 Acceleration in 3D reconnecting current sheets

New MHD simulations of particle acceleration rates and spectra from collapsing current sheets have revised our views on the efficiency of particle acceleration inside a diffusion region, although the number of particles (both electrons and protons) that can be accelerated in a current sheet is limited by the volume encompassed by the current sheet (Holman 1985; Litvinenko 1996a, see Section 3.3). However, more complex 3-D current sheets and/or multiple current sheets may be reconcilable with this model (see Sections 4.4 and 4.5). Acceleration of electrons in a 3-D RCS occurs mostly around the RCS midplane, over a very short timescale comparable with the growth rate of hard X-ray emission in solar flares. Acceleration of protons has a much longer timescale and results in a spread of protons in a location outside the midplane. The particle orbits in the RCS lead to a separation of electrons and protons into the opposite semiplanes, corresponding to ejection in opposite directions and

into opposite loop legs. The separation of electrons and protons during acceleration in an RCS leads to the formation of a polarization electric field (induced by Hall currents), which sets the frame for the generation of strong plasma turbulence that can lead to further particle acceleration by stochastic processes. Single 3-D current sheets with guiding fields have been found, through both test-particle and PIC approaches, to be able to supply sufficient energy into both electrons and protons in order to account for *RHESSI* hard X-ray and gamma-ray observations.

Spine reconnection in 3-D MHD reconnection simulations can naturally produce two symmetric jets of energetic particles escaping along the spine, while the fan reconnection produces azimuthally localized ribbons of high energy particles in the fan plane. Both features, in principle, are often observed in flares (e.g., magnetic jets in SOL2000-07-14T10:24, X5.7, and SOL2002-07-23T00:35, X4.8) and two-ribbon flares as discussed in Fletcher et al. (2011).

Another possibility involves tearing instabilities in current sheets, which leads to the formation of large numbers of magnetic islands, on which a large number of particles can be rapidly accelerated; however, the simulated electron energy spectra are much harder than inferred from hard X-ray observations.

Despite these qualified successes, there are two outstanding problems with this kind of acceleration model: (1) incorporation of the self-consistent electrodynamic fields associated with the accelerated particles; and (2) production of sufficient numbers of accelerated particles to match the observations. The latter can be marginally accounted for if one notes that strongly stressed 3-D current sheets, discussed in Sections 4.4 and 4.5, are characterized by much larger diffusion regions than in simple reconnection models (Section 3.2).

5.2.4 Complex reconnection models

The other way to tackle the particle number problem involves multiple dissipation sites associated with self-organized criticality (SOC) that could lead to “spreading” of the dissipation across a large coronal volume (see Section 4.6). Particles move between the current sheets, either gaining or losing energy in each one, resulting in a systematic second-order gain in energy. Particle energy distributions from the simulations fit the observed spectra for electrons very well, although proton spectra have yet to be simulated.

However, a few essential issues do remain:

1. The models invoke an *ad hoc* distribution of RCS sizes and physical conditions in order to account for the number and spectra of the accelerated particles;
2. The basic model of a current sheet (discussed in Section 3.3) is used to derive the energy gains by accelerated particles in a component current sheet, while the actual gains are significantly different in more realistic 3-D models of reconnecting current sheets;
3. Even if multiple current sheets are formed in the whole volume of the corona, there remains the issue of where the reconnecting magnetic field lines are embedded and how the test particles can move across the strong magnetic field threading the reconnection volume in order to reach another current sheet;
4. Some of these models also suffer from problems associated with the neglect of the feedback of the electric and magnetic fields associated with the accelerated particles themselves;
5. Multiple RCS models simulated with a more realistic PIC approach are applicable to only a very small region (about 10^6 cm^3), and it is assumed without justification that the results can be scaled to flare volumes.

6 Summary

Over the past decade, and especially in the *RHESSI* era, significant progress has been made in advancing various particle acceleration models and assessing their ability to account for the observed features in solar flares. *RHESSI* observations have been instrumental in encouraging the further development and exploration of both “traditional” and “non-traditional” mechanisms, including more complicated magnetic field geometries and topologies, to enhanced MHD and PIC models of magnetic reconnection in a single current sheet, to multiple current sheets and stochastic acceleration by various plasma waves. Substantial progress has been made through the use of phenomenological estimations made in collapsing traps, termination shocks of Alfvén waves, and direct simulations using both test-particle and self-consistent PIC approaches.

Consideration of the full three-dimensionality of the magnetic reconnection process has been found to significantly enhance the acceleration efficiency in current-sheet diffusion regions. However, the question still remains whether such a mechanism can account for the very large number of electrons responsible for hard X-ray emission and whether consideration of the whole electric circuit formed by precipitating and returning beams in reconnecting loops can resolve the particle number problem. PIC simulations have demonstrated that the acceleration of substantial numbers of charged particles causes a number of important secondary effects: for example, polarization electric fields induced by separation of electrons and protons towards the midplane, return currents formed from precipitating and ambient electrons, and plasma turbulence related to beam instabilities.

Interactions of large-scale loops with strong magnetic fields can lead either to acceleration in collapsing traps by betatron and/or first-order Fermi mechanisms, or to acceleration in the termination shock formed by such the collapsing sheets (or by large-scale Alfvén waves produced during the reconnection). Interaction of smaller-scale magnetic fields can produce magnetic islands or multiple current sheets in which particles can be also accelerated in a cascade processes if the particle travels and gains energy from one feature or another.

The exact acceleration scenario will depend on the magnetic field topology and on the absolute magnitudes of physical parameters. Further, it is possible, or even likely, that all the acceleration processes discussed above play some role in solar flares and elsewhere in astrophysics. The strict demands imposed by the *RHESSI* observations have necessitated a thorough and critical review of all these models, leading to substantial new understanding along the way.

Acknowledgements AGE acknowledges support from the NASA Heliophysics Division and from UC Berkeley. EPK acknowledge the support of a PPARC/STFC Rolling Grant, PPARC/STFC UK Advanced Fellowship and Royal Society Conference Grant and by the European Commission through the SOLAIRE Network (MTRN-CT-2006-035484). AGE and EPK were also supported in part by a grant from the International Space Science Institute (ISSI) in Bern, Switzerland. NV acknowledges support from Centre National d’Etudes Spatiales (CNES) and from the French program on Solar-Terrestrial Physics (PNST) of INSU/CNRS for the participation to the *RHESSI* project. VZ acknowledges the support of the Science Technology and Facility Council (STFC) project PP/E001246/1. The computational work for the test-particle and PIC simulations was carried out on the joint STFC and SFC (SRIF) funded cluster at the University of St Andrews, UK.

References

- T. Amano, M. Hoshino, *Physical Review Letters* **104**(18), 181102 (2010), 1004.3838, doi:10.1103/PhysRevLett.104.181102

- E. Amato, P. Blasi, *Mon. Not. Roy. Astron. Soc.* **364**, L76 (2005), arXiv:astro-ph/0509673, doi:10.1111/j.1745-3933.2005.00110.x
- A. Anastasiadis, C. Gontikakis, N. Vilmer, L. Vlahos, *Astron. Astrophys.* **422**, 323 (2004), doi:10.1051/0004-6361:20035712
- S. K. Antiochos, C. R. DeVore, J. A. Klimchuk, *Astrophys. J.* **510**, 485 (1999), arXiv:astro-ph/9807220, doi:10.1086/306563
- T. D. Arber, M. Haynes, *Physics of Plasmas* **13**(11), 112105 (2006), doi:10.1063/1.2375039
- K. Arzner, A. O. Benz, *Solar Phys.* **231**, 117 (2005), arXiv:astro-ph/0503145, doi:10.1007/s11207-005-1590-8
- K. Arzner, L. Vlahos, *Astrophys. J. Lett.* **605**, L69 (2004), arXiv:astro-ph/0402605, doi:10.1086/392506
- A. Asai, H. Nakajima, M. Shimojo, S. M. White, H. S. Hudson, R. P. Lin, *Pub. Astron. Soc. Japan* **58**, L1 (2006)
- M. J. Aschwanden, *Astrophys. J.* **661**, 1242 (2007), doi:10.1086/516814
- M. J. Aschwanden, R. M. Bynum, T. Kosugi, H. S. Hudson, R. A. Schwartz, *Astrophys. J.* **487**, 936 (1997), doi:10.1086/304633
- M. J. Aschwanden, R. A. Schwartz, *Astrophys. J.* **464**, 974 (1996), doi:10.1086/177385
- M. J. Aschwanden, M. J. Wills, H. S. Hudson, T. Kosugi, R. A. Schwartz, *Astrophys. J.* **468**, 398 (1996), doi:10.1086/177700
- G. Aulanier, E. E. DeLuca, S. K. Antiochos, R. A. McMullen, L. Golub, *Astrophys. J.* **540**, 1126 (2000), doi:10.1086/309376
- H. Aurass, G. Mann, *Astrophys. J.* **615**, 526 (2004), doi:10.1086/424374
- H. Aurass, G. Rausche, G. Mann, *Astron. Astrophys.* **471**, L37 (2007), doi:10.1051/0004-6361:20077544
- H. Aurass, B. Vršnak, G. Mann, *Astron. Astrophys.* **384**, 273 (2002), doi:10.1051/0004-6361:20011735
- T. Bai, R. Ramaty, *Astrophys. J.* **219**, 705 (1978), doi:10.1086/155830
- A. Barnes, J. V. Hollweg, *J. Geophys. Res.* **79**, 2302 (1974), doi:10.1029/JA079i016p02302
- T. S. Bastian, G. D. Fleishman, D. E. Gary, *Astrophys. J.* **666**, 1256 (2007), 0704.2413, doi:10.1086/520106
- M. Battaglia, A. O. Benz, *Astron. Astrophys.* **456**, 751 (2006), arXiv:astro-ph/0606353, doi:10.1051/0004-6361:20065233
- M. Battaglia, A. O. Benz, *Astron. Astrophys.* **466**, 713 (2007), arXiv:astro-ph/0702309, doi:10.1051/0004-6361:20077144
- M. Battaglia, A. O. Benz, *Astron. Astrophys.* **499**, L33 (2009), 0904.4146, doi:10.1051/0004-6361/200912143
- T. E. Bell, *Astronomy* **6**, 6 (1978)
- S. G. Benka, G. D. Holman, *Astrophys. J.* **435**, 469 (1994), doi:10.1086/174829
- A. Benz (ed.), *Plasma Astrophysics, second edition*, volume 279 of *Astrophysics and Space Science Library* (2002)
- A. O. Benz, P. C. Grigis, A. Csillaghy, P. Saint-Hilaire, *Solar Phys.* **226**, 121 (2005), arXiv:astro-ph/0410436, doi:10.1007/s11207-005-5254-5
- A. O. Benz, H. Perret, P. Saint-Hilaire, P. Zlobec, *Advances in Space Research* **38**, 951 (2006), doi:10.1016/j.asr.2005.09.030
- C. K. Birdsall, A. B. Langdon, *Plasma physics via computer simulation / Charles K. Birdsall, A. Bruce Langdon* (McGraw-Hill, New York :, 1985)
- J. Birn, J. F. Drake, M. A. Shay, B. N. Rogers, R. E. Denton, M. Hesse, M. Kuznetsova, Z. W. Ma, A. Bhattacharjee, A. Otto, P. L. Pritchett, *J. Geophys. Res.* **106**, 3715 (2001), doi:10.1029/1999JA900449
- J. Birn, L. Fletcher, M. Hesse, T. Neukirch, *Astrophys. J.* (2009)
- D. Biskamp, *Nonlinear Magnetohydrodynamics* (1997)
- R. D. Blandford, J. P. Ostriker, *Astrophys. J. Lett.* **221**, L29 (1978), doi:10.1086/182658
- S. A. Bogachev, B. V. Somov, *Astronomy Letters* **31**, 537 (2005), doi:10.1134/1.2007030
- S. A. Bogachev, B. V. Somov, *Astronomy Letters* **33**, 54 (2007), doi:10.1134/S1063773707010070
- A. Bret, *Astrophys. J.* **699**, 990 (2009), 0903.2658, doi:10.1088/0004-637X/699/2/990
- J. W. Brosius, S. M. White, *Astrophys. J. Lett.* **641**, L69 (2006), doi:10.1086/503774
- J. C. Brown, *Solar Phys.* **18**, 489 (1971)
- J. C. Brown, in *Coronal Disturbances*, ed. by G. A. Newkirk (1974), volume 57 of *IAU Symposium*, pp. 395–+
- J. C. Brown, R. Bingham, *Astron. Astrophys.* **131**, L11 (1984)
- J. C. Brown, A. J. Conway, M. J. Aschwanden, *Astrophys. J.* **509**, 911 (1998), doi:10.1086/306522
- J. C. Brown, A. G. Emslie, E. P. Kontar, *Astrophys. J. Lett.* **595**, L115 (2003), doi:10.1086/378169
- J. C. Brown, E. P. Kontar, A. M. Veronig, in *Lecture Notes in Physics, Berlin Springer Verlag*, ed. by K.-L. Klein & A. L. MacKinnon (2007), volume 725 of *Lecture Notes in Physics, Berlin Springer Verlag*,

- pp. 65–+
- P. Browning, S. Dalla, *Memorie della Societa Astronomica Italiana* **78**, 255 (2007)
- J. Büchner, *Astrophys. Spa. Sci.* **264**, 25 (1999)
- S. V. Bulanov, S. I. Syrovatskii, *Motion of charged particles in the vicinity of a magnetic-field zero line* (1976), pp. 114–126
- A. M. Bykov, G. D. Fleishman, *Astrophys. J. Lett.* **692**, L45 (2009), 0901.2677, doi:10.1088/0004-637X/692/1/L45
- A. M. Bykov, I. N. Toptygin, in *International Cosmic Ray Conference* (1993), volume 2 of *International Cosmic Ray Conference*, pp. 267–+
- P. J. Cargill, *Astrophys. J.* **376**, 771 (1991), doi:10.1086/170325
- A. Caspi, R. P. Lin, *Astrophys. J. Lett.* **725**, L161 (2010), 1105.2839, doi:10.1088/2041-8205/725/2/L161
- F. F. Chen, *Introduction to plasma physics* (1974)
- Q. Chen, A. Otto, L. C. Lee, *J. Geophys. Res.* **102**, 151 (1997), doi:10.1029/96JA03144
- E. L. Chupp, in *American Institute of Physics Conference Series*, ed. by S. E. Woosley (1984), volume 115 of *American Institute of Physics Conference Series*, pp. 641–+
- E. L. Chupp, O. A. Benz, *Astrophys. J. Suppl.* **90**, 511 (1994)
- E. L. Chupp, D. J. Forrest, P. R. Higbie, A. N. Suri, C. Tsai, P. P. Dunphy, *Nature* **241**, 333 (1973), doi:10.1038/241333a0
- E. L. Chupp, J. M. Ryan, *Research in Astronomy and Astrophysics* **9**, 11 (2009), doi:10.1088/1674-4527/9/1/003
- N. B. Crosby, M. J. Aschwanden, B. R. Dennis, *Solar Phys.* **143**, 275 (1993), doi:10.1007/BF00646488
- R. B. Dahlburg, S. K. Antiochos, T. A. Zang, *Physics of Fluids B* **4**, 3902 (1992), doi:10.1063/1.860347
- S. Dalla, P. K. Browning, *Astron. Astrophys.* **436**, 1103 (2005), doi:10.1051/0004-6361:20042589
- S. Dalla, P. K. Browning, *Astrophys. J. Lett.* **640**, L99 (2006), doi:10.1086/503302
- S. Dalla, P. K. Browning, *Astron. Astrophys.* **491**, 289 (2008), 0811.1144, doi:10.1051/0004-6361:200809771
- D. W. Datlowe, R. P. Lin, *Solar Phys.* **32**, 459 (1973), doi:10.1007/BF00154958
- W. Daughton, *Physics of Plasmas* **6**, 1329 (1999), doi:10.1063/1.873374
- W. Daughton, V. Roytershteyn, B. J. Albright, H. Karimabadi, L. Yin, K. J. Bowers, *Physical Review Letters* **103**(6), 065004 (2009), doi:10.1103/PhysRevLett.103.065004
- C. Dauphin, N. Vilmer, *Astron. Astrophys.* **468**, 289 (2007), doi:10.1051/0004-6361:20066247
- L. Davis, *Physical Review* **101**, 351 (1956), doi:10.1103/PhysRev.101.351
- N. Décamp, F. Malara, *Astrophys. J. Lett.* **637**, L61 (2006), doi:10.1086/500450
- P. Demoulin, J. C. Héroux, E. R. Priest, C. H. Mandrini, *Astron. Astrophys.* **308**, 643 (1996)
- P. Démoulin, E. R. Priest, D. P. Lonie, *J. Geophys. Res.* **101**, 7631 (1996), doi:10.1029/95JA03558
- B. R. Dennis, H. S. Hudson, S. Krucker, in *Lecture Notes in Physics, Berlin Springer Verlag*, ed. by K.-L. Klein & A. L. MacKinnon (2007), volume 725 of *Lecture Notes in Physics, Berlin Springer Verlag*, pp. 33–+
- A. Des Jardins, R. Canfield, D. Longcope, C. Fordyce, S. Waitukaitis, *Astrophys. J.* **693**, 1628 (2009), doi:10.1088/0004-637X/693/2/1628
- P. Dmitruk, W. H. Matthaeus, *Journal of Geophysical Research (Space Physics)* **111**, 12110 (2006), doi:10.1029/2006JA011988
- P. Dmitruk, W. H. Matthaeus, N. Seenu, M. R. Brown, *Astrophys. J. Lett.* **597**, L81 (2003), doi:10.1086/379751
- J. F. Drake, D. Biskamp, A. Zeiler, *Geophys. Res. Lett.* **24**, 2921 (1997), doi:10.1029/97GL52961
- J. F. Drake, Y. C. Lee, *Physical Review Letters* **39**, 453 (1977), doi:10.1103/PhysRevLett.39.453
- J. F. Drake, M. Opher, M. Swisdak, J. N. Chamoun, *Astrophys. J.* **709**, 963 (2010), 0911.3098, doi:10.1088/0004-637X/709/2/963
- J. F. Drake, M. A. Shay, W. Thongthai, M. Swisdak, *Physical Review Letters* **94**(9), 095001 (2005), doi:10.1103/PhysRevLett.94.095001
- J. F. Drake, M. Swisdak, H. Che, M. A. Shay, *Nature* **443**, 553 (2006a), doi:10.1038/nature05116
- J. F. Drake, M. Swisdak, K. M. Schoeffler, B. N. Rogers, S. Kobayashi, *Geophys. Res. Lett.* **33**, 13105 (2006b), doi:10.1029/2006GL025957
- G. A. Dulk, D. J. McLean, *Solar Phys.* **57**, 279 (1978), doi:10.1007/BF00160102
- D. C. Ellison, et al., in *International Cosmic Ray Conference* (2005), volume 3 of *International Cosmic Ray Conference*, pp. 261–+
- A. G. Emslie, *Astrophys. J.* **235**, 1055 (1980), doi:10.1086/157709
- A. G. Emslie, *Astrophys. J.* **245**, 711 (1981), doi:10.1086/158846
- A. G. Emslie, *Astrophys. J. Lett.* **595**, L119 (2003), doi:10.1086/378168
- A. G. Emslie, J. C. Brown, A. L. MacKinnon, *Astrophys. J.* **485**, 430 (1997), doi:10.1086/304423

- A. G. Emslie, J.-C. Héroux, *Astrophys. J.* **446**, 371 (1995), doi:10.1086/175796
- A. G. Emslie, E. P. Kontar, S. Krucker, R. P. Lin, *Astrophys. J. Lett.* **595**, L107 (2003), doi:10.1086/378931
- A. G. Emslie, J. A. Miller, J. C. Brown, *Astrophys. J. Lett.* **602**, L69 (2004), doi:10.1086/382350
- A. G. Emslie, P. A. Sturrock, *Solar Phys.* **80**, 99 (1982), doi:10.1007/BF00153426
- E. Fermi, *Physical Review* **75**, 1169 (1949), doi:10.1103/PhysRev.75.1169
- L. Fletcher, H. S. Hudson, *Astrophys. J.* **675**, 1645 (2008), 0712.3452, doi:10.1086/527044
- L. Fletcher, T. R. Metcalf, D. Alexander, D. S. Brown, L. A. Ryder, *Astrophys. J.* **554**, 451 (2001), doi:10.1086/321377
- L. Fletcher et al., *Space Sci. Rev.* pp. XXX–XXX (2011)
- T. G. Forbes, *Astrophys. J.* **305**, 553 (1986), doi:10.1086/164268
- D. J. Forrest, in *Positron-Electron Pairs in Astrophysics*, ed. by M. L. Burns, A. K. Harding, & R. Ramaty (1983), volume 101 of *American Institute of Physics Conference Series*, pp. 3–14, doi:10.1063/1.341119
- H. P. Furth, J. Killeen, M. N. Rosenbluth, *Physics of Fluids* **6**, 459 (1963), doi:10.1063/1.1706761
- K. Galsgaard, Å. Nordlund, *Astrophysical Letters Communications* **34**, 175 (1996)
- K. Galsgaard, I. Roussev, *Astron. Astrophys.* **383**, 685 (2002), doi:10.1051/0004-6361:20011733
- J. Giacalone, J. R. Jokipii, *J. Geophys. Res.* **101**, 11095 (1996), doi:10.1029/96JA00394
- M. L. Goldstein, *Astrophys. J.* **219**, 700 (1978), doi:10.1086/155829
- V. S. Gorbachev, B. V. Somov, *Soviet Astronomy* **33**, 57 (1989)
- P. C. Grigis, A. O. Benz, *Astron. Astrophys.* **426**, 1093 (2004), arXiv:astro-ph/0407431, doi:10.1051/0004-6361:20041367
- P. C. Grigis, A. O. Benz, *Astron. Astrophys.* **434**, 1173 (2005), arXiv:astro-ph/0501431, doi:10.1051/0004-6361:20042265
- P. C. Grigis, A. O. Benz, *Astron. Astrophys.* **458**, 641 (2006), arXiv:astro-ph/0606339, doi:10.1051/0004-6361:20065809
- R. J. Hamilton, V. Petrosian, *Astrophys. J.* **398**, 350 (1992), doi:10.1086/171860
- J. V. Hollweg, *J. Geophys. Res.* **79**, 1357 (1974), doi:10.1029/JA079i010p01357
- G. D. Holman, *Astrophys. J.* **293**, 584 (1985), doi:10.1086/163263
- G. D. Holman, L. Sui, R. A. Schwartz, A. G. Emslie, *Astrophys. J. Lett.* **595**, L97 (2003), doi:10.1086/378488
- G. Holman et al., *Space Sci. Rev.* pp. XXX–XXX (2011)
- J. D. Huba, L. I. Rudakov, *Physical Review Letters* **93**(17), 175003 (2004), doi:10.1103/PhysRevLett.93.175003
- H. S. Hudson, *Solar Phys.* **24**, 414 (1972), doi:10.1007/BF00153384
- G. J. Hurford, S. Krucker, R. P. Lin, R. A. Schwartz, G. H. Share, D. M. Smith, *Astrophys. J. Lett.* **644**, L93 (2006), doi:10.1086/505329
- G. J. Hurford, R. A. Schwartz, S. Krucker, R. P. Lin, D. M. Smith, N. Vilmer, *Astrophys. J. Lett.* **595**, L77 (2003), doi:10.1086/378179
- H. Isliker, L. Vlahos, *Phys. Rev. E* **67**(2), 026413 (2003), arXiv:physics/0211113, doi:10.1103/PhysRevE.67.026413
- V. Jayanti, J. V. Hollweg, *J. Geophys. Res.* **98**, 19049 (1993), doi:10.1029/93JA02208
- Y. W. Jiang, S. Liu, W. Liu, V. Petrosian, *Astrophys. J.* **638**, 1140 (2006), arXiv:astro-ph/0508532, doi:10.1086/498863
- T. W. Jones, *Astrophys. J. Suppl.* **90**, 969 (1994), doi:10.1086/191934
- S. R. Kane, E. L. Chupp, D. J. Forrest, G. H. Share, E. Rieger, *Astrophys. J. Lett.* **300**, L95 (1986), doi:10.1086/184610
- H. Karimabadi, W. Daughton, J. Scudder, *Geophys. Res. Lett.* **34**, 13104 (2007), doi:10.1029/2007GL030306
- M. Karlický, M. Bárta, *Solar Phys.* **247**, 335 (2008), doi:10.1007/s11207-008-9115-x
- M. Karlický, T. Kosugi, *Astron. Astrophys.* **419**, 1159 (2004), doi:10.1051/0004-6361:20034323
- J. Kašparová, M. Karlický, E. P. Kontar, R. A. Schwartz, B. R. Dennis, *Solar Phys.* **232**, 63 (2005), arXiv:astro-ph/0508636, doi:10.1007/s11207-005-1581-9
- C. A. Kletzing, *J. Geophys. Res.* **99**, 11095 (1994), doi:10.1029/94JA00345
- J. W. Knight, P. A. Sturrock, *Astrophys. J.* **218**, 306 (1977), doi:10.1086/155683
- E. P. Kontar, J. C. Brown, *Astrophys. J. Lett.* **653**, L149 (2006), arXiv:astro-ph/0611170, doi:10.1086/510586
- E. P. Kontar, A. G. Emslie, A. M. Massone, M. Piana, J. C. Brown, M. Prato, *Astrophys. J.* **670**, 857 (2007), 0707.4225, doi:10.1086/521977
- E. P. Kontar, A. G. Emslie, M. Piana, A. M. Massone, J. C. Brown, *Solar Phys.* **226**, 317 (2005), arXiv:astro-ph/0409691, doi:10.1007/s11207-005-7150-4
- E. P. Kontar, A. L. MacKinnon, *Solar Phys.* **227**, 299 (2005), arXiv:astro-ph/0506097, doi:10.1007/s11207-005-1101-y
- E. Kontar et al., *Space Sci. Rev.* pp. XXX–XXX (2011)

- R. A. Kopp, G. W. Pneuman, *Solar Phys.* **50**, 85 (1976), doi:10.1007/BF00206193
- A. G. Kosovichev, V. V. Zharkova, *Astrophys. J. Lett.* **550**, L105 (2001), doi:10.1086/319484
- D. Krauss-Varban, D. Burgess, *J. Geophys. Res.* **96**, 143 (1991), doi:10.1029/90JA01728
- D. Krauss-Varban, D. Burgess, C. S. Wu, *J. Geophys. Res.* **94**, 15089 (1989), doi:10.1029/JA094iA11p15089
- D. Krauss-Varban, C. S. Wu, *J. Geophys. Res.* **94**, 15367 (1989), doi:10.1029/JA094iA11p15367
- S. Krucker, M. Battaglia, P. J. Cargill, L. Fletcher, H. S. Hudson, A. L. MacKinnon, S. Masuda, L. Sui, M. Tomczak, A. L. Veronig, L. Vlahos, S. M. White, *Astron. Astrophys. Rev.* **16**, 155 (2008a), doi:10.1007/s00159-008-0014-9
- S. Krucker, E. P. Kontar, S. Christe, R. P. Lin, *Astrophys. J. Lett.* **663**, L109 (2007a), doi:10.1086/519373
- S. Krucker, P. Saint-Hilaire, S. Christe, S. M. White, A. D. Chavier, S. D. Bale, R. P. Lin, *Astrophys. J.* **681**, 644 (2008b), doi:10.1086/588549
- S. Krucker, S. M. White, R. P. Lin, *Astrophys. J. Lett.* **669**, L49 (2007b), doi:10.1086/523759
- L. D. Landau, E. M. Lifshitz, *Electrodynamics of continuous media* (1960)
- S. H. Langer, V. Petrosian, *Astrophys. J.* **215**, 666 (1977), doi:10.1086/155400
- G. Lapenta, J. U. Brackbill, W. S. Daughton, *Physics of Plasmas* **10**, 1577 (2003), doi:10.1063/1.1560615
- T. N. Larosa, A. G. Emslie, *Solar Phys.* **120**, 343 (1989), doi:10.1007/BF00159883
- Y.-T. Lau, J. M. Finn, *Astrophys. J.* **350**, 672 (1990), doi:10.1086/168419
- J. Leach, *The Impulsive Hard X-Rays from Solar Flares.*, Ph.D. thesis, AA(STANFORD UNIVERSITY.) (1984)
- M. M. Leroy, A. Mangeney, *Annales Geophysicae* **2**, 449 (1984)
- R. P. Lin, S. Krucker, G. J. Hurford, D. M. Smith, H. S. Hudson, G. D. Holman, R. A. Schwartz, B. R. Dennis, G. H. Share, R. J. Murphy, A. G. Emslie, C. Johns-Krull, N. Vilmer, *Astrophys. J. Lett.* **595**, L69 (2003), doi:10.1086/378932
- Y. E. Litvinenko, *Solar Phys.* **167**, 321 (1996a), doi:10.1007/BF00146342
- Y. E. Litvinenko, *Astrophys. J.* **462**, 997 (1996b), doi:10.1086/177213
- Y. E. Litvinenko, B. V. Somov, *Solar Phys.* **146**, 127 (1993a), doi:10.1007/BF00662174
- Y. E. Litvinenko, B. V. Somov, *Solar Phys.* **146**, 127 (1993b)
- W. Liu, *Characteristics of Solar Flare Hard X-ray Emissions: Observations and Models*, Ph.D. thesis, Stanford University (2006)
- E. T. Lu, R. J. Hamilton, *Astrophys. J. Lett.* **380**, L89 (1991), doi:10.1086/186180
- Z. W. Ma, A. Bhattacharjee, *Geophys. Res. Lett.* **23**, 1673 (1996), doi:10.1029/96GL01600
- M. E. Mandt, R. E. Denton, J. F. Drake, *Geophys. Res. Lett.* **21**, 73 (1994a), doi:10.1029/93GL03382
- M. E. Mandt, R. E. Denton, J. F. Drake, *Geophys. Res. Lett.* **21**, 73 (1994b), doi:10.1029/93GL03382
- G. Mann, H. Aurass, A. Warmuth, *Astron. Astrophys.* **454**, 969 (2006), doi:10.1051/0004-6361:20064990
- G. Mann, A. Warmuth, H. Aurass, *Astron. Astrophys.* **494**, 669 (2009), doi:10.1051/0004-6361:200810099
- J. T. Mariska, J. M. McTiernan, *Astrophys. J.* **514**, 484 (1999), doi:10.1086/306927
- P. C. H. Martens, A. Young, *Astrophys. J. Suppl.* **73**, 333 (1990), doi:10.1086/191469
- S. Masuda, T. Kosugi, H. Hara, S. Tsuneta, Y. Ogawara, *Nature* **371**, 495 (1994), doi:10.1038/371495a0
- K. G. McClements, L. Fletcher, *Astrophys. J.* **693**, 1494 (2009), doi:10.1088/0004-637X/693/2/1494
- S. W. McIntosh, P. Charbonneau, T. J. Bogdan, H.-L. Liu, J. P. Norman, *Phys. Rev. E* **65**(4), 046125 (2002), doi:10.1103/PhysRevE.65.046125
- D. B. Melrose, S. M. White, *Proceedings of the Astronomical Society of Australia* **3**, 369 (1979)
- J. A. Miller, P. J. Cargill, A. G. Emslie, G. D. Holman, B. R. Dennis, T. N. LaRosa, R. M. Winglee, S. G. Benka, S. Tsuneta, *J. Geophys. Res.* **102**, 14631 (1997), doi:10.1029/97JA00976
- J. A. Miller, T. N. Larosa, R. L. Moore, *Astrophys. J.* **461**, 445 (1996), doi:10.1086/177072
- J. A. Miller, D. A. Roberts, *Astrophys. J.* **452**, 912 (1995), doi:10.1086/176359
- G. J. Newkirk, *Astrophys. J.* **133**, 983 (1961), doi:10.1086/147104
- L. Nocera, I. I. Skrynnikov, B. V. Somov, *Solar Phys.* **97**, 81 (1985), doi:10.1007/BF00152980
- A. V. Oreshina, B. V. Somov, *Astronomy Letters* **26**, 750 (2000a), doi:10.1134/1.1323282
- A. V. Oreshina, B. V. Somov, *Astronomy Letters* **26**, 750 (2000b), doi:10.1134/1.1323282
- G. K. Parks, J. R. Winckler, *Astrophys. J. Lett.* **155**, L117+ (1969), doi:10.1086/180315
- P. Petkaki, A. L. MacKinnon, *Solar Phys.* **172**, 279 (1997)
- V. Petrosian, T. Q. Donaghy, J. M. McTiernan, *Astrophys. J.* **569**, 459 (2002), arXiv:astro-ph/0112363, doi:10.1086/339240
- V. Petrosian, S. Liu, *Astrophys. J.* **610**, 550 (2004), arXiv:astro-ph/0401585, doi:10.1086/421486
- V. Petrosian, H. Yan, A. Lazarian, *Astrophys. J.* **644**, 603 (2006), arXiv:astro-ph/0508567, doi:10.1086/503378
- H. E. Petschek, *NASA Special Publication* **50**, 425 (1964)
- E. Priest, T. Forbes, *Magnetic Reconnection* (Cambridge University Press, Cambridge, UK, 2000)
- E. R. Priest, *Solar magneto-hydrodynamics* (1982)

- E. R. Priest, T. N. Bungey, V. S. Titov, *Geophysical and Astrophysical Fluid Dynamics* **84**, 127 (1997), doi:10.1080/03091929708208976
- E. R. Priest, P. Démoulin, *J. Geophys. Res.* **100**, 23443 (1995), doi:10.1029/95JA02740
- E. R. Priest, T. G. Forbes, *Astron. Astrophys. Rev.* **10**, 313 (2002), doi:10.1007/s001590100013
- E. R. Priest, V. S. Titov, *Royal Society of London Philosophical Transactions Series A* **354**, 2951 (1996), doi:10.1098/rsta.1996.0136
- P. L. Pritchett, F. V. Coroniti, *Journal of Geophysical Research (Space Physics)* **109**, 1220 (2004), doi:10.1029/2003JA009999
- P. L. Pritchett, F. V. Coroniti, V. K. Decyk, *J. Geophys. Res.* **101**, 27413 (1996), doi:10.1029/96JA02665
- J. M. Pryadko, V. Petrosian, *Astrophys. J.* **482**, 774 (1997), arXiv:astro-ph/9610148, doi:10.1086/304168
- J. M. Pryadko, V. Petrosian, *Astrophys. J.* **495**, 377 (1998), arXiv:astro-ph/9706050, doi:10.1086/305271
- P. Saint-Hilaire, A. O. Benz, *Astron. Astrophys.* **435**, 743 (2005), doi:10.1051/0004-6361:20041918
- A. A. Schekochihin, S. C. Cowley, *Turbulence and Magnetic Fields in Astrophysical Plasmas* (Springer, 2007), pp. 85–
- R. Schlickeiser, J. A. Miller, *Astrophys. J.* **492**, 352 (1998), doi:10.1086/305023
- V. D. Shapiro, V. I. Shevchenko, *Soviet Scientific Reviews E Astrophysics and Space Physics Reviews* **6**, 425 (1988)
- G. H. Share, R. J. Murphy, *Washington DC American Geophysical Union Geophysical Monograph Series* **165**, 177 (2006)
- M. A. Shay, J. F. Drake, *Geophys. Res. Lett.* **25**, 3759 (1998), doi:10.1029/1998GL900036
- M. A. Shay, J. F. Drake, M. Swisdak, *Physical Review Letters* **99**(15), 155002 (2007), 0704.0818, doi:10.1103/PhysRevLett.99.155002
- K. Shibata, S. Masuda, M. Shimojo, H. Hara, T. Yokoyama, S. Tsuneta, T. Kosugi, Y. Ogawara, *Astrophys. J. Lett.* **451**, L83+ (1995), doi:10.1086/309688
- A. Y. Shih, R. P. Lin, G. J. Hurford, S. E. Boggs, A. C. Zoglauer, C. B. Wunderer, J. G. Sample, P. Turin, S. McBride, D. M. Smith, H. Tajima, P. N. Luke, M. S. Amman, in *Bulletin of the American Astronomical Society* (2009a), volume 41 of *Bulletin of the American Astronomical Society*, pp. 436–
- A. Y. Shih, R. P. Lin, D. M. Smith, *Astrophys. J. Lett.* **698**, L152 (2009b), doi:10.1088/0004-637X/698/2/L152
- T. V. Siversky, V. V. Zharkova, *Journal of Plasma Physics* p. xx (2009), doi:10.1017/S0022377809008009
- B. V. Somov (ed.), *Physical processes in solar flares.*, volume 172 of *Astrophysics and Space Science Library* (1992)
- B. V. Somov (ed.), *Cosmic Plasma Physics*, volume 251 of *Astrophysics and Space Science Library* (2000)
- B. V. Somov, T. Kosugi, *Astrophys. J.* **485**, 859 (1997), doi:10.1086/304449
- B. U. Ö. Sonnerup, in *Magnetospheric Boundary Layers*, ed. by B. Battrock, J. Mort, G. Haerendel, & J. Ortner (1979), volume 148 of *ESA Special Publication*, pp. 395–397
- D. S. Spicer, *Solar Phys.* **53**, 305 (1977), doi:10.1007/BF00160276
- L. Spitzer, *Physics of Fully Ionized Gases* (1962)
- K. Stasiewicz, P. Bellan, C. Chaston, C. Kletzing, R. Lysak, J. Maggs, O. Pokhotelov, C. Seyler, P. Shukla, L. Stenflo, A. Streltsov, J.-E. Wahlund, *Space Science Reviews* **92**, 423 (2000)
- J. J. Sudol, J. W. Harvey, *Astrophys. J.* **635**, 647 (2005), doi:10.1086/497361
- L. Sui, G. D. Holman, *Astrophys. J. Lett.* **596**, L251 (2003), doi:10.1086/379343
- P. A. Sweet, *Annual Rev Astron. Astrophys.* **7**, 149 (1969), doi:10.1146/annurev.aa.07.090169.001053
- S. I. Syrovatskii, *The physical nature of solar flares* (1981), pp. 21–41
- T. Takakura, T. Kosugi, T. Sakao, K. Makishima, M. Inada-Koide, S. Masuda, *Pub. Astron. Soc. Japan* **47**, 355 (1995)
- E. Tandberg-Hanssen, A. G. Emslie, *The physics of solar flares* (1988)
- V. S. Titov, G. Hornig, *Advances in Space Research* **29**, 1087 (2002), doi:10.1016/S0273-1177(02)00021-2
- G. Trotter, N. Vilmer, C. Barat, A. Benz, A. Magun, A. Kuznetsov, R. Sunyaev, O. Terekhov, *Astron. Astrophys.* **334**, 1099 (1998)
- D. Tsiklauri, T. Haruki, *Physics of Plasmas* **14**(11), 112905 (2007), 0708.1699, doi:10.1063/1.2800854
- S. Tsuneta, T. Naito, *Astrophys. J. Lett.* **495**, L67+ (1998), arXiv:astro-ph/9801109, doi:10.1086/311207
- R. Turkmani, P. J. Cargill, K. Galsgaard, L. Vlahos, H. Isliker, *Astron. Astrophys.* **449**, 749 (2006), doi:10.1051/0004-6361:20053548
- R. Turkmani, U. Torkelsson, *Astron. Astrophys.* **409**, 813 (2003), arXiv:astro-ph/0307559, doi:10.1051/0004-6361:20031167

- R. Turkmani, L. Vlahos, K. Galsgaard, P. J. Cargill, H. Isliker, *Astrophys. J. Lett.* **620**, L59 (2005), doi:10.1086/428395
- G. H. J. van den Oord, *Astron. Astrophys.* **234**, 496 (1990)
- G. E. Vekstein, P. K. Browning, *Physics of Plasmas* **4**, 2261 (1997), doi:10.1063/1.872555
- A. B. Verboncoeur, J. P. Langdon, N. T. Gladd, *Comp. Phys. Comm.* **87**, 199 (1995), doi:10.1016/0010-4655(94)00173-Y
- N. Vilmer, A. L. MacKinnon, G. Trottet, C. Barat, *Astron. Astrophys.* **412**, 865 (2003), doi:10.1051/0004-6361:20031488
- N. Vilmer, G. Trottet, C. Barat, R. A. Schwartz, S. Enome, A. Kuznetsov, R. Sunyaev, O. Terekhov, *Astron. Astrophys.* **342**, 575 (1999)
- N. Vilmer et al., *Space Sci. Rev.* pp. XXX–XXX (2011)
- L. Vlahos, H. Isliker, F. Lepreti, *Astrophys. J.* **608**, 540 (2004), arXiv:astro-ph/0402645, doi:10.1086/386364
- H. Wang, C. Liu, Y. Deng, H. Zhang, *Astrophys. J.* **627**, 1031 (2005), doi:10.1086/430418
- A. Warmuth, G. Mann, H. Aurass, *Central European Astrophysical Bulletin* **31**, 135 (2007)
- A. Warmuth, G. Mann, H. Aurass, *Astron. Astrophys.* **494**, 677 (2009), doi:10.1051/0004-6361:200810101
- S. White et al., *Space Sci. Rev.* pp. XXX–XXX (2011)
- P. Wood, T. Neukirch, *Solar Phys.* **226**, 73 (2005), doi:10.1007/s11207-005-5686-y
- C. C. Wu, *Geophys. Res. Lett.* **10**, 545 (1983), doi:10.1029/GL010i007p00545
- A. Zeiler, D. Biskamp, J. F. Drake, B. N. Rogers, M. A. Shay, M. Scholer, *Journal of Geophysical Research (Space Physics)* **107**, 1230 (2002), doi:10.1029/2001JA000287
- V. V. Zharkova, O. V. Agapitov, *Journal of Plasma Physics* **75**, 159 (2009), doi:10.1017/S002237780800771X
- V. V. Zharkova, M. Gordovskyy, *Astrophys. J.* **604**, 884 (2004), doi:10.1086/381966
- V. V. Zharkova, M. Gordovskyy, *Mon. Not. Roy. Astron. Soc.* **356**, 1107 (2005a), doi:10.1111/j.1365-2966.2004.08532.x
- V. V. Zharkova, M. Gordovskyy, *Space Science Reviews* **121**, 165 (2005b), doi:10.1007/s11214-006-6027-7
- V. V. Zharkova, M. Gordovskyy, *Astron. Astrophys.* **432**, 1033 (2005c), doi:10.1051/0004-6361:20041102
- V. V. Zharkova, M. Gordovskyy, *Astrophys. J.* **651**, 553 (2006), doi:10.1086/506423
- V. V. Zharkova, S. I. Zharkov, S. S. Ipson, A. K. Benkhalil, *Journal of Geophysical Research (Space Physics)* **110**, 8104 (2005), doi:10.1029/2004JA010934
- Z. Zhu, R. M. Winglee, *J. Geophys. Res.* **101**, 4885 (1996), doi:10.1029/95JA03144

Index

- above-the-looptop sources, 3
- abundances, 9
 - and acceleration of heavy ions, 9
 - Ne/O ratio, 9
- accelerated particles
 - energy spectra, 25, 43, 53, 60
 - 3-D reconnection, 38
 - energy-dependent index, 5
 - spectral index, 36
 - heavy ions, 9
 - number problem, 62
 - transport, 59
- acceleration
 - Alfvén waves, 26
 - and magnetic reconnection, 14
 - and particle transport, overview, 59
 - 3-D reconnection, 61
 - collapsing traps, 60
 - current sheets, 61
 - electric circuit, 59
 - magnetic islands, 61
 - radiative transport, 60
 - return current, 59
 - self-organized criticality, 61
 - stochastic acceleration, 60
 - transit-time damping, 60
 - turbulence, 59
 - and pitch-angle change, 30
 - betatron, 24, 29
 - cellular automaton model, 42
 - collapsing magnetic trap, 29, 60
 - conditions for runaway, 14
 - direct electric field, 43
 - electron-proton asymmetry, 33, 49, 61
 - dependence on strength of guide field, 35
 - electrons
 - by Alfvén waves, 25
 - timescales, 4
 - Fermi
 - first order, 22, 24, 29
 - in shrinking islands, 56
 - second order, 22
 - in chromosphere, 26
 - in current sheets, 32
 - fan and spine geometry, 37
 - illustration, 35, 36
 - multiple, 41
 - in Dreicer field, 14
 - in MHD turbulence, 4, 22, 44, 46
 - test-particle experiments, 44
 - in PIC approach, 55
 - list of mechanisms, 13
 - models, 13
 - multiple current sheets
 - issues, 46
 - particle-in-cell (PIC), 49
 - limitations, 57
 - pre-acceleration of ions, 23
 - pre-flare phase, 13
 - proton
 - need for pre-acceleration, 23
 - shock, 21
 - quasi-parallel, 21
 - quasi-perpendicular, 21
 - “seed” particles, 21
 - termination, 30
 - shock-drift, 24, 30
 - electrons, 30
 - illustration, 31
 - similarities of shock and turbulent mechanisms, 23
 - sources of electric field, 14
 - stochastic, 22, 23, 25, 60
 - ad hoc* waves, 23
 - spectrum not a power law, 23
 - limitations of models, 25, 46, 62
 - MHD turbulence, 60
 - multiple current sheets, 42, 61
 - net electrical current, 25
 - parameter dependence, 23
 - resonant cascade, 23
 - stochastic current sheets, 45
 - test-particle approach, 4, 24
 - limitations, 47, 62
 - transit-time damping, 22, 25, 60
- acceleration region
 - bulk acceleration, 25
 - charge separation, 59

- escape from, 3
- replenishment, 8
- test-particle approach, 4, 47
- turbulence, 24, 25
- active regions
 - fractal structure, 43
 - high Alfvén speed, 27
- albedo, 6, 7
- Alfvén speed, 20
 - and electron thermal speed, 27
 - and injection, 23
 - and termination shock, 29
 - gradient in chromosphere, 27
 - in the impulsive phase, 27
- beams, 8
 - electric field, 25
 - electron-proton asymmetry, 49
- bounced particles, 33, 49
- bremsstrahlung
 - electron-electron, 5
 - multithermal, 5
 - nonthermal, 5
 - thermal, 4
 - thick-target, 8
- cartoons
 - collapsing trap
 - illustration, 29
 - Poynting-flux transport
 - illustration, 26
 - standard, 28
- caveats
 - acceleration in test-particle approach, 46
 - specific problems, 47
 - limitation of test-particle approach, 24, 33
 - limits of MHD approach, 20
 - MHD turbulent acceleration
 - list of problems, 46
- cellular automata, 24, 42
- Cherenkov resonance, 22
- collapsing magnetic trap, 61
- Compton scattering, 6
- continuum
 - cyclotron maser, 12
 - fast-mode waves, 23
 - hard X-ray, 8
- cooling
 - conductive, 4
- coronal sources, 3, 10, 12, 13, 40
 - HXR and decimetric, 12
- cosmic rays
 - shock acceleration, 21
- current sheets, 4, 19
 - 3-D, 24, 33
 - and particle acceleration, 18, 32
 - and proton Larmor radius, 21
 - collapsing trap, 61
 - electric fields, 20
 - fan plane, 37
 - instability, 54
 - non-neutral, 18, 19
 - illustration, 18
 - observed in flares, 54
 - outflows, 28
 - physical conditions, 20
 - PIC simulations, 48
 - stochastic, 45
 - strong guide field, 35
- de Hoffmann-Teller frame, 30
- diffusion coefficient
 - angular, 22
 - energy, 22
- diffusion region, 15, 20
- directivity
 - hard X-ray, 6
- distribution functions
 - bump-on-tail, 38
- Dreicer field, 14, 20, 43
- drift speed
 - strong drift regime, 38
- electric fields
 - advective, 58
 - inadequacy as a driver, 58
 - and particle acceleration, 3
 - Dreicer, 14
 - Hall, 47
 - in current sheets, 20
 - induced by particles, 10, 25
 - large-scale, 14
 - MHD current-sheet assumption, 20
 - PIC simulations
 - induced polarization field, 51
 - turbulent, 52

- polarization, 34, 47, 61
 - induced by asymmetric acceleration, 51
- problem of origin in simulations, 58
- reconnection
 - convective, 20
- return current, 58
 - inadequacy as a driver, 58
- sub-Dreicer, 4
- super-Dreicer, 4, 41
- turbulent, 48
- electrodynamical feedback, 24
- electron beams
 - and return current, 25
 - and two-stream instability, 48
 - and type III bursts, 12
 - high-energy return current, 59
 - inductive fields, 47
- electrons
 - accelerated
 - associated current, 8
 - density, 8
 - energy content, 8
 - flux, 8
 - number, 8
 - collision losses, 5
 - distribution function
 - bump-on-tail, 53
 - Maxwellian, 14
 - mean electron distribution, 6
 - dominant tail population, 25
 - injected distribution, 8
 - mildly relativistic, 12
 - number problem, 7
 - total energy, 9, 10
- equations of motion, 33, 45
 - relativistic, 33
- filaments
 - eruptive, 3
- flare (individual)
 - SOL1992-01-13T17:25 (M2.0)
 - above-the-loop-top source, 3
 - SOL2000-07-14T10:24 (X5.7)
 - ribbons in, 61
 - SOL2002-02-26T10:27 (C9.6)
 - illustration, 6
 - SOL2002-07-23T00:35 (X4.8)
 - flare-related changes, 13
- footpoint differences, 10
- γ -rays, 11
- hard X-rays, 11
- illustration, 11
- ribbons in, 61
- time delays, 9
- SOL2002-08-20T08:25 (M3.4)
 - low-energy cutoff, 7
- SOL2003-10-28T11:10 (X17.2), 8
 - gamma-rays, 11
 - illustration, 7
 - termination shock, 30, 32
- SOL2005-07-13T14:49 (M5.0), 10
 - illustration, 10
- flare models
 - breakout, 3
 - cellular automaton, 24, 41, 42, 45
 - illustration, 42, 43
 - PIC simulation, 44
 - Poynting flux
 - illustration, 26
 - reconnection, 14
 - standard
 - illustration, 28
 - thick-target, 5, 10, 25, 44
 - thin-target, 10
 - wave energy transport, 26
- flare types
 - two-ribbon, 61
- flares
 - and acceleration, 3
 - energy content
 - accelerated particles, 7
- Fokker-Planck equation, 22
- footpoint simultaneity, 27
- footpoints, 3
 - Alfvén-wave transport, 27
 - and collapsing traps, 61
 - and simultaneous coronal sources, 10
 - motions, 28
 - generation of turbulence, 45
 - spectral equality, 10
- frequency
 - collision, 5, 24
 - and runaway, 14
 - Larmor, 22, 52
 - plasma, 23, 25, 48
 - plasma fundamental and harmonic, 12

- spatial, 46
- turbulence, 60
- frozen-in field, 15, 20
- γ -rays
 - near-simultaneity with HXRs, 8
- gamma-rays
 - broad lines, 9
 - correlation with hard X-rays, 10
 - deexcitation lines, 9
 - imaging, 11, 23
 - lightcurves, 8
 - narrow lines, 9
 - synchronism with hard X-rays, 8
- GOES* classification, 10
- hard X-rays
 - albedo, 6, 60
 - and radio emission, 12
 - coronal sources, 5, 40
 - correlation with footpoint sources, 10
 - pivot point, 60
 - soft-hard-soft, 25, 60
 - directivity, 6
 - footpoint sources, 10
 - gradual emission, 4
 - imaging, 23
 - lightcurves and spectra, 4
 - looptop sources, 3
 - near-simultaneity with γ -rays, 8
 - soft-hard-soft, 5, 60
 - spectra
 - footpoints, 10
 - footpoints vs. coronal sources, 10
 - pivot point, 25
 - spectrum
 - double power law, 5
 - thermal interpretation, 5
 - thin-target, 5
- inverse problem
 - forward fit, 8
- ion-neutral coupling, 27
- ions
 - distribution functions, 9
 - number problem, 9
 - total energy, 10
 - dependence on spectral distribution, 9
 - transport time scales, 8
- isothermal spectrum
 - improbability of, 5
- jets, 61
 - reconnection outflow, 24, 30, 40
 - illustration, 28, 56
- Langmuir waves, 53
- “local” spectral index, 5
- looptop sources, 3
- low-energy cutoff, 7, 9, 25
 - and albedo, 7
 - and warm target, 7
- magnetic diffusion equation, 14
- magnetic field
 - chromospheric, 27
 - flare-related changes, 13
 - in core of active region, 27
 - induced by particles, 24
 - inductive, 8
 - non-potential, 3
 - observation, 12
 - wave, 22
- magnetic moment
 - dimensionless, 38
- magnetic Reynolds number, 14
- magnetic structures
 - collapsing trap, 24, 28, 29
 - complex, 41
 - cusp, 24
 - fan, 17, 37
 - filamentation, 21
 - fractal dimension, 43
 - hard X-ray and γ -ray sources, 10
 - helmet, 18, 28
 - interacting loops, 18, 19
 - islands, 54, 56, 61
 - and tearing mode, 25
 - illustration, 57
 - neutral points, 16
 - loss cone, 30
 - definition, 31
 - mirror geometry, 3, 17
 - moving, 29, 30
 - multiple unstable current sheet, 42
 - neutral line, 13
 - illustration, 17

- null, 17, 24, 37
 - change in aspect ratio, 35
 - illustration, 15, 56
 - O-type (elliptic), 16
 - potential, 38
 - X-type (hyperbolic), 16
- PIC simulation
 - magnetic null, 57
 - model size limits, 57
- PIC simulation of magnetic islands
 - illustration, 55
- separator, 17
- separatrix, 17
- spine, 17, 37
- magnetic tension, 56
- magnetization
 - differential, 16, 20
- magnetosphere, 26
 - shocks, 21
- mass ratio
 - artificial value of, 59
- Parker, E. N., 15
- pitch-angle diffusion, 21
- pitch-angle scattering, 23
- plasma instabilities
 - bump-on-tail, 53
 - cold-beam, 48
 - electron-cyclotron maser, 12
 - in PIC simulations
 - list, 54
 - Kelvin-Helmholtz, 16, 54
 - kink, 16, 54
 - lower hybrid drift, 16, 54
 - parametric, 27
 - resistive, 16
 - sausage, 16, 54
 - tearing mode, 25, 54, 57, 61
 - two-stream, 48
 - various, 28
- plasma turbulence, 3, 46, 59, 61, 62
- polarization
 - electric field, 34, 47
- potential null, 38
- Poynting flux, 26, 27
- probability densities
 - in cellular automata, 43
- prominence
 - eruptive, 28
- radio emission
 - association with hard X-rays, 12
 - decimetric spikes, 12
 - coherent, 12
 - and flare energy release, 13
 - decimetric spikes, 12
 - gyrosynchrotron, 12
 - narrow-band spikes, 13
 - plasma radiation, 32
 - pulsations, 13
 - termination-shock signature, 30
 - type III burst
 - harmonic, 12
 - type IV burst
 - stationary, 13
- Rankine-Hugoniot relations, 32
- reconnection, 3, 14
 - 2-D theory, 15
 - 2-D vs. 3-D, 17
 - and particle acceleration, 14
 - and Poynting-flux transport, 28
 - current sheet
 - number problem, 21
 - fan, 17, 37
 - Hall, 16
 - ideal region, 38
 - multiple current sheets, 21
 - multiple sites, 13
 - Petschek, 15
 - slow, 15
 - spine, 17, 37
 - spine and fan
 - test-particle acceleration, 40
 - Sweet-Parker, 3, 15
 - PIC, 57
 - two-fluid, 16
- relativistic equations of motion, 33
- resistivity
 - anomalous, 16, 28, 54
 - hybrid, 45
- return current, 8, 23, 59
 - electric field, 58
- RHESSI*, 3
 - “pure” gamma-ray lines, 8
- ribbons, 41
 - and fans, 61
- satellites
 - GOES*, 10

- GRANAT*
- PHEBUS, 5
- RHESSI*, 3
- SMM*, 9
 - GRS, 9
- SOHO*, 11
- Yohkoh*, 3
- scattering
 - Compton, 6
 - in Fermi acceleration, 22
 - pitch-angle, 21, 23, 24
- self-organized critical state, 41, 61
- separatrix, 17, 37
- shocks
 - and reconnection, 3
 - particle acceleration, 21
 - termination, 4, 24, 29
 - numerical simulation, 30
- simulations
 - 3-D MHD
 - and cellular automata, 43
 - kinetic, 16
 - MHD, 22
 - as framework for test-particle acceleration, 45
 - reconnection shocks, 30
 - standard flare model, 28
 - PIC, 16, 20, 21, 24, 36
 - 3-D current sheet, 48
 - acceleration in magnetic islands, 54
 - collapsing islands, 54
 - effect of polarization electric field, 48
 - energy spectra, 52
 - limitations, 57
 - low-density assumption, 49
 - particle trajectories, 52
 - small mass-ratio assumption, 49
 - super-Alfvénic outflow jets, 57
 - turbulent electric field, 52
 - two-fluid, 27
- skin depth, 49
- soft X-rays
 - multi-thermal bremsstrahlung modeling, 5
- soft-hard-soft, 60
 - in coronal sources, 25
- SOHO*
- MDI, 11
- spectrum
 - hard X-ray, 5
- speed of light
 - artificial reduction in simulations, 59
- Sweet, P. A., 15
- termination shock, 29
 - and particle acceleration, 30
- test-particle approach
 - limitations, 32, 33, 36, 46
- thick-target model, 5
- time-of-flight analysis, 5
- transit particles, 33, 49
- transit-time damping, 23
- transport
 - biases acceleration theory, 59
 - ions, 8
- trapping
 - by turbulence, 3
- turbulence, 3
 - p*-model, 46
 - ad hoc, 25
 - MHD, 4, 22, 23, 25
 - perpendicular cascade, 27
 - plasma wave, 22
- warm target, 7
- waves
 - Alfvén
 - and magnetic reconnection, 28
 - illustration, 26
 - reflection at chromosphere, 27
 - Alfvén mode, 27
 - fast-mode
 - broad-band, 23
 - growth rate, 24
 - ion-acoustic, 27
 - Langmuir, 53
 - magneto-acoustic, 16
 - and particle acceleration, 22
 - whistlers, 16, 55